JETP Letters, Vol. 82, No. 9, 2005, pp. 551–556. From Pis'ma v Zhurnal Éksperimental'noĭ i Teoreticheskoĭ Fiziki, Vol. 82, No. 9, 2005, pp. 627–632.
Original English Text Copyright © 2005 by Isayev.

Two-Body Correlation Functions in Nuclear Matter with Neutron–Proton Condensate¶

A. A. Isayev
Kharkov Institute of Physics and Technology, Kharkov, 61108 Ukraine
Kharkov National University, Kharkov, 61077 Ukraine

Received September 13, 2005; in final form, September 29, 2005

The density, spin, and isospin correlation functions in nuclear matter with a neutron–proton condensate are calculated to study the possible signatures of the BEC–BCS crossover in the low-density region. It is shown that the criterion of the crossover (Phys. Rev. Lett. **95**, 090402 (2005)), consisting in the change of the sign of the density correlation function at low momentum transfer, fails to describe correctly the density-driven BEC–BCS transition at finite isospin asymmetry or finite temperature. The presence (BCS regime) or absence (BEC regime) of the singularity in the momentum distribution of the quasiparticle density of states can be used as an unambiguous signature of the BEC–BCS transition. *© 2005 Pleiades Publishing, Inc.*

PACS numbers: 21.30.Fe, 21.65.+f, 71.10.Ay

INTRODUCTION

Neutron–proton pairing correlations play an important role in a number of contexts, including the study of medium-mass $N \approx Z$ nuclei produced at the radioactive nuclear beam facilities [1] and the process of deuteron formation in medium-energy heavy-ion collisions [2]. In the astrophysical context, neutron–proton (*np*) pairing correlations are relevant for the astrophysical *r* process [3], which is responsible for the synthesis of nuclear species more massive than iron, and can play a major role in neutron star models, which permit pion or kaon condensation [4]. For not too low densities, *np* pairing correlations crucially depend on the overlap between neutron and proton Fermi surfaces, and even a small isospin asymmetry effectively destroys a condensate with *np* Cooper pairs due to the Pauli blocking effect [5–7]. However, under decreasing density, when neutrons and protons start to bind in deuterons and the spatial separation between deuterons, and between deuterons and extra neutrons, is large, the Pauli blocking loses its efficiency in destroying a *np* condensate. In such a situation, despite the fact that the isospin asymmetry may be very large, a *np* condensate survives and exists in the form of a Bose–Einstein condensate of deuterons.

The transition from BCS superconductivity to Bose–Einstein condensation (BEC) occurs in a Fermi system if either density is decreased or the attractive interaction between fermions is increased sufficiently. This transition was first studied in excitonic semiconductors [8] and then in an attractive Fermi gas [9]. Later, it was realized that an analogous phase transition takes place in symmetric nuclear matter, when *np* Cooper pairs at higher densities go over to BEC of deuterons at lower densities [2, 5]. During this transition, the chemical potential changes its sign at certain critical density (Mott transition), approaching half of the deuteron binding energy at ultralow densities. In [5], crossover from *np* superfluidity to a BEC of deuterons was investigated in the *T*-matrix approach, where the pole in the *T* matrix determines the critical temperature of BEC of bound states in the case of negative chemical potential and the critical temperature of the appearance of *np* Cooper pairs in the case of positive chemical potential. The influence of isospin asymmetry on the BEC–BCS crossover in nuclear matter was studied in [10] within the BCS formalism. It has been shown that a Bose–Einstein condensate is weakly affected by an additional gas of free neutrons even at very large asymmetries. The same conclusion was also confirmed in [11] on the basis of the variational approach for the thermodynamic potential.

The recent upsurge of interest to the BEC–BCS crossover was caused by the discovery of BCS pairing in ultracold trapped quantum atom gases [12, 13]. In this study, we examine the possible signatures of the BEC–BCS crossover in low-density nuclear matter. It may have interesting consequences, for example, in the far tails of the density profiles of exotic nuclei, where a deuteron condensate can exist in spite of the fact that the density there can be quite asymmetric. In addition, similar physical effects can play an important role in the expanding nuclear matter formed in heavy-ion collisions or in nuclear matter in the crust of a neutron star. The main emphasis is placed on the behavior of the density, spin, and isospin correlation functions across the BEC–BCS transition region. The study is motivated by the results of [14], where the authors state that the

---

¶ The text was submitted by the author in English.

density correlation function of a two-component ultracold fermionic gas of atoms changes sign at low momentum transfer, and this represents an unambiguous signature of the BEC–BCS crossover. This statement is checked for nuclear matter taking into account additional factors: finite isospin asymmetry or finite temperature. In both cases, this criterion fails to provide a correct description of the density-driven BEC–BCS crossover and cannot serve as the universal feature of transition between two states of the system.

BASIC EQUATIONS

Superfluid states of nuclear matter are described by the normal f and anomalous g distribution functions of nucleons

$$f_{\kappa_1\kappa_2} = \mathrm{Tr}\rho \overset{+}{a}_{\kappa_2} a_{\kappa_1}, \quad g_{\kappa_1\kappa_2} = \mathrm{Tr}\rho a_{\kappa_2} a_{\kappa_1}, \qquad (1)$$

where $\kappa \equiv (\mathbf{k}, \sigma, \tau)$, $\mathbf{k}$ is momentum, $\sigma(\tau)$ is the projection of spin (isospin) on the third axis, and ρ is the density matrix of the system. We shall study np pairing correlations in the pairing channel with total spin S and isospin T of a pair $S = 1$, $T = 0$ and the projections $S_z = T_z = 0$. In this case, the distribution functions for isospin-asymmetric nuclear matter have the structure

$$\begin{aligned} f(\mathbf{k}) &= f_{00}(\mathbf{k})\sigma_0\tau_0 + f_{03}(\mathbf{k})\sigma_0\tau_3, \\ g(\mathbf{k}) &= g_{30}(\mathbf{k})\sigma_3\sigma_2\tau_2, \end{aligned} \qquad (2)$$

where σ_i and τ_k are the Pauli matrices in spin and isospin spaces, respectively. Using the minimum principle of the thermodynamic potential and the procedure of block diagonalization [7], one can obtain expressions for the distribution functions:

$$f_{00}(\mathbf{k}) = \frac{1}{2} - \frac{\xi_k}{4E_k}\left(\tanh\frac{E_k^+}{2T} + \tanh\frac{E_k^-}{2T}\right), \qquad (3)$$

$$f_{03}(\mathbf{k}) = \frac{1}{4}\left(\tanh\frac{E_k^+}{2T} - \tanh\frac{E_k^-}{2T}\right), \qquad (4)$$

$$g_{30}(\mathbf{k}) = -\frac{\Delta(\mathbf{k})}{4E_k}\left(\tanh\frac{E_k^+}{2T} + \tanh\frac{E_k^-}{2T}\right). \qquad (5)$$

Here,

$$E_k^{\pm} = E_k \pm \delta\mu = \sqrt{\xi_k^2 + \Delta^2(\mathbf{k})} \pm \delta\mu, \quad \xi_k = \frac{\mathbf{k}^2}{2m} - \mu, \qquad (6)$$

Δ being the energy gap in the quasiparticle excitation spectrum, m being the effective nucleon mass, and μ and $\delta\mu$ being half of a sum and half of a difference of neutron and proton chemical potentials, respectively.

Equations governing np pairing correlations in the $S = 1$, $T = 0$ pairing channel can be obtained on the basis of the Green's function formalism and have the form [7, 11]

$$\Delta(\mathbf{k}) = -\frac{1}{V}\sum_{\mathbf{k}'} V(\mathbf{k}, \mathbf{k}')\frac{\Delta(\mathbf{k}')}{2E_{k'}}(1 - f(E_{k'}^+) - f(E_{k'}^-)), \qquad (7)$$

$$\rho = \frac{2}{V}\sum_{\mathbf{k}}\left(1 - \frac{\xi_k}{E_k}[1 - f(E_k^+) - f(E_k^-)]\right) \equiv \frac{2}{V}\sum_{\mathbf{k}} n_k, \qquad (8)$$

$$\alpha\rho = \frac{2}{V}\sum_{\mathbf{k}}(f(E_k^-) - f(E_k^+)), \qquad (9)$$

where $f(E)$ is the Fermi distribution function. Equation (7) is the equation for the energy gap Δ, and Eqs. (8) and (9) are equations for the total density $\rho = \rho_p + \rho_n$ and neutron excess $\delta\rho = \rho_n - \rho_p \equiv \alpha\rho$ (α being the asymmetry parameter). Note that, since we consider a unitary superfluid state ($\Delta\Delta^+ \propto I$), Eqs. (7)–(9) formally coincide with the equations for a two-component isospin-asymmetric superfluid with singlet spin pairing between unlike fermions. Introducing the anomalous density

$$\psi(\mathbf{k}) = \langle \overset{+}{a}_{n,k} \overset{+}{a}_{p,-k} \rangle = \frac{\Delta(\mathbf{k})}{2E_k}(1 - f(E_k^+) - f(E_k^-))$$

and using Eq. (8), one can represent Eq. (7) for the energy gap in the form

$$\frac{k^2}{m}\psi(\mathbf{k}) + (1 - n_k)\sum_{\mathbf{k}'} V(\mathbf{k}, \mathbf{k}')\psi(\mathbf{k}') = 2\mu\psi(\mathbf{k}). \qquad (10)$$

In the limit of vanishing density, $n_k \longrightarrow 0$, Eq. (10) goes over to the Schrödinger equation for the deuteron bound state [2, 10]. The corresponding energy eigenvalue is equal to 2μ. The change in the sign of the mean chemical potential μ of neutrons and protons under decreasing density of nuclear matter signals the transition from the regime of large overlapping np Cooper pairs to the regime of nonoverlapping bound states (deuterons).

Let us consider the two-body density correlation function

$$\begin{aligned} \mathcal{D}(\mathbf{x}, \mathbf{x}') &= \mathrm{Tr}\rho\Delta\hat{n}(\mathbf{x})\Delta\hat{n}(\mathbf{x}'), \quad \Delta\hat{n}(\mathbf{x}) = \hat{n}(\mathbf{x}) - \hat{n}, \\ \hat{n}(\mathbf{x}) \equiv \sum_{\sigma\tau}\overset{+}{\psi}_{\sigma\tau}(\mathbf{x})\psi_{\sigma\tau}(\mathbf{x}) &= \frac{1}{V}\sum_{\sigma\tau\mathbf{k}\mathbf{k}'} e^{i(\mathbf{k}'-\mathbf{k})\mathbf{x}}\overset{+}{a}_{\mathbf{k}\sigma\tau}a_{\mathbf{k}'\sigma\tau}, \\ \hat{n} &= \frac{1}{V}\sum_{\sigma\tau\mathbf{k}}\overset{+}{a}_{\mathbf{k}\sigma\tau}a_{\mathbf{k}\sigma\tau}. \end{aligned} \qquad (11)$$

Its general structure in the spatially uniform and isotropic case reads [15]

$$\mathcal{D}(\mathbf{x}, \mathbf{x}') = \rho\delta(\mathbf{r}) + \rho D(r), \quad \mathbf{r} = \mathbf{x} - \mathbf{x}'. \qquad (12)$$

The function $D(r)$ is called the density correlation function, as well. We will be interested in the behavior of the function $D(r)$. The trace in Eq. (10) can be calculated by using definitions (1) and the Wick rules. Taking into account Eqs. (2) and going to the Fourier representation

$$D(q) = \int d^3\mathbf{r}\, e^{i\mathbf{qr}} D(r),$$

one can get

$$D(q) = I_g^{30}(q) - I_f^{00}(q) - I_f^{03}(q), \tag{13}$$

where

$$I_f^{00}(q) = \frac{4}{\pi^3\rho}\int_0^\infty dr r^2 j_0(rq)\left[\int_0^\infty dk k^2 f_{00}(k) j_0(rk)\right]^2,$$

$$I_f^{03}(q) = \frac{4}{\pi^3\rho}\int_0^\infty dr r^2 j_0(rq)\left[\int_0^\infty dk k^2 f_{03}(k) j_0(rk)\right]^2,$$

$$I_g^{30}(q) = \frac{4}{\pi^3\rho}\int_0^\infty dr r^2 j_0(rq)\left[\int_0^\infty dk k^2 g_{30}(k) j_0(rk)\right]^2.$$

Here, j_0 is the spherical Bessel function of the first kind and zeroth order. The functions I_f^{00}, I_f^{03}, and I_g^{30} represent the normal and anomalous contributions to the density correlation function. Analogously, we can consider the two-body spin correlation function

$$\mathscr{S}_{\mu\nu}(\mathbf{x}, \mathbf{x}') = \mathrm{Tr}\rho\Delta\hat{s}_\mu(\mathbf{x})\Delta\hat{s}_\nu(\mathbf{x}'),$$

$$\Delta\hat{s}_\mu(\mathbf{x}) = \hat{s}_\mu(\mathbf{x}) - \hat{s}_\mu,$$

$$\hat{s}_\mu(\mathbf{x}) \equiv \frac{1}{2}\sum_{\sigma\sigma'\tau}\psi^{+}_{\sigma\tau}(\mathbf{x})(\sigma_\mu)_{\sigma\sigma'}\psi_{\sigma'\tau}(\mathbf{x}) \tag{14}$$

$$= \frac{1}{2V}\sum_{\sigma\sigma'\tau\mathbf{k}\mathbf{k}'} e^{i(\mathbf{k}'-\mathbf{k})\mathbf{x}} a^{+}_{\mathbf{k}\sigma\tau}(\sigma_\mu)_{\sigma\sigma'} a_{\mathbf{k}'\sigma'\tau},$$

$$\hat{s}_\mu = \frac{1}{2V}\sum_{\sigma\sigma'\tau\mathbf{k}} a^{+}_{\mathbf{k}\sigma\tau}(\sigma_\mu)_{\sigma\sigma'} a_{\mathbf{k}\sigma'\tau},$$

and the two-body isospin correlation function

$$\mathscr{T}_{\mu\nu}(\mathbf{x}, \mathbf{x}') = \mathrm{Tr}\rho\Delta\hat{t}_\mu(\mathbf{x})\Delta\hat{t}_\nu(\mathbf{x}'),$$

$$\Delta\hat{t}_\mu(\mathbf{x}) = \hat{t}_\mu(\mathbf{x}) - \hat{t}_\mu,$$

$$\hat{t}_\mu(\mathbf{x}) \equiv \frac{1}{2}\sum_{\sigma\tau\tau'}\psi^{+}_{\sigma\tau}(\mathbf{x})(\tau_\mu)_{\tau\tau'}\psi_{\sigma\tau'}(\mathbf{x})$$

$$= \frac{1}{2V}\sum_{\sigma\tau\tau'\mathbf{k}\mathbf{k}'} e^{i(\mathbf{k}'-\mathbf{k})\mathbf{x}} a^{+}_{\mathbf{k}\sigma\tau}(\tau_\mu)_{\tau\tau'} a_{\mathbf{k}'\sigma\tau'}, \tag{15}$$

$$\hat{t}_\mu = \frac{1}{2V}\sum_{\sigma\tau\tau'\mathbf{k}} a^{+}_{\mathbf{k}\sigma\tau}(\tau_\mu)_{\tau\tau'} a_{\mathbf{k}\sigma\tau'}.$$

Their general structure for isospin-asymmetric nuclear matter without spin polarization is

$$\mathscr{S}_{\mu\nu}(\mathbf{x}, \mathbf{x}') = \frac{\rho}{4}\delta_{\mu\nu}\delta(\mathbf{r}) + \rho S_{\mu\nu}(r), \tag{16}$$

$$\mathscr{T}_{\mu\nu}(\mathbf{x}, \mathbf{x}') = \frac{\rho}{4}\delta_{\mu\nu}\delta(\mathbf{r}) + \frac{\alpha\rho}{4}i\epsilon_{\mu\nu 3}\delta(\mathbf{r}) + \rho T_{\mu\nu}(r). \tag{17}$$

Then, calculating traces in Eqs. (14) and (15), for the Fourier transforms of the spin and isospin correlation functions, one can get

$$\begin{aligned} S_{\mu\nu}(q) = -\frac{1}{4}\{&\delta_{\mu\nu}(I_f^{00}(q) + I_f^{03}(q)) \\ &+ (\delta_{\mu\nu} - 2\delta_{3\mu}\delta_{3\nu})I_g^{30}(q)\}, \end{aligned} \tag{18}$$

$$\begin{aligned} T_{\mu\nu}(q) = -\frac{1}{4}\{&\delta_{\mu\nu}(I_f^{00}(q) + I_g^{30}(q)) \\ &- (\delta_{\mu\nu} - 2\delta_{3\mu}\delta_{3\nu})I_f^{03}(q)\}. \end{aligned} \tag{19}$$

Note that, if we put $\nu = \mu = 3$ in Eqs. (18) and (19), we get the longitudinal spin S^l and isospin T^l correlation functions, while setting $\mu, \nu = 1, 2$ gives the transverse spin and isospin correlation functions

$$\begin{aligned} S^t_{\mu\nu}(q) &= -\frac{\delta_{\mu\nu}}{4}(I_f^{00}(q) + I_f^{03}(q) + I_g^{30}(q)) \equiv \delta_{\mu\nu}S^t(q), \\ &\mu, \nu = 1, 2, \\ T^t_{\mu\nu}(q) &= -\frac{\delta_{\mu\nu}}{4}(I_f^{00}(q) - I_f^{03}(q) + I_g^{30}(q)) \equiv \delta_{\mu\nu}T^t(q). \end{aligned} \tag{20}$$

The following relationships between the correlation functions are true:

$$S^l(q) = \frac{D(q)}{4}, \quad S^t(q) = T^l(q). \tag{21}$$

At zero temperature and zero momentum transfer, the correlation functions satisfy the sum rule

$$\begin{aligned} &S^t(q = 0) = T^l(q = 0) \\ &= -\frac{1}{2\pi^2\rho}\int dk k^2(f_{00}^2(k) + f_{03}^2(k) + g_{30}^2(k)) = -\frac{1}{4}, \end{aligned} \tag{22}$$

where the right-hand side is independent of density and isospin asymmetry. In addition, the transverse isospin correlation function satisfies the relationship

$$\begin{aligned} T^t(q = 0) &= -\frac{1}{2\pi^2\rho}\int dk k^2(f_{00}^2(k) - f_{03}^2(k) + g_{30}^2(k)) \\ &= -\frac{1-\alpha}{4}, \end{aligned} \tag{23}$$

where the right-hand side is independent of density.

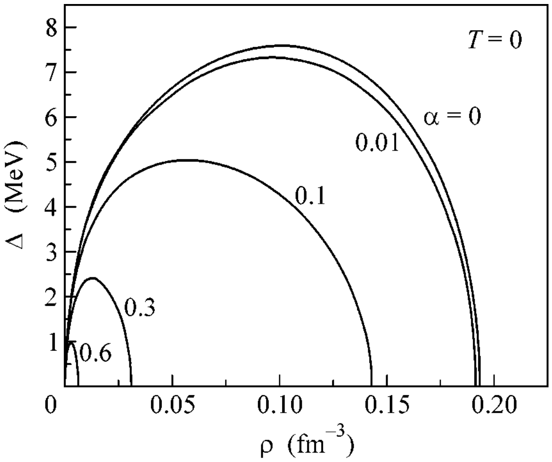

Fig. 1. Energy gap as a function of density at zero temperature and different asymmetries.

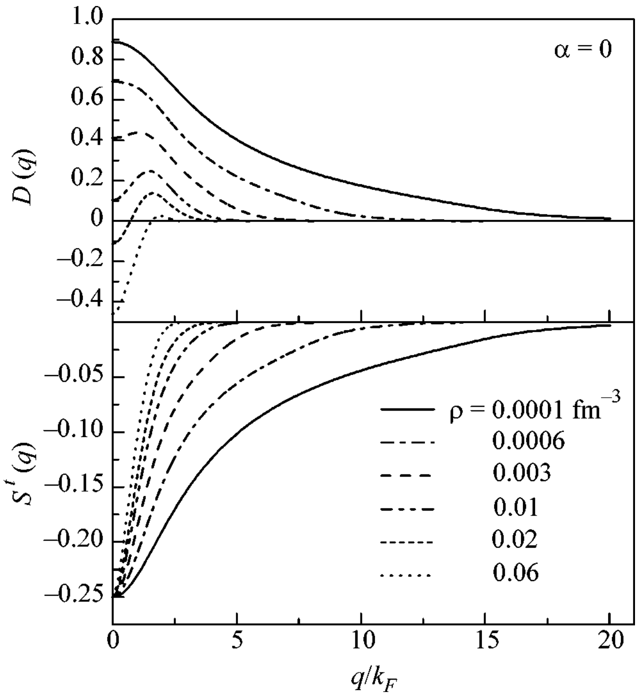

Fig. 2. Density and transverse spin correlation functions as functions of momentum at zero temperature and different densities for symmetric nuclear matter.

CORRELATION FUNCTIONS IN NUCLEAR MATTER WITH A *np* CONDENSATE

Further, for numerical calculations, we shall use the effective zero range force, which was developed in [16] to reproduce the pairing gap in $S = 1$, $T = 0$ pairing channel with a Paris *NN* potential:

$$V(\mathbf{r}_1, \mathbf{r}_2) = v_0\left\{1-\eta\left(\frac{\rho\left(\frac{\mathbf{r}_1+\mathbf{r}_2}{2}\right)}{\rho_0}\right)^{\gamma}\right\}\delta(\mathbf{r}_1-\mathbf{r}_2), \quad (24)$$

where $\rho_0 = 0.16$ fm^{-3} is the nuclear saturation density, $v_0 = -530$ MeV fm^3, $\eta = 0$, $m = m_G$, m_G being the effective mass corresponding to the Gogny force D1S. Also, in the gap equation (7), Eq. (24) must be supplemented with a cutoff parameter, $\varepsilon_c = 60$ MeV.

To find the correlation functions, one should first solve the gap equation (7) self-consistently with Eqs. (8) and (9). The correlation functions can then be determined directly from Eqs. (13), (18), and (19). The results of numerical determination of the energy gap as a function of density for different asymmetries at zero temperature are shown in Fig. 1. As one can see, with increasing asymmetry, the magnitude of the energy gap is decreased and the density interval where a *np* condensate exists shrinks to lower density. In reality, solutions exist for any $\alpha < 1$ (the phase curves for larger values of α are not shown in Fig. 1) and correspond to the formation of a BEC of deuterons at very low densities of nuclear matter.

Now we consider the correlation functions $D(q)$ and $S^t(q)$ for symmetric nuclear matter at zero temperature, depicted in Fig. 2 (at $\alpha = 0$, $T^t(q) = S^t(q)$). The density correlation function changes sign at low momentum transfer when the system smoothly evolves from the BEC regime to the BCS regime. These two regimes are distinguished by negative and positive values of the chemical potential μ, respectively. In view of Eq. (21), the longitudinal spin correlation function $S^l(q)$ changes sign through the BEC–BCS crossover as well. The transverse spin correlation function and, according to Eq. (21), the longitudinal and transverse isospin correlation functions change fluently between BEC and BCS limits. The behavior of the density correlation function in the isospin-symmetric case at zero temperature qualitatively agrees with the behavior of the density correlation function in an ultracold fermionic atom gas with singlet pairing of fermions [14]. In [14], the change in the sign of the density correlation function at low momentum transfer was considered as a signature of the BEC–BCS crossover. We would like to extend their calculations taking into account the finite isospin asymmetry and finite temperature.

Figure 3 shows the dependence of the density correlation function $D(\mathbf{q} = 0)$ at zero momentum transfer as a function of density for a set of various isospin asymmetry parameters and zero temperature. It is seen that, with increasing asymmetry parameter, the density correlation function decreases. For strong enough asymmetry, the function $D(\mathbf{q} = 0)$ is always negative. In accordance with the above criterion, the density region where the function $D(\mathbf{q} = 0)$ has positive or negative values would correspond to the BEC or BCS regime, respectively. Hence, as follows from Fig. 3, for strong isospin asymmetry, we would have only the BCS state for all densities, where a *np* condensate exists. Obviously, this conclusion contradicts the behavior of the mean chemical potential μ, being negative at very low densities for any $\alpha < 1$, and, hence, giving evidence to

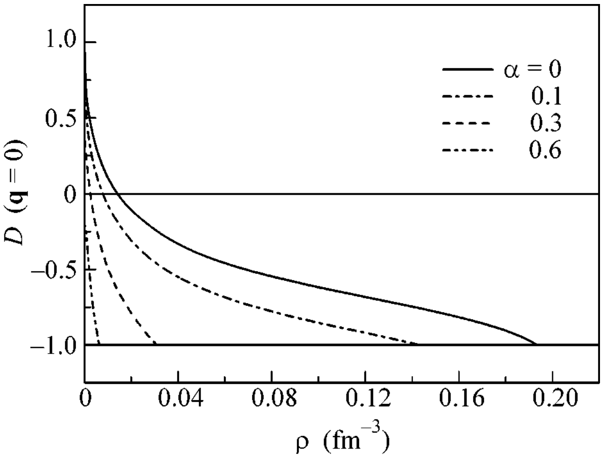

Fig. 3. Density correlation function $D(\mathbf{q} = 0)$ as a function of density at zero temperature for different isospin asymmetry parameters.

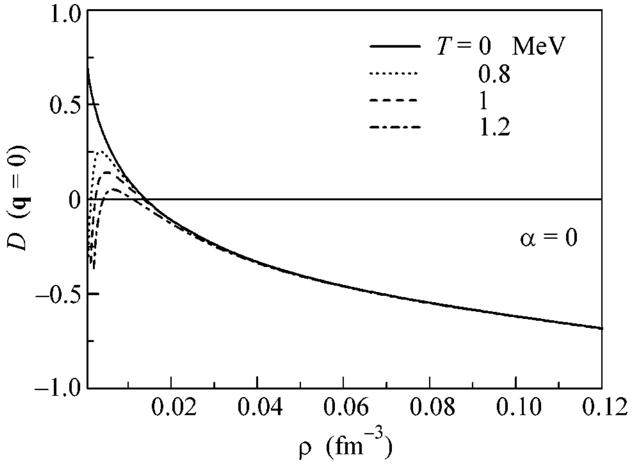

Fig. 4. Density correlation function $D(\mathbf{q} = 0)$ as a function of density at different temperatures for symmetric nuclear matter.

the formation of BEC of bound states [11]. Thus, at strong enough isospin asymmetry, the criterion of the crossover based on the change of the sign of the density correlation function fails to predict the transition to the BEC of deuterons in low-density nuclear matter.

Now we consider symmetric nuclear matter at finite temperature. Figure 4 shows the dependence of the density correlation function $D(\mathbf{q} = 0)$ at zero momentum transfer as a function of density for a set of various temperatures. It is seen that, for not too high temperatures, the density response function is nonmonotonic and twice changes sign in the region of low densities. Hence, in accordance with the above criterion, we would have the density interval $\rho_1 < \rho < \rho_2$ with the BEC state, surrounded by the density regions with the BCS state. However, this conclusion contradicts the behavior of the mean chemical potential μ for these temperatures, being a monotonic function of density and indicating the formation of a BEC state at low densities ($\mu < 0$) and a BCS state at larger densities ($\mu > 0$). Thus, at finite temperature, the criterion of the crossover formulated in [14] fails to provide the correct description of the transition between two regimes.

In summary, we have calculated the density, spin, and isospin correlation functions in superfluid nuclear matter with *np* pairing correlations, intending to find the possible signatures of the BEC–BCS crossover. It is shown that the transverse spin and longitudinal and transverse isospin correlation functions satisfy the sum rule at zero momentum transfer and zero temperature and change smoothly between BEC and BCS regimes. In [14], it was learned that the density correlation function in a two-component ultracold fermionic atom gas with singlet pairing of fermions changes sign at low momentum transfer across the BEC–BCS transition, driven by a change in the scattering length of the interaction at zero temperature. We have shown that, for spin triplet pairing, the longitudinal spin correlation function plays an analogous role to the density correlation function and changes sign at low momentum transfer across the crossover in symmetric nuclear matter at zero temperature. However, while giving a satisfactory description of the density-driven BEC–BCS crossover in dilute nuclear matter at zero temperature for the isospin-symmetric case, this criterion fails to provide the correct description of the crossover at finite isospin asymmetry (nonequal densities of fermions of different species) or finite temperature. Hence, the criterion in [14] cannot be considered as the universal indication of the BEC–BCS transition. During the Mott transition, when the chemical potential changes sign, there is a qualitative change in the quasiparticle energy spectrum: the minimum shifts from a finite (BCS state) to zero-momentum value (BEC state) (see Eq. (6) and [17]). As such, the presence (BCS) or absence (BEC) of the singularity in the momentum distribution of the quasiparticle density of states represents the universal signature of the BEC–BCS transition. This transition may be relevant and could give valuable information on *np* pairing correlations in low-density nuclear systems, such as tails of nuclear density distributions in exotic nuclei produced at radioactive nuclear beam facilities, expanding nuclear matter in heavy-ion collisions, and low-density nuclear matter in outer regions of neutron stars.

REFERENCES

1. A. L. Goodman, Phys. Rev. C **60**, 014311 (1999).
2. M. Baldo, U. Lombardo, and P. Schuck, Phys. Rev. C **52**, 45 (1995).
3. B. K.-L. Kratz, J.-P. Bitouzet, F.-K. Thielmann, *et al.*, Astrophys. J. **403**, 216 (1993).
4. G. E. Brown and H. A. Bethe, Astrophys. J. **423**, 659 (1994).

5. T. Alm, B. L. Friman, G. Röpke, *et al.*, Nucl. Phys. A **551**, 45 (1993).
6. A. Sedrakian and U. Lombardo, Phys. Rev. Lett. **84**, 602 (2000).
7. A. I. Akhiezer, A. A. Isayev, S. V. Peletminsky, *et al.*, Phys. Rev. C **63**, 021304 (2001).
8. L. V. Keldysh and Yu. V. Kopaev, Sov. Phys. Solid State **6**, 2219 (1965).
9. P. Nozieres and S. Schmitt-Rink, J. Low Temp. Phys. **59**, 195 (1985).
10. U. Lombardo, P. Nozieres, P. Schuck, *et al.*, Phys. Rev. C **64**, 064314 (2001).
11. A. A. Isayev, S. I. Bastrukov, and J. Yang, Nucl. Phys. A **734**, E112 (2004); Phys. At. Nucl. **67**, 1840 (2004).
12. M. W. Zwierlein, C. A. Stan, C. H. Schunck, *et al.*, Phys. Rev. Lett. **92**, 120403 (2004).
13. J. Kinast, S. L. Hemmer, M. E. Gehm, *et al.*, Phys. Rev. Lett. **92**, 150402 (2004).
14. B. Mihaila, S. Gaudio, K. B. Blagoev, *et al.*, Phys. Rev. Lett. **95**, 090402 (2005).
15. L. D. Landau and E. M. Lifshitz, *Course of Theoretical Physics*, Vol. 5: *Statistical Physics*, 3rd ed. (Nauka, Moscow, 1976; Pergamon, Oxford, 1980), Part 1.
16. E. Garrido, P. Sarriguren, E. Moya de Guerra, *et al.*, Phys. Rev. C **63**, 037304 (2001).
17. M. Parish, B. Mihaila, E. M. Timmermans, *et al.*, Phys. Rev. B **71**, 064513 (2005).

JETP Letters, Vol. 82, No. 9, 2005, pp. 557–561. From Pis'ma v Zhurnal Éksperimental'noĭ i Teoreticheskoĭ Fiziki, Vol. 82, No. 9, 2005, pp. 633–637.

QCD String and the Lorentz Nature of Confinement¶

A. V. Nefediev and Yu. A. Simonov
Institute of Theoretical and Experimental Physics, Moscow, 117218 Russia
Received September 19, 2005

We address the question of the Lorentz nature of the effective long-range interquark interaction generated by the QCD string with quarks at the ends. Studying the Dyson–Schwinger equation for a heavy–light quark–antiquark system, we demonstrate explicitly how a Lorentz scalar interaction appears in the Dirac-like equation for the light quark as a consequence of chiral symmetry breaking. We argue that the effective interquark interaction in the Hamiltonian of the QCD string with quarks at the ends stems from this effective scalar interaction. *© 2005 Pleiades Publishing, Inc.*

PACS numbers: 12.38.Aw, 12.39.–x

1. INTRODUCTION

Description of the spectrum of mass and other properties of hadrons is one of the main tasks of QCD as the theory of strong interactions, and a variety of nonperturbative theoretical approaches have been developed for this purpose. In this paper, we touch upon two of them, which we believe to be complementary to one another. On one hand, the quantum mechanical approach of the QCD string with quarks at the ends can be derived starting from the fundamental QCD Lagrangian. On the other hand, a field-theory-inspired approach based on the Dyson–Schwinger equation for quarkonia can be developed. The two mentioned approaches allow one to make reliable predictions for the properties of hadrons, although both of them meet certain problems and should be applied together, side by side. For example, the approach based on the Dyson–Schwinger equation for quarkonia is well adjusted for the case of heavy–light systems, whereas, in the light–light case, its application is not straightforward. Meanwhile, the QCD string approach can be readily applied to both heavy–light and light–light quarkonia, as well as to other hadrons, including those with excited gluonic degrees of freedom. Unfortunately, since the effects of spontaneous breaking of chiral symmetry (SBCS) are not inherent to the string model, there is no hope of reproducing the properties of the lightest states in the mesonic spectrum—the pions and the kaons—in this approach. This is the problem for which the method of the Dyson–Schwinger equation comes to the rescue. Indeed, this method appears appropriate for studies of chiral symmetry breaking (CSB) and for all phenomena related to it. In this paper, we make one more step on the way to merging the two aforementioned methods and study the problem of the Lorentz nature of confinement generated by the QCD string. Considering a heavy–light quarkonium, we employ the Dyson–Schwinger approach to derive an effective Dirac-like bound state equation for the spectrum of the system. We argue that it is SBCS, caused by confinement, which gives rise to the scalar part of the interquark interaction in this equation and demonstrate how the confinement-induced scalar interaction reduces, under certain conditions, to a local potential dynamics described by the quantum mechanical Salpeter equation for quarkonium. Finally, we extend this conclusion of the scalar nature of the effective interquark interaction to the case of a rotating QCD string with quarks at the ends.

2. QCD STRING AND THE SPINLESS SALPETER EQUATION

In this section, we remind the reader of the main steps used to derive the Hamiltonian of the QCD string with quarks at the ends in the vacuum correlator method (VCM) [1]. We start from the gauge-invariant in- and out-states of the quarkonium, $\Psi^{(\text{in, out})}_{q\bar{q}}(x, y\,|\,A) = \bar{\Psi}_{\bar{q}}(x)P\exp(ig\int_y^x dz_\mu A_\mu)\Psi_q(y)$ [2]. Now, writing the Green's function of the (flavor-nonsinglet) quark–antiquark meson,

$$G_{q\bar{q}} = \langle \Psi^{(\text{out})}_{q\bar{q}}(\bar{x}, \bar{y}|A)\Psi^{(\text{in})\dagger}_{q\bar{q}}(x, y|A)\rangle_{q\bar{q}A}, \tag{1}$$

and performing averaging over the gluonic field by means of the minimal area law for the isolated Wilson loop, we can extract the standard Nambu–Goto effective action for the string connecting the quarks,

$$S_{\min} = \int_0^T dt\int_0^1 d\beta\sqrt{(\dot{w}w')^2 - \dot{w}^2w'^2}, \tag{2}$$
$$w_\mu(t, \beta) = \beta x_{1\mu}(t) + (1-\beta)x_{2\mu}(t),$$

¶ The text was submitted by the authors in English.

where we used the straight-line string ansatz for the minimal surface [2]. Finally, considering the quark–antiquark system at rest in the laboratory reference frame, we synchronize the quark times and put them equal to the laboratory time, $x_{10} = x_{20} = t$. The resulting center-of-mass Hamiltonian reads [2]

$$H = \sum_{i=1}^{2}\left[\frac{p_r^2+m_i^2}{2\mu_i}+\frac{\mu_i}{2}\right]+\int_0^1 d\beta\left[\frac{\sigma^2 r^2}{2\nu}+\frac{\nu}{2}\right]$$
$$+\frac{\mathbf{L}^2}{2r^2\left[\mu_1(1-\zeta)^2+\mu_2\zeta^2+\int_0^1 d\beta\nu(\beta-\zeta)^2\right]}, \quad (3)$$

$$\zeta = \frac{\mu_1+\int_0^1 d\beta\nu\beta}{\mu_1+\mu_2+\int_0^1 d\beta\nu},$$

where, in order to get rid of the square roots in the relativistic quark kinetic terms and in the string term (2), we used the auxiliary field method and introduced the einbeins $\mu_{1,2}$ and $\nu(\beta)$. The interested reader can find the details of the einbein field formalism in the original paper [3] and examples of its application to the QCD string with quarks at the ends in [2, 4]. Notice that extremum conditions for all three einbeins are understood in order to arrive at the Hamiltonian in the final form, expressed via physical degrees of freedom only. The spinless Hamiltonian (3) is to be supplied by the nonperturbative spin–orbit interaction [5], as well as by the Coulomb potential and spin-dependent terms generated by the latter. The resulting model appears rather successful in studies of quarkonia: for example, the spectrum of heavy–light D, D_s, B, and B_s mesons can be reproduced with good accuracy this way [6]. The last, angular-momentum-dependent term in the Hamiltonian (3) contains a strong contribution of the proper dynamics of the string, described by the integral term in the denominator. The effect of this dynamics on the properties of the system is comprehensively studied in the literature and is known to bring the Regge trajectories slope to the experimental value [2, 7], to lower the masses of orbitally excited states [6], and so on. In the meantime, this contribution does not affect the Lorentz nature of the interquark interaction generated by the string. Therefore, for the sake of simplicity, we restrict ourselves to the case of $L = 0$ in the Hamiltonian (3), and we then take extrema in all einbeins explicitly. The resulting Hamiltonian,

$$H = \sqrt{p_r^2+m_1^2}+\sqrt{p_r^2+m_2^2}+\sigma r, \quad (4)$$

gives rise to the well-known Salpeter equation for the spectrum. For the heavy–light system with $m_1 \equiv M \longrightarrow \infty$ and $m_2 \equiv m$, it reads

$$\left[\sqrt{p_r^2+m^2}+\sigma r\right]\psi(r) = E\psi(r), \quad (5)$$

where E describes the excess of the bound state energy over the heavy-quark mass. Equation (5) is usually referred to as the Salpeter equation with the Lorentz vector interaction [8], as opposed to the would-be Lorentz scalar confinement, as in the equation

$$\left[\sqrt{p_r^2+(m+\sigma r)^2}\right]\psi(r) = E\psi(r). \quad (6)$$

Therefore, according to general expectations, the Klein paradox might have operated for such a system, and one might have expected problems with the collapse of the mesonic wave functions and uncontrolled production of light-quark pairs by such an interaction if confinement had been present in the effective Dirac equation for the light quark in the form of a Lorentz time vector. The aim of the present paper is to argue that this conclusion is misleading in the sense that the form (5) of the Salpeter equation *does not imply* that the confining potential σr appears as a Lorentz vector interaction in the one-particle Dirac equation for the light quark. On the contrary, we demonstrate that an effective scalar interquark interaction appears in this equation as a result of CSB; nevertheless, the resulting Salpeter equation has the form of Eq. (5) rather than of Eq. (6). As far as Eq. (6) is concerned, it was demonstrated in [8] that its spectrum contradicts the phenomenology of heavy–light mesons. Note also that we are not aware of any consistent way to derive such an equation in QCD.

3. HEAVY–LIGHT QUARKONIUM IN THE DYSON–SCHWINGER APPROACH

We start in this section with the necessary details of the Dyson–Schwinger approach to heavy–light quarkonium suggested in [9]. Since the trajectory of the infinitely heavy particle is a straight line, it is convenient to fix the so-called modified Fock–Schwinger gauge [10] for the background gluonic field (we work in Euclidean space),

$$\mathbf{x}\mathbf{A}(x_4,\mathbf{x}) = 0, \quad A_4(x_4,\mathbf{0}) = 0, \quad (7)$$

and thus to reduce the role of the static antiquark to providing the overall gauge invariance of the $q\bar{q}$ Green's function, which, in the gauge (7), coincides with the Green's function of the light quark. Then, the Dyson–Schwinger equation can be derived for the latter [9],

$$\begin{gathered}(-i\hat{\partial}_x - im)S(x,y)\\ +\int d^4z\gamma_4 S(x,z)\gamma_4\mathcal{K}(x,z)S(z,y) = \delta^{(4)}(x-y),\end{gathered} \quad (8)$$

where only the structure $\gamma_4 \times \gamma_4$ is kept for the sake of simplicity, whereas the interaction with the full structure $\gamma_\mu \times \gamma_\nu$ can be studied, as well (see [9, 11]). The quark kernel $\mathcal{K}(x, y)$ is related to the profile function $D(\tau, \lambda)$,

$$\begin{aligned}\mathcal{K}(x, y) &= \mathcal{K}(x_4 - y_4, \mathbf{x}, \mathbf{y}) \\ &= (\mathbf{x}\mathbf{y})\int_0^1 d\alpha\int_0^1 d\beta D(x_4 - y_4, |\alpha\mathbf{x} - \beta\mathbf{y}|),\end{aligned} \tag{9}$$

which, in turn, parametrizes the bilocal correlator of the gluonic-field tensors, $\langle F(x)F(y)\rangle \propto D(x - y)$ [1]. The profile D decreases in all directions of the Euclidean spacetime with the correlation length T_g, for which lattice simulations give as small a value as $T_g \simeq 0.2$–0.3 fm [12]; therefore, the limit $T_g \longrightarrow 0$, known as the string limit of QCD, is adequate. In this limit, the profile function $D(\tau, \lambda)$ can be approximated by the delta-functional form, $D(\tau, \lambda) = 2\sigma\delta(\tau)\delta(\lambda)$, which is consistent with the definition of the string tension [1],

$$\sigma = 2\int_0^\infty d\tau\int_0^\infty d\lambda D(\tau, \lambda). \tag{10}$$

Then, with the help of Eq. (9), the kernel is found in the following form:

$$\begin{aligned}&K(\mathbf{x}, \mathbf{y}) \\ &\equiv \frac{1}{2}\int_{-\infty}^{\infty}\mathcal{K}(x_4 - y_4, \mathbf{x}, \mathbf{y})e^{i\omega(x_4 - y_4)}d(x_4 - y_4) \\ &= \frac{1}{2}(\mathbf{x}\mathbf{y})\int_0^1 d\alpha\int_0^1 d\beta\int_{-\infty}^{\infty} d\tau D(\tau, |\alpha\mathbf{x} - \beta\mathbf{y}|) \\ &\approx \frac{1}{2}\sigma(|\mathbf{x}| + |\mathbf{y}| - |\mathbf{x} - \mathbf{y}|),\end{aligned} \tag{11}$$

where, in the last, approximate equality, the requirement of strict collinearity of the vectors $\mathbf{x}$ and $\mathbf{y}$ is relaxed, which is admissible at large distances, $|\mathbf{x}|, |\mathbf{y}| \gg |\mathbf{x} - \mathbf{y}|$.

The ultimate form of Eq. (11) allows one to establish a link to potential quark models for QCD [13], as well as to generalize the shape of the confining interquark interaction from linear confinement σr to a generic form $V(r)$. Now, we can rewrite the Dyson–Schwinger Eq. (8) in Minkowski space in the form

$$\begin{aligned}&(\alpha\mathbf{p} + \beta m)\Psi(\mathbf{x}) \\ &+ \int d^3z\Lambda(\mathbf{x}, \mathbf{z})K(\mathbf{x}, \mathbf{z})\Psi(\mathbf{z}) = E\Psi(\mathbf{x}),\end{aligned} \tag{12}$$

where the quantity $\Lambda(\mathbf{x}, \mathbf{z})$, introduced in [9], is defined as

$$\begin{aligned}\Lambda(\mathbf{x}, \mathbf{z}) &\equiv 2i\int\frac{d\omega}{2\pi}S(\omega, \mathbf{x}, \mathbf{z})\beta \\ &= \sum_{n=-\infty}^{\infty}\Psi_n(\mathbf{x})\operatorname{sgn}(n)\Psi_n^\dagger(\mathbf{z}).\end{aligned} \tag{13}$$

It is clear that the Lorentz nature of confinement in Eq. (12) depends entirely on the matrix structure of $\Lambda(\mathbf{x}, \mathbf{z})$. To proceed, we stick to the formalism of the chiral angle φ_p, the standard approach used in potential quark models [13]. In this formalism, the positive- and negative-energy solutions to the bound-state Eq. (12) can be parametrized in the form [14]

$$\begin{aligned}&\Psi_{n>0}(\mathbf{p}) = T_p\begin{pmatrix}\psi(\mathbf{p}) \\ 0\end{pmatrix}, \quad \Psi_{n<0}(\mathbf{p}) = T_p\begin{pmatrix}0 \\ \psi(\mathbf{p})\end{pmatrix}, \\ &T_p = \exp\left[-\frac{1}{2}(\gamma\hat{\mathbf{p}})\left(\frac{\pi}{2} - \varphi_p\right)\right].\end{aligned} \tag{14}$$

The wavefunction $\psi(\mathbf{p})$ obeys a Schrödinger-like eigenvalue equation which follows from Eq. (12) after the exact Foldy–Wouthuysen transformation generated by the Foldy operator $T_p^\dagger$ (see Eq. (18) below). The chiral angle φ_p is the solution to the mass-gap equation,

$$\begin{aligned}&p\sin\varphi_p - m\cos\varphi_p \\ &= \frac{\sigma}{p^2}\int_0^\infty\frac{dk}{2\pi}\left[\frac{4p^2k^2}{(p^2 - k^2)^2}\sin[\varphi_k - \varphi_p]\right. \\ &\left.\times\left(\frac{2pk}{(p + k)^2} + \ln\left|\frac{p - k}{p + k}\right|\right)\cos\varphi_k\sin\varphi_p\right],\end{aligned} \tag{15}$$

quoted here without derivation for the linearly rising potential. The interested reader can find the details of this formalism in [13]. Notice that the chiral angle also plays the role of the Foldy angle; this is a general feature of such models. For the purpose of the present research, it is sufficient to bear in mind that the chiral angle is a continuous smooth function which starts from $\pi/2$ at the origin, with the slope inversely proportional to the scale of the CSB generated by this solution. In the large-momentum limit, φ_p approaches zero. It is an easy task now to compute the function Λ [14],

$$\begin{aligned}\Lambda(\mathbf{p}, \mathbf{q}) &= (2\pi)^3\delta^{(3)}(\mathbf{p} - \mathbf{q})U_p, \\ U_p &= T_p^2\beta = \beta\sin\varphi_p + (\alpha\hat{\mathbf{p}})\cos\varphi_p,\end{aligned} \tag{16}$$

and to rewrite Eq. (12) in the form

$$\begin{aligned}&E_pU_p\Psi(\mathbf{p}) + \frac{1}{2}\int\frac{d^3k}{(2\pi)^3}V(\mathbf{p} - \mathbf{k}) \\ &\times(U_p + U_k)\Psi(\mathbf{k}) = E\Psi(\mathbf{p}),\end{aligned} \tag{17}$$

where E_p stands for the quark dispersive law and, for the linearly rising potential, $V(\mathbf{p}) = -8\pi\sigma/p^4$. Alternatively, this equation can be arrived at as the one-particle limit of the Bethe–Salpeter equation for the quark–antiquark meson in the framework of the potential quark models [13]. The Foldy–Wouthuysen transformation of Eq. (17), performed with the help of the Foldy operator $T_p^\dagger$, leads one to the Schrödinger-like equation [14],

$$E_p\psi(\mathbf{p}) + \int\frac{d^3k}{(2\pi)^3}V(\mathbf{p}-\mathbf{k}) \times[C_pC_k + (\sigma\hat{\mathbf{p}})(\sigma\hat{\mathbf{k}})S_pS_k]\psi(\mathbf{k}) = E\psi(\mathbf{p}), \tag{18}$$

where

$$C_p = \cos\frac{1}{2}\left(\frac{\pi}{2}-\varphi_p\right) \text{ and } S_p = \sin\frac{1}{2}\left(\frac{\pi}{2}-\varphi_p\right);$$

σ are Pauli matrices, and $\hat{\mathbf{p}}$ and $\hat{\mathbf{k}}$ are the unity vectors for $\mathbf{p}$ and $\mathbf{k}$, respectively.

With Eq. (17) in hand, we are in a position to comment on the Lorentz nature of confinement. CSB means an existence of the quark Green's function having the effective mass operator with the matrix γ_0 to an even power or, in the language of the chiral angle, the existence of a nontrivial solution to the mass-gap equation (15). This is trivially achieved for heavy quarks when the chiral symmetry is broken explicitly, since the quark mass term provides the required behavior of the quark Green's function and, in the meantime, saturates the chiral angle. For light (massless) quarks, such solutions for the quark Green's function and for the chiral angle are to appear self-consistently in order to provide SBCS. In either case, the chiral angle is different from zero for $0 \le p \lesssim \Lambda_\chi$, with the CSB scale Λ_χ given by the quark mass for heavy quarks, and by the nonperturbative scale $\sqrt{\sigma}$ for light quarks. The full structure of the matrix Λ and its influence on highly excited states in the spectrum is studied in detail in [14]. For the purpose of the present qualitative research, it is sufficient to stick either to very heavy quarks or to extremely strong confinement (the so-called pointlike limit of $\sqrt{\sigma} \longrightarrow \infty$, which can also be called the heavy-string limit). In this case, the chiral angle is $\varphi_p = \pi/2$ for all p, so that $U_p \approx \beta$ and, therefore,

$$\Lambda(\mathbf{x},\mathbf{z}) \approx \beta\delta^{(3)}(\mathbf{x}-\mathbf{z}). \tag{19}$$

Thus, using Eqs. (11), (12), and (19) altogether, we arrive at the effective Dirac equation for the light quark with a purely scalar confinement,

$$[\alpha\mathbf{p} + \beta(m + V(r))]\Psi(\mathbf{x}) = E\Psi(\mathbf{x}). \tag{20}$$

This coincides with the findings of [9], where a summation of quasiclassical eigenvalues of Eq. (20) with $V(r) = \sigma r$ was performed explicitly, and relation (19) was derived for light quarks. Notice that, for massless quarks, and had SBCS not happened, the chiral angle would have been identically zero, and the term proportional to the matrix β in U_p, as follows from Eq. (16), would have vanished. We see therefore that the effective scalar interquark interaction arises due to CSB, both explicit and spontaneous. In the same limit of $\varphi_p = \pi/2$, one has $C_p = 1$ and $S_p = 0$, so that the interaction part of Eq. (18) reduces to the potential $V(r)$ in coordinate space. As for the kinetic term in Eq. (18), for heavy quarks, it can be well approximated by the free-quark energy, $\sqrt{\mathbf{p}^2 + m^2}$. For light quarks, such a substitution is more arguable, though it is known to work rather well for heavy–light as well as for excited light–light mesons, when the nontrivial low-momentum behavior of the dressed-quark dispersive law E_p does not play a considerable role. (Notice that this approximation fails completely for the lowest light–light quark–antiquark state—for the chiral pion. The latter cannot be described by the Salpeter Hamiltonian, and one must consider the full Dyson–Schwinger equation; see [13, 15] for two complementary approaches to the problem of the pion.) Thus, starting from Eq. (18), we arrive at the Salpeter equation,

$$[\sqrt{\mathbf{p}^2 + m^2} + V(r)]\psi(\mathbf{x}) = E\psi(\mathbf{x}), \tag{21}$$

which, for $L = 0$ and $V(r) = \sigma r$, coincides with Eq. (5).

It is clear from Eq. (18) that the interaction term is always added to the entire kinetic energy of the quark, so that the resulting Salpeter equation in the form of Eq. (5), rather than in the form of Eq. (6), should not come as a surprise. Moreover, for massless quarks and no CSB, $\varphi_p = 0$ everywhere, so that $C_p = S_p = 1/\sqrt{2}$ and the interaction in Eq. (18) acquires a rather complex structure which does not reduce to a plain potential and supports parity doublers. Indeed, in the resulting equation, eigenstates with opposite parity, given by $\psi(\mathbf{p})$ and $(\sigma\hat{\mathbf{p}})\psi(\mathbf{p})$, come in pairs degenerate in mass [14], a feature inherent to vectorial interaction. In any case, the interaction given by matrix (16) does not contain a Lorentz time-vector part, which could have been dangerous from the point of view of the Klein paradox.

4. CONCLUSIONS

In this paper, using the Dyson–Schwinger approach to heavy–light quarkonia, we derive the effective one-particle equation for the light quark in the field of the static antiquark (Eq. (12)). In the heavy–quark limit of $m \longrightarrow \infty$ or in the heavy-string limit of $\sqrt{\sigma} \longrightarrow \infty$, the chiral angle is $\varphi_p = \pi/2$, and this equation reduces to the Dirac equation with purely scalar confinement. In the meantime, if the exact Foldy–Wouthuysen transformation is performed over the bound-state Eq. (12), the Schrödinger-like Eq. (18) arises with the interaction having a rather complex structure. In the same limiting case of $\varphi_p = \pi/2$, this interaction can be considerably simplified, reducing to a local potential. The spinless Salpeter Eq. (5) is derived this way, with the interaction term added to the entire quark kinetic energy. We notice also that, without CSB, explicit or spontaneous, the chiral angle would vanish identically, giving rise to a nonpotential dynamics (as follows from Eq. (18) with $\varphi_p = 0$) which has nothing to do with the dynamics described by the Salpeter Eq. (5) and the like. Since the approach of the QCD string with quarks at the ends is the generalization of the simple potential Salpeter equation to the case of the interquark interaction incorporating the proper dynamics of the string, we conclude that the effective interquark interaction generated by the QCD string has a scalar nature; that is, it appears entirely due to CSB. The detailed analysis of the Lorentz nature of confinement in quarkonia with the actual form of the chiral angle—the solution to the mass-gap equation—lies beyond the scope of the present paper, but we emphasize that, in order to have an accurate and self-consistent approach, one must consider and solve the full Dyson–Schwinger Eq. (8). Note that, although the fundamental color interaction in QCD mediated by gluons is manifestly vectorial, this does not automatically give rise to the Salpeter Eq. (5). Indeed, the effective interquark interaction, which appears after integrating out gluonic degrees of freedom and which can be described naturally, for example, with the help of the Dirac-like Eq. (12), appears dynamically, and, thus, no *a priori* conclusion can be made concerning its Lorentz nature. We argue, therefore, that one should be careful using the notions of “vector” and “scalar” confinement, always giving an explicit reference to the corresponding Dirac-like equation or Hamiltonian.

We thank Yu.S. Kalashnikova, M.G. Olsson, and E. Ribeiro for reading the manuscript and critical comments. The financial support of grant no. NS-1774.2003.2, as well as of the Federal Program of the Russian Ministry of Industry, Science, and Technology (project no. 40.052.1.1.1112), is acknowledged. The work of A.V.N. is also supported by die Deutsche Forschungsgemeinschaft (German Research Foundation, grant no. 436 RUS 113/820/0-1) and the Russian Foundation for Basic Research (project no. 05-02-04012-NNIOa).

REFERENCES

1. H. G. Dosch, Phys. Lett. B **190**, 177 (1987); H. G. Dosch and Yu. A. Simonov, Phys. Lett. B **205**, 339 (1988); Yu. A. Simonov, Nucl. Phys. B **307**, 512 (1988).
2. A. Yu. Dubin, A. B. Kaidalov, and Yu. A. Simonov, Phys. Lett. B **323**, 41 (1994); Phys. Lett. B **343**, 310 (1995); E. L. Gubankova and A. Yu. Dubin, Phys. Lett. B **334**, 180 (1994).
3. L. Brink, P. Di Vecchia, and P. Howe, Nucl. Phys. B **118**, 76 (1977).
4. Yu. S. Kalashnikova and A. V. Nefediev, Yad. Fiz. **60**, 1529 (1997) [Phys. At. Nucl. **60**, 1389 (1997)]; Yad. Fiz. **61**, 871 (1998) [Phys. At. Nucl. **61**, 785 (1998)].
5. Yu. A. Simonov, Nucl. Phys. B **324**, 67 (1989); Yad. Fiz. **66**, 363 (2003) [Phys. At. Nucl. **66**, 338 (2003)]; A. M. Badalian and Yu. A. Simonov, Yad. Fiz. **59**, 2247 (1996) [Phys. At. Nucl. **59**, 2164 (1996)].
6. Yu. S. Kalashnikova and A. V. Nefediev, Phys. Lett. B **492**, 91 (2000); Phys. Lett. B **530**, 117 (2002); Yad. Fiz. **68**, 681 (2005) [Phys. At. Nucl. **68**, 650 (2005)]; Yu. S. Kalashnikova, A. V. Nefediev, and Yu. A. Simonov, Phys. Rev. D **64**, 014037 (2001).
7. M. G. Olsson, Phys. Rev. D **55**, 5479 (1997); V. L. Morgunov, A. V. Nefediev, and Yu. A. Simonov, Phys. Lett. B **459**, 653 (1999); F. Buisseret and C. Semay, Phys. Rev. D **70**, 077501 (2004); hep-ph/0505168.
8. T. J. Allen and M. G. Olsson, Phys. Rev. D **68**, 054022 (2003); T. J. Allen, M. G. Olsson, J. R. Schmidt, *et al.*, Phys. Rev. D **70**, 054012 (2004).
9. Yu. A. Simonov, Yad. Fiz. **60**, 2252 (1997) [Phys. At. Nucl. **60**, 2069 (1997)]; Phys. Rev. D **65**, 094018 (2002); Yad. Fiz. **67**, 868 (2004) [Phys. At. Nucl. **67**, 846 (2004)]; J. A. Tjon and Yu. A. Simonov, Phys. Rev. D **62**, 014501 (2000).
10. I. I. Balitsky, Nucl. Phys. B **254**, 166 (1985).
11. N. Brambilla and A. Vairo, Phys. Lett. B **407**, 167 (1997); Yu. S. Kalashnikova and A. V. Nefediev, Phys. Lett. B **414**, 149 (1997).
12. M. Campostrini, A. Di Giacomo, and G. Mussardo, Z. Phys. C **25**, 173 (1984); M. Campostrini, A. Di Giacomo, and S. Olejnik, Z. Phys. C **31**, 577 (1986); A. Di Giacomo, E. Meggiolaro, and H. Panagopoulos, Nucl. Phys. B **483**, 371 (1997); G. Bali, N. Brambilla, and A. Vairo, Phys. Lett. B **421**, 265 (1998).
13. A. Amer, A. Le Yaouanc, L. Oliver, *et al.*, Phys. Rev. Lett. **50**, 87 (1983); A. Le Yaouanc, L. Oliver, O. Pene, and J.-C. Raynal, Phys. Lett. B **134B**, 249 (1984); Phys. Rev. D **29**, 1233 (1984); A. Le Yaouanc, L. Oliver, S. Ono, *et al.*, Phys. Rev. D **31**, 137 (1985); P. Bicudo and J. E. Ribeiro, Phys. Rev. D **42**, 1611 (1990); Phys. Rev. D **42**, 1625 (1990); Phys. Rev. D **42**, 1635 (1990); P. Bicudo, Phys. Rev. Lett. **72**, 1600 (1994); Phys. Rev. C **60**, 035209 (1999); P. J. A. Bicudo, A. V. Nefediev, and J. E. F. T. Ribeiro, Phys. Rev. D **65**, 085026 (2002); A. V. Nefediev and J. E. F. T. Ribeiro, Phys. Rev. D **70**, 094020 (2004).
14. Yu. S. Kalashnikova, A. V. Nefediev, and J. E. F. T. Ribeiro, Phys. Rev. D **72**, 034020 (2005).
15. Yu. A. Simonov, Yad. Fiz. **67**, 868 (2004) [Phys. At. Nucl. **67**, 846 (2004)]; S. M. Fedorov and Yu. A. Simonov, Pis’ma Zh. Éksp. Teor. Fiz. **78**, 67 (2003) [JETP Lett. **78**, 57 (2003)].

JETP Letters, Vol. 82, No. 9, 2005, pp. 562–564. Translated from Pis'ma v Zhurnal Éksperimental'noĭ i Teoreticheskoĭ Fiziki, Vol. 82, No. 9, 2005, pp. 638–641.
Original Russian Text Copyright © 2005 by Baranov, Bellucci, Biryukov, Britvich, Balasubramanian, Guidi, Giannini, Zapolsky, Kotov, Kushnirenko, Maisheev, Martinelli, Milan, Pikalov, Terekhov, Uggerhoj, Chepegin, Chesnokov.

First Results of Investigation of Radiation from Positrons in a Crystalline Undulator

V. T. Baranov[a], S. Bellucci[b], V. M. Biryukov[a], G. I. Britvich[a], C. Balasubramanian[b], V. Guidi[c], G. Giannini[b], V. N. Zapolsky[a], V. I. Kotov[a], A. E. Kushnirenko[a], V. A. Maisheev[a], G. Martinelli[c], E. Milan[c], V. A. Pikalov[a], V. I. Terekhov[a], U. Uggerhoj[d], V. N. Chepegin[a], and Yu. A. Chesnokov[a]

[a] *Institute for High Energy Physics, Protvino, Moscow region, 142281 Russia*
e-mail: chesnokov@ihep.ru
[b] *INFN—Laboratori Nazionali di Frascati, P.O. Box 13, 00044 Frascati, Italy*
[c] *Department of Physics and INFN, Via Paradiso 12, I-44100 Ferrara, Italy*
[d] *Aarhus University, 8000 Aarhus C., Denmark*

Received October 13, 2005

Radiation emitted by positrons moving in a periodically deformed crystal has been experimentally observed for the first time. Radiation spectra have been measured in a wide energy range. Experimental evidence has been obtained for an undulator peak in a radiation spectrum, which is qualitatively consistent with calculations. Crystalline undulators ensure an equivalent magnetic field of 1000 T and a period in the submillimeter range and can therefore be used to generate x-ray and gamma radiation that is a hundred times harder than radiation in usual undulators. *© 2005 Pleiades Publishing, Inc.*

PACS numbers: 07.85.–m, 41.60.–m, 61.85.+p

At present, intense x-ray beams are used for investigations in biology, medicine, materials science, and other fields of science and engineering. The traditional method for generating such beams (with energies of several keV or higher) is the use of special magnets (undulators) at accelerators [1].

The energy of photons generated in an undulator is proportional to the square of the Lorentz factor γ and is inversely proportional to the undulator period L, i.e., $\hbar\omega = 2\pi\hbar\gamma^2 c/L$. In the ordinary electromagnetic undulator, the period reaches several centimeters. Thus, photons with an energy of about 1 keV are obtained with an accelerator beam of an energy of about 1 GeV.

For a number of investigations, it is important to increase the beam energy. The concept of the production of undulators based on crystals, where a strong periodic electric field naturally exists, has been actively discussed for the past 25 years [2–9]. The practical possibility of producing such a device was first demonstrated in our work [10].

The proposed undulator is a crystalline Si wafer 0.5 mm in thickness with the (111) surface and special scratches deposited with a period of 0.1–1 mm on the sides of the wafer. These scratches give rise to periodic wafer deformations (with an amplitude of 100 Å or higher) close to the sine form. The first experimental samples of the crystalline undulator have already been produced and the presence of the sinuous bend was determined by x-ray analysis [11]. The decisive tests that were carried out on a proton beam proved the "transparency" of crystalline undulators for the transmission of high-energy particles in the channeling mode [12]. In the experiment carried out in the fall of 2004 at the U-70 IHEP accelerator, photon emission by positrons from a crystalline undulator was observed.

Figure 1 shows the experiment layout. A positron beam with a central pulse of 10 GeV/c is directed to a crystalline undulator. The beams of gamma-rays and positrons (which partially lose energy due to interaction in the undulator) are separated by means of a horizontal magnet. Gamma-ray photons from the undulator are detected by the electromagnetic calorimeter $G1$. As this calorimeter, two calorimeters based on yttrium aluminate $YAlO_3$ and BGO crystals are used in the experiment (not simultaneously). The yttrium calorimeter

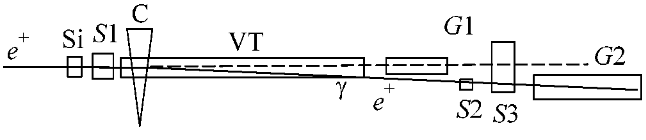

Fig. 1. Experiment layout for observing radiation from the crystalline undulator: e^+ is the positron beam, Si is the undulator and goniometer, C is the horizontal magnet (corrector), VT is the vacuum tube, γ is gamma radiation at the undulator exit, $S1$–$S3$ are the scintillator counters, and $G1$ and $G1$ are the gamma detectors.

0021-3640/05/8209-0562$26.00 © 2005 Pleiades Publishing, Inc.

was adapted for detecting photons in a range of 0.06–2 MeV, whereas the BGO detector could detect gamma-ray photons with energies of several MeV or higher.

The electromagnetic calorimeter *G*2, "Shashlyk" [13], detected positrons. The trigger was a coincidence between counters *S*1*S*3. In addition, the amplitude of ionization losses was recorded in the counter *S*2. The positron beam was obtained at an energy of 10 GeV. At an average discharge of (3–4) × 10^{11} protons on the aluminum target, near 10^5 positrons were present in a beam line. The energy spectrum of the positron beam was measured by the calorimeter "Shashlyk" with a resolution of several percent.

A specificity of the problem is the unordinary geometry of the source. It has a small transverse size of 0.3 mm and a large longitudinal size of several millimeters along the beam, because about ten undulator periods with a step of 0.5 mm and an amplitude of several tens of angstroms are required. Previous experiments concerning emission accompanying channeling in crystals were carried out with short targets with a length of less than 1 mm.

For this reason, the first problem is the identification of the source, because only a small fraction (~1/500) of beam particles passes through the crystal. We easily found the source of radiation using a thin scintillator 500 μm in width as a trigger and remotely displacing the crystal across the beam. The orientation curve plotted in Fig. 2 proves that the source of radiation is the oriented crystal.

The second feature associated with the large length of the crystal gives rise to multiple photon production, distorting the measured spectra. For this reason, measurements of the emitted energy are more informative. These measurements in comparison with the calculations in Fig. 3 certainly point to the presence of channeling in the deformed crystal. Only channeling can be responsible for such a narrow angular scan of fractions of a milliradian.

Figure 4 shows the emitted-photon spectra in the oriented and disoriented crystals, as well as the background spectra measured by the BGO detector without a crystal. An increase in the spectral density is observed in a range of hundreds of MeV, corresponding to channeling.

The signal on the yttrium detector, adapted for detecting undulator radiation, is strongly distorted. Figure 5 shows the emitted-energy spectra measured in the oriented and disoriented crystals. According to calculations [14], these distortions are attributed to the presence of coherent radiation accompanying channeling that provides a multiplicity factor of 3, which is much larger than 1, at a positron energy of 10 GeV reached in beam line 22. Correspondingly, most undulator events (0.5 photons per positron) are accompanied by several photons with higher energies and are detected with distortions.

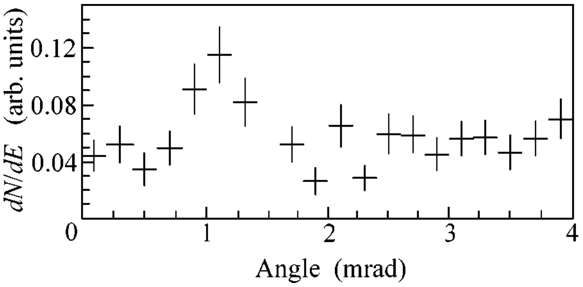

Fig. 2. Number of detected photons vs. the crystal orientation. Ten counts correspond to an angle of 1 μrad.

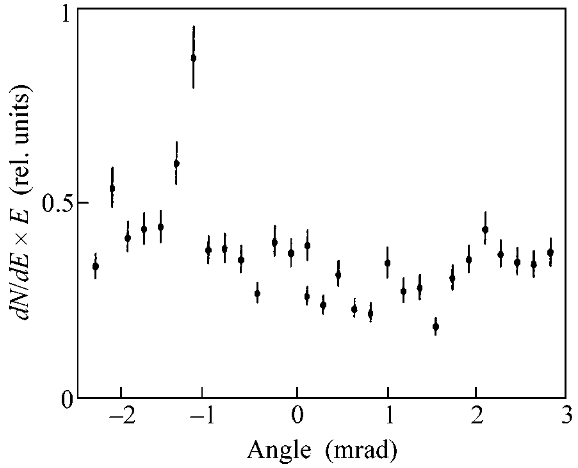

Fig. 3. Orientation curve of emitted energy as measured by the BGO detector.

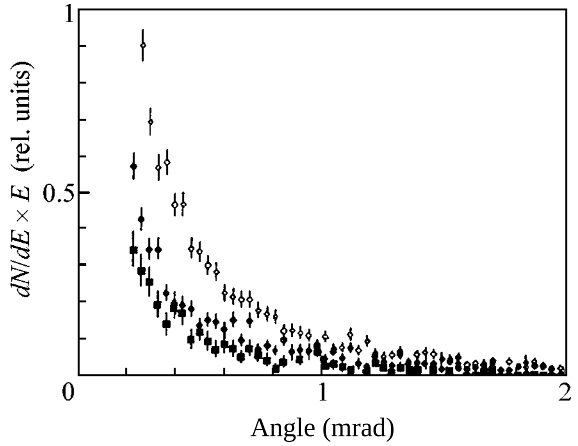

Fig. 4. Emitted-energy spectrum in the (open circles) oriented and (closed circles) disoriented crystals, as well as (squares) the background measured by the BGO detector without a crystal.

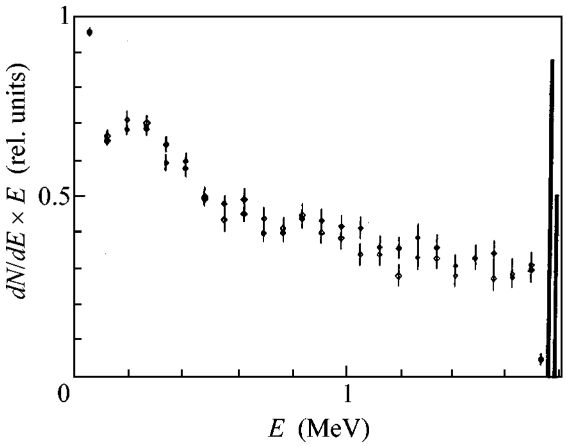

Fig. 5. Emitted-energy spectra in the (open circles) oriented and (closed circles) disoriented crystals as measured by the yttrium detector. Two columns in the right are signals above 2 MeV (oriented/disoriented cases) on a 1 : 50 scale.

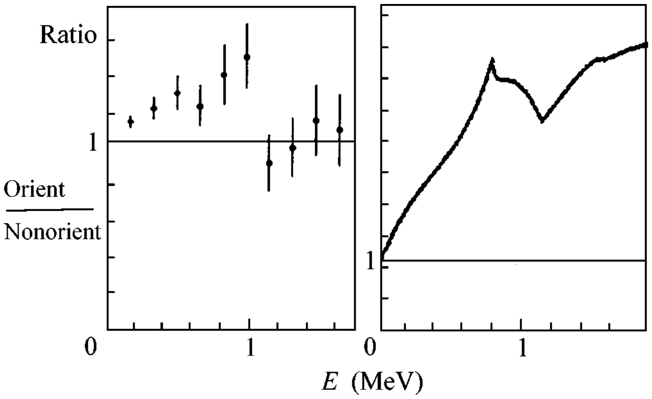

Fig. 6. (Left panel) Measured and (right panel) calculated ratios of the emitted-energy spectra in the oriented and disoriented crystals as measured by the yttrium detector.

However, applying a special selection rule for events with low energy losses of a primary positron by means of the high-precision spectrometer Shashlyk (about 30% of the overall statistics), we obtain spectra that are experimental indications to the existence of an undulator peak near an energy of 1 MeV. These data are shown in Fig. 6 in comparison with the calculations corroborating the existence of the radiation peak at this energy. This comparison is possible only at the qualitative level, because the apparatus function of the detector (limited detection efficiency of gamma rays and Compton tail) is ignored.

The setup layout used here will be updated in future accelerator runs. In particular, the use of a narrow calorimeter is planned for limiting the angular distribution of gamma radiation. In order to reconstruct an undistorted gamma spectrum, we are going to apply the Compton scatterer method [15]. In addition, the crystals are planned to be optimized according to the recommendations given in [14].

Radiation from positrons in a periodically deformed crystal has been experimentally observed. Under heavy background conditions due to the multiple production of photons, experimental evidence has been obtained for the existence of the undulator radiation peak, which is consistent with calculations. In order to continue these measurements under pure conditions, the optimization of the setup, beam line, and crystals is planned. These investigations are expected to be continued in other accelerator centers under other conditions [11, 16].

We are grateful to A.M. Zaĭtsev and N.E. Tyurin for attention and support of the work. This work was supported by the Russian Foundation for Basic Research (project nos. 05-02-17622 and 05-02-08085ofi-e).

REFERENCES

1. Beam Line (Stanford) **32**, No. 1 (2002).
2. V. V. Kaplin, S. V. Plotnikov, and S. A. Vorobiev, Zh. Tekh. Fiz. **50**, 1079 (1980) [Sov. Phys. Tech. Phys. **25**, 650 (1980)].
3. V. G. Baryshevsky, I. Ya. Dubovskaya, and A. O. Grubich, Phys. Lett. A **77**, 61 (1980).
4. H. Ikezi, Y. R. Lin-Liu, and T. Ohkawa, Phys. Rev. B **30**, 1567 (1984).
5. S. A. Bogacz and J. B. Ketterson, J. Appl. Phys. **60**, 177 (1986); S. A. Bogacz, Part. Accel. **42**, 181 (1993).
6. G. B. Dedkov, Phys. Status Solidi B **184**, 535 (1994).
7. A. V. Korol, A. V. Solovev, and W. Greiner, Int. J. Mod. Phys. **8**, 49 (1999).
8. U. Mikkelsen and E. Uggerhoj, Nucl. Instrum. Methods Phys. Res. B **160**, 435 (2000).
9. R. O. Avakian, K. T. Avetyan, K. A. Ispirian, and E. G. Melikyan, Nucl. Instrum. Methods Phys. Res. A **492**, 11 (2002).
10. S. Bellucci, S. Bini, V. M. Biryukov, *et al.*, Phys. Rev. Lett. **90**, 034801 (2003).
11. S. Bellucci, S. Bini, G. Giannini, *et al.*, Phys. Rev. ST Accel. Beams **7**, 023501 (2004).
12. A. G. Afonin, V. T. Baranov, S. Bellucci, *et al.*, Nucl. Instrum. Methods Phys. Res. B **234**, 122 (2005).
13. G. S. Atoian, V. V. Issakov, and O. V. Karavichev, Nucl. Instrum. Methods Phys. Res. A **531**, 467 (2004).
14. S. Bellucci and V. A. Maisheev, *Talk on Workshop on Relativistic Channeling and Related Coherent Phenomena* (INFN, Frascati, 2005).
15. S. V. Blazhevich, G. L. Bochek, A. P. Potylitsin, *et al.*, Tech. Phys. **38**, 374 (1993).
16. J. U. Andersen, S. P. Moller, A. H. Sorensen, *et al.*, CERN Note: CERN-SPSC-2005-030 (2005).

Translated by R. Tyapaev

JETP Letters, Vol. 82, No. 9, 2005, pp. 565–569. Translated from Pis'ma v Zhurnal Éksperimental'noĭ i Teoreticheskoĭ Fiziki, Vol. 82, No. 9, 2005, pp. 642–646.
Original Russian Text Copyright © 2005 by Brazhnikov, Kolmakov, Levchenko, Mezhov-Deglin.

Suppression of High-Frequency Turbulent Oscillations of the Fluid Surface by Additional Low-Frequency Pumping

M. Yu. Brazhnikov*, G. V. Kolmakov, A. A. Levchenko, and L. P. Mezhov-Deglin
Institute of Solid State Physics, Russian Academy of Sciences, Chernogolovka, Moscow region, 142432 Russia
** e-mail: makc@issp.ac.ru*

Received September 4, 2005

The dynamics of establishing steady-state turbulent cascade has been studied in a system of capillary waves on the surface of liquid hydrogen after additional pumping whose frequency is lower than the frequency of the main pumping is switched off/on. It has been found that, when the additional low-frequency pumping *is switched on*, the amplitude of waves in the high-frequency part of the turbulent spectrum *decreases*, which gives rise to the narrowing of the inertial frequency range. The experimental data qualitatively agree with the numerical calculations performed in the kinetic-equation approximation including the viscous damping of waves. *© 2005 Pleiades Publishing, Inc.*

PACS numbers: 47.27.–i, 47.35.+i

INTRODUCTION

At present, turbulence on the surface of a fluid is studied in numerous experimental and theoretical investigations. Interest in this phenomenon is in particular stimulated by numerous applications, one of which is the prediction of weather using measurements of the spectrum of wind waves on the ocean surface. Investigation of the turbulence of capillary waves is of considerable interest, because dynamics at this wavelength scale is of fundamental importance in the transfer and dissipation of energy on the fluid surface.

As was shown in recent investigations [1–6], the charged surface of liquid hydrogen is an excellent model object for studying the dynamics of nonlinear waves on the fluid surface. Relatively low viscosity, low density, large nonlinearity coefficient of capillary waves on the surface of liquid hydrogen, and the possibility of exciting waves on the charged fluid surface by an alternating electric field enable us to observe the formation of a Kolmogorov cascade of capillary turbulence on the surface of hydrogen in a wide frequency range (10^2–10^4 Hz) [1, 2]. More recently, a change in the turbulent spectrum upon a change in the spectral characteristics of the exciting force [3], a change in the main mechanism of energy transfer in the system of capillary waves from the nonlinear transformation of waves to viscous damping at high frequencies [4], and quasiadiabatic decay of capillary turbulence when the external pumping is stepwise switched off [5, 6] were observed.

In the theory of weak wave turbulence [7, 8], the statistical distribution of occupation numbers n_ω for capillary waves can be described by the kinetic equation

$$\frac{\partial n_\omega}{\partial t} = \mathrm{st}(n) - 2\gamma_\omega n_\omega + F_{\mathrm{drive}}(t), \tag{1}$$

where st(n) is the collision integral, γ_ω is the viscous-damping coefficient for capillary waves, and $F_{\mathrm{drive}}(t)$ corresponds to the external pumping. The frequency ω and wave vector k of a capillary wave are related by the dispersion relation $\omega^2 = (\sigma/\rho)k^3$, where σ is the surface tension coefficient and ρ is the density of the fluid. The stationary solution of kinetic equation (1) in the inertial range describes the isotropic spectrum of capillary turbulence:

$$n_\omega = CQ^{1/2}\left(\frac{\sigma}{\rho}\right)^{1/2}\omega^{-15/6}, \tag{2}$$

where C is the numerical factor and $Q > 0$, which corresponds to the energy transfer from low- to high-frequency waves. The frequency distribution of the deviation $\langle|\eta_\omega|^2\rangle$ of the fluid surface from the equilibrium state found from distribution (2) has the form

$$\langle|\eta_\omega|^2\rangle = \frac{\rho\omega}{\sigma k^2}n_\omega = CQ^{1/2}\left(\frac{\sigma}{\rho}\right)^{1/6}\omega^{-17/6}. \tag{3}$$

Solution (3) is realized in the inertial frequency range in the case of broadband pumping by low-frequency noise [8, 3]. Numerical solution [9] of Eq. (1), as well as our previous measurements [1], showed that the case of spectrally narrow pumping exhibits a turbulent spectrum consisting of equidistant peaks whose amplitudes decrease as $\langle|\eta_\omega|^2\rangle \sim \omega^{-21/6}$, i.e., with an exponent differing from the Kolmogorov index.

At high frequencies, where the effect of the viscosity of the fluid is significant, the wave transfer of energy through the cascade changes to the viscous damping of

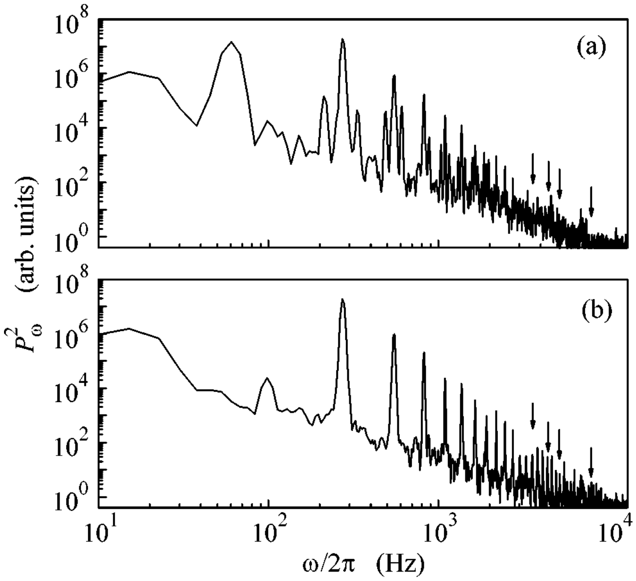

Fig. 1. Stationary spectrum of the oscillations of the fluid surface upon pumping (a) simultaneously at two resonance frequencies $\omega_1/2\pi = 61$ Hz and $\omega_2/2\pi = 274$ Hz and (b) at the main resonance frequency $\omega_2/2\pi = 274$ Hz.

waves, which limits the inertial range from the high-frequency side. As the pumping amplitude increases, the position of the high-frequency edge of the inertial range is shifted toward higher frequencies; i.e., the inertial range expands [4].

In this paper, we report the investigation of the evolution of the spectrum of capillary turbulence on the surface of liquid hydrogen when additional low-frequency pumping is switched off/on. It was found that, when additional low-frequency pumping is *switched on*, turbulence in the high-frequency range is *suppressed* and the inertial frequency range decreases. When additional low-frequency pumping is switched off, the amplitudes of high-frequency turbulent oscillations increase and the inertial range expands. The results of the numerical investigation of the effect of additional low-frequency pumping on the stationary spectrum of capillary turbulence are also reported. In calculations, kinetic equation (1) for capillary waves with allowance for viscous damping of waves is used. The results of the numerical calculations qualitatively agree with the experimental data.

EXPERIMENT

The apparatus design and measurement procedure are similar to those used in our previous investigations [1–6] and were described in detail in [10]. An optical cell was placed in a vacuum cavity of a helium cryostat. Gaseous hydrogen was condensed between the plates of a horizontal cylindrical capacitor placed inside the cell. The collection of hydrogen was stopped when the fluid level between the capacitor plates reached the guard ring.

A radioactive target was attached to the lower plate of the capacitor. Positive electric voltage applied to the lower plate extracts positive ions from the ionized fluid layer adjacent to the target surface and draws them to the surface of liquid hydrogen, so that a quasi-two-dimensional charged layer is formed under the surface. To prevent the drift of charges to the container walls, a voltage equal to the voltage at the lower plate was applied to the guard ring. The field of the charged layer completely compensates the electric field inside the fluid. The thickness of the layer of liquid hydrogen is equal to 6 mm and the distance of the fluid surface from the upper plate of the capacitor is equal to 3.2 mm. The measurements were carried out at a constant fluid temperature of $T = 15.5$ K.

Oscillations of the surface of liquid hydrogen were excited by an alternating electric voltage applied between the guard ring and upper capacitor plate in addition to the constant voltage. Surface oscillations were detected by a change in the power of a laser beam reflected from the surface. The reflected beam was focused by a lens onto a photodetector. The ac voltage component on the photodetector was amplified and written to computer memory using a 16-bit analog-to-digital converter.

The spectrum of the oscillations of the fluid surface was determined from the Fourier spectrum of the reflected laser-beam power [10]. These measurements were carried out in the “wide-beam” regime (the light-spot diameter is much larger than the wavelength on the fluid surface), for which the Fourier harmonic P_ω of the reflected power is proportional to the Fourier harmonic η_ω of the surface deviation and, correspondingly,

$$\langle |\eta_\omega|^2 \rangle = \mathrm{const}|P_\omega|^2. \quad (4)$$

To study the evolution of the spectrum of the surface oscillations when additional low-frequency pumping is switched on/off, we used the short-time Fourier transform procedure [11]. This procedure is applicable because our previous observations [5, 6] show that the characteristic decay time of the turbulent oscillations of the fluid surface is on the order of the viscous damping time of capillary waves, whose frequency is equal to the pumping frequency, and is much longer than the period of the surface oscillations. This relation allows the choice of a time window smaller than the signal decay time but much larger than the period of the exciting force. By shifting the window position in time, one can study the evolution of the turbulent cascade on the surface of liquid hydrogen when the additional low-frequency pumping is switched off/on.

OBSERVATION RESULTS AND DISCUSSION

Two types of measurements were conducted in these experiments. In measurements of the first type, waves on the fluid surface were excited by pumping simultaneously at two different resonance frequencies of the cell. After the formation of the steady turbulent distribution, pumping at one of the frequencies (additional frequency) was stepwise switched off, whereas the intensity of pumping at the other (main) frequency remained unchanged. In measurements of the second type, waves on the fluid surface were first excited at one of the resonance frequencies of the cell and then additional pumping at another resonance frequency was switched on. Thus, in both cases, a transient process was studied in the turbulent system of capillary waves after the additional pumping was switched off or on.

Figure 1 shows the stationary spectra of the steady oscillations of the surface of liquid hydrogen before and after the additional pumping is switched off (a) for simultaneous pumping at two resonance frequencies of the cell: main $\omega_2/2\pi$ = 274 Hz and additional $\omega_1/2\pi$ = 61 Hz and (b) after the pumping at the additional frequency ω_1 is switched off. It is worth noting that the wave energy $E_{\omega_1} \propto \omega_1^{4/3}|\eta_{\omega_1}|^2$ at the frequency ω_1 is an order of magnitude lower than the wave energy E_{ω_2} at the frequency ω_2. For this reason, the oscillation spectrum in Fig. 1a can be treated as the capillary-turbulence spectrum that is generated by the main harmonic pumping at the frequency $\omega_2/2\pi$ = 274 Hz and is perturbed by the additional pumping at the frequency $\omega_1/2\pi$ = 61 Hz. Correspondingly, near the relatively high peaks at frequencies that are multiples of ω_2, relatively low peaks at combination frequencies are located on both sides of the harmonics of the main frequency at a distance of the frequency ω_1 from it. The distribution in Fig. 1b is the stationary spectrum of capillary turbulence generated by the harmonic force at the frequency ω_2: the amplitude of peaks at frequencies that are multiples of the frequency ω_2 decreases in a power law as the frequency increases. It is seen that the amplitudes of the high-frequency peaks generated by pumping at one frequency (Fig. 1b) are noticeably larger than those generated by pumping at two frequencies (Fig. 1a).

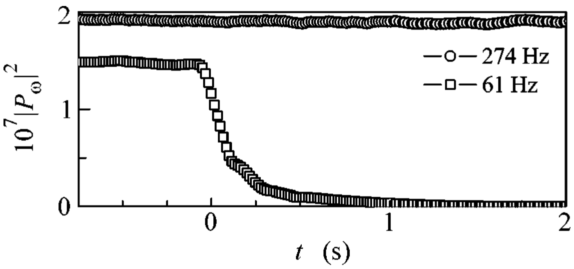

Fig. 2. Time dependence of the amplitude squared for waves on the surface of liquid hydrogen at the (circles) main and (squares) additional frequencies when the additional pumping is switched off at the time $t = 0$.

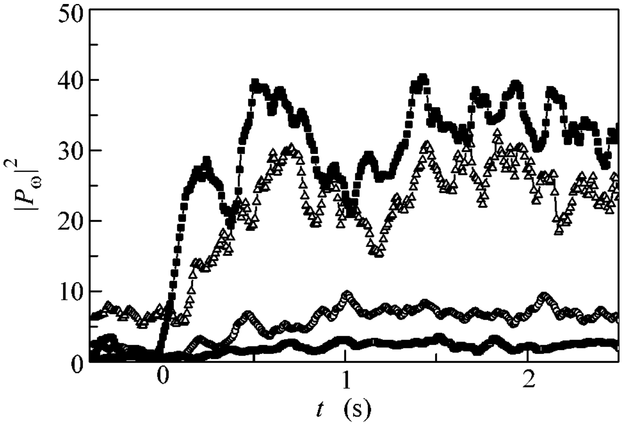

Fig. 3. Time dependence of the amplitude squared for peaks at frequencies that are multiples of the main pumping frequency ω_2 when the additional pumping at the frequency ω_1 is switched off at the time $t = 0$. The triangles, closed squares, open squares, and circles correspond to the 13th (3.57 kHz), 16th (4.49 kHz), 19th (5.19 kHz), and 29th (7.96 kHz) harmonics of the frequency ω_2, respectively. The positions of the corresponding harmonics are shown by arrows in Fig. 1.

Figure 2 shows the time dependence of the amplitude squared for waves on the surface of liquid hydrogen at the (circles) main and (squares) additional frequencies [we recall that $P_\omega^2 \propto |\eta_\omega|^2$ according to Eq. (4)]. Pumping at the additional frequency ω_1 is switched off at time $t = 0$, whereas the pumping amplitude at the main frequency ω_2 remains unchanged. As is seen in the figure, the amplitude of the wave with the frequency ω_1 decreases almost exponentially with time and, in agreement with [6], the characteristic decay time nearly coincides with the viscous damping time $\gamma_{\omega_1}^{-1}$ of the capillary wave with the frequency ω_1.

Figure 3 shows the time dependence of the amplitude squared for peaks at frequencies that are multiples of the main pumping frequency ω_2 when the additional pumping is switched off at the time $t = 0$. The triangles, closed squares, open squares, and circles correspond to the 13th (3.57 kHz), 16th (4.49 kHz), 19th (5.19 kHz), and 29th (7.96 kHz) harmonics of the frequency ω_2, respectively. The positions of the corresponding harmonics are shown by arrows in Fig. 1. As seen in Fig. 3, after the additional pumping is *switched off*, the amplitudes of the high-frequency harmonics *increase* by several times in time comparable with the damping time for the wave at the frequency ω_1 (Fig. 2).

Figure 4 shows the fragment of the spectrogram of the surface oscillations for frequencies 3–10 kHz in the time interval from –0.8 to 4 s. The ordinate axis shows the logarithm of the frequency and the abscissa axis presents the time in seconds. The gray color density is proportional to the amplitude squared for waves with corresponding frequencies. After the additional pumping is switched off ($t > 0$), the spectrogram exhibits the

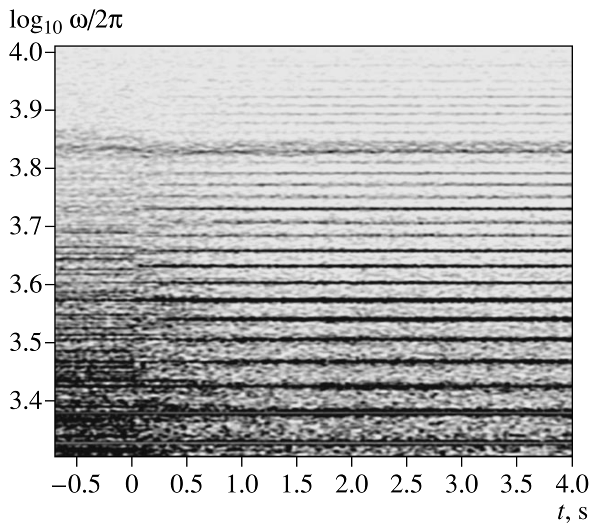

Fig. 4. Spectrogram of the oscillations of the surface of liquid hydrogen upon simultaneous pumping at frequencies $\omega_1/2\pi = 61$ Hz and $\omega_2/2\pi = 274$ Hz. Darker regions correspond to larger wave amplitudes. The gray color density is proportional to the amplitude squared for waves with corresponding frequencies.

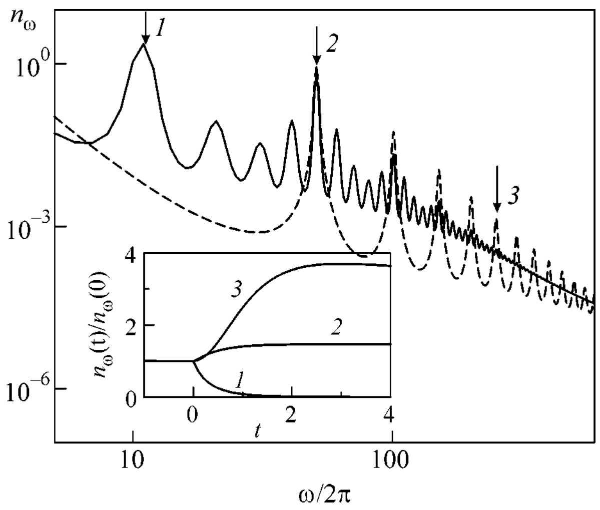

Fig. 5. Numerically calculated stationary spectra of capillary turbulence generated by pumping at (solid line) two frequencies $\omega_1/2\pi = 10$ Hz and $\omega_2/2\pi = 50$ Hz simultaneously and (dashed line) frequency ω_2. The inset shows the time dependence of the relative height of the (*1*) 10-, (*2*) 50-, and (*3*) 250-Hz (fifth harmonic of the main pumping) peaks when the additional pumping is switched off at the time $t = 0$. The corresponding peaks are marked by the arrows in the main part of the figure.

regular density maxima (black horizontal straight lines) at frequencies that are multiples of the main pumping frequency ω_2, which corresponds to an increase in the amplitude of the high-frequency surface oscillations with time.

In addition, analysis of the evolution of the spectrum of the fluid-surface oscillations shows that, when the additional pumping is switched on at the time $t = 0$, the amplitudes of the high-frequency oscillations decrease at $t > 0$. Thus, the observed evolution of the turbulent spectrum is completely reversible.

Further analysis (see Fig. 5) shows that the experimental data agree with the numerical calculations performed with kinetic equation (1), where the effect of viscous losses on the damping of capillary waves on the surface of liquid hydrogen is taken into account. The solid line in Fig. 5 is the dimensionless stationary spectrum of surface oscillations (occupation number n_ω as a function of the wave frequency $\omega/2\pi$) generated by pumping at the two frequencies $\omega_1/2\pi = 10$ Hz and $\omega_2/2\pi = 50$ Hz simultaneously. The dashed line is the stationary spectrum of surface oscillations formed after pumping at a frequency of 10 Hz is switched off, whereas the intensity of pumping at a frequency of 50 Hz remains unchanged. It is seen that the amplitude of the fluid-surface oscillations at frequencies $\omega/2\pi > 100$ Hz increases after the additional pumping is switched off. The inset shows the time dependence of the relative height of the (*1*) 10-, (*2*) 50-, and (*3*) 250-Hz (fifth harmonic of the main pumping) peaks after pumping at a frequency of 10 Hz is switched off at the time $t = 0$. The corresponding peaks are marked by the arrows in the main part of the figure. The amplitudes $n_\omega(t)$ of the peaks in the inset are normalized to their initial values $n_\omega(0)$. The time in the inset is given in dimensionless units. It is seen that, after the low-frequency pumping is switched off, the amplitudes of the high-frequency turbulent oscillations increase by several times.

The increase in the amplitudes of the high-frequency turbulent oscillations after the additional low-frequency pumping is switched off can be qualitatively attributed to a decrease in the density of states (number of harmonics excited in the unit frequency range) involved in the nonlinear energy transfer form low- to high-frequency oscillations in the inertial frequency range. Indeed, simultaneous pumping at two frequencies excites oscillations at frequencies that are multiples of the pumping frequencies and at combination frequencies. When the additional pumping is switched off, the amplitudes of the oscillations at this frequency, as well as at multiple harmonics and combination frequencies, decrease rapidly. This damping gives rise to the redistribution of oscillation energy over frequencies, which is manifested in the evolution of the turbulent spectrum and in a noticeable increase in the amplitudes of waves with frequencies that are multiples of the main pumping frequency ω_2.

CONCLUSIONS

The relaxation of the turbulent oscillations on the surface of liquid hydrogen has been studied for the case where the additional low-frequency perturbation is switched on/off. It has been found for the case of spectrally narrow pumping that, after the additional pumping is *switched off*, the wave amplitudes in the high-frequency part of the turbulent spectrum *increase* and thereby the inertial frequency range expands. The observed evolution of the spectrum is reversible: after the additional perturbation is *switched on*, the wave amplitudes in the high-frequency part of the turbulent spectrum *decrease* and the inertial range narrows. Thus, it has been shown that high-frequency turbulent oscillations on the fluid surface are suppressed in the presence of additional low-frequency pumping.

We are grateful to V.E. Zakharov and E.A. Kuznetsov for stimulating discussions and to V.N. Khlopinskiĭ for assistance in preparing experiments. This work was supported in part by the Russian Foundation for Basic Research (project no. 05-02-17849) and by the Presidium of the Russian Academy of Sciences (program “Quantum Macrophysics”). The work of M.Yu.B. was supported by the Foundation for Assistance to Russian Science.

REFERENCES

1. M. Yu. Brazhnikov, G. V. Kolmakov, A. A. Levchenko, and L. P. Mezhov-Deglin, Pis’ma Zh. Éksp. Teor. Fiz. **74**, 443 (2001) [JETP Lett. **73**, 398 (2001)].
2. M. Yu. Brazhnikov, A. A. Levchenko, G. V. Kolmakov, and L. P. Mezhov-Deglin, Fiz. Nizk. Temp. **27**, 1183 (2001) [Low Temp. Phys. **27**, 876 (2001)].
3. M. Yu. Brazhnikov, G. V. Kolmakov, and A. A. Levchenko, Zh. Éksp. Teor. Fiz. **122**, 521 (2002) [JETP **95**, 447 (2002)].
4. M. Yu. Brazhnikov, G. V. Kolmakov, A. A. Levchenko, and L. P. Mezhov-Deglin, Pis’ma Zh. Éksp. Teor. Fiz. **74**, 660 (2001) [JETP Lett. **74**, 583 (2001)].
5. G. V. Kolmakov, A. A. Levchenko, M. Yu. Brazhnikov, *et al.*, Phys. Rev. Lett. **93**, 074501 (2004).
6. M. Yu. Brazhnikov, G. V. Kolmakov, A. A. Levchenko, and L. P. Mezhov-Deglin, Pis’ma Zh. Éksp. Teor. Fiz. **80**, 99 (2004) [JETP Lett. **80**, 90 (2004)].
7. V. E. Zakharov and N. N. Filonenko, J. Appl. Mech. Tech. Phys. **4**, 506 (1967).
8. V. E. Zakharov, G. Falkovich, and V. S. L’vov, *Kolmogorov Spectra of Turbulence*, Vol. 1: *Wave Turbulence* (Springer, Berlin, 1992).
9. G. E. Fal’kovich and A. B. Shafarenko, Zh. Éksp. Teor. Fiz. **94**, 172 (1988) [Sov. Phys. JETP **67**, 1393 (1988)].
10. M. Yu. Brazhnikov, A. A. Levchenko, and L. P. Mezhov-Deglin, Prib. Tekh. Éksp., No. 6, 31 (2002) [Instrum. Exp. Tech. **45**, 758 (2002)].
11. S. Mallat, *A Wavelet Tour of Signal Processing* (Academic, New York, 1997).

Translated by R. Tyapaev

JETP Letters, Vol. 82, No. 9, 2005, pp. 570–574. Translated from Pis'ma v Zhurnal Éksperimental'noĭ i Teoreticheskoĭ Fiziki, Vol. 82, No. 9, 2005, pp. 647–651.
Original Russian Text Copyright © 2005 by Ilgisonis, Khalzov.

Formal Stability of Three-Dimensional Flows of an Ideal Conducting Fluid

V. I. Ilgisonis and I. V. Khalzov
Russian Research Centre Kurchatov Institute, Moscow, 123182 Russia

Received September 26, 2005

The linearized dynamics of an ideal fluid is shown to have an infinite set of invariants different from the usual Casimir invariants. The procedure of their construction is described. The inclusion of one or several such invariants makes it possible to obtain a sufficient condition for the stability of flows of the fluid in the framework of usual or magnetic hydrodynamics. The condition appears to be softer (closer to a necessary condition) than the previously known conditions. © *2005 Pleiades Publishing, Inc.*

PACS numbers: 46.15.Cc, 52.30.Cv

Deviation of a conservative physical system from the equilibrium position can effectively increase in time, which points to the instability of such an equilibrium position. When the deviation amplitude is small enough, the dynamics of the system is approximately described by linearized equations, which makes spectral methods attractive for analyzing stability. Correct analysis of the spectral stability in continuum media is methodically difficult, because it is necessary to determine not only eigenvalues but also eigenvectors that must satisfy certain boundary conditions. As a result, instead of a discrete spectrum usual for finite-dimensional systems, a spectrum in hydrodynamics is often continuous or absent altogether. At the same time, to reveal whether an equilibrium state is stable or unstable, variational methods, e.g., Lyapunov theory, can be used. An analog of the Lyapunov theorem for a linearized system is sometimes called the formal stability condition. According to this condition, the equilibrium state is called formally stable if the linearized dynamics of the system has an invariant U whose first variation is equal to zero at the equilibrium point and the second variation has definite sign. The formal stability assures spectral stability. In contrast to the classical Lagrange result for finite-dimensional systems, the general statement for nonlinear stability is absent and additional analysis is necessary. Moreover, only sign semidefiniteness ($\delta^2 U \geq 0$) rather than sign definiteness ($\delta^2 U > 0$) is characteristic of hydrodynamics, which assures the absence of exponentially increasing perturbations but does not provide, conclusion about the possibility of perturbations growing slower. Nevertheless, even such a problem has not yet been solved with sufficient completeness. We hope that the approach proposed in this work will promote advance in its solution.

At the same time, there are also continual examples where the formal stability condition is exhaustive. Among them is the static equilibrium of an ideal conducting fluid (plasma) in a magnetic field [1]. We are inspired by this circumstance and consider the linearized equation of magnetic hydrodynamics (MHD) that has the following form in terms of the liquid-element displacement $\boldsymbol{\xi}(t, \mathbf{r})$ (see, e.g., [2]):

$$\rho\ddot{\boldsymbol{\xi}} + 2\rho(\mathbf{V}\cdot\nabla)\dot{\boldsymbol{\xi}} - \mathbf{F}(\boldsymbol{\xi}) = 0. \tag{1}$$

Here, the dot stands for the partial time derivative and

$$\begin{aligned}\mathbf{F}(\boldsymbol{\xi}) = {} & -\delta\rho(\mathbf{V}\cdot\nabla)\mathbf{V} - \rho(\delta\mathbf{V}\cdot\nabla)\mathbf{V} \\ & -\rho(\mathbf{V}\cdot\nabla)\delta\mathbf{V} - \nabla\delta p \\ & +((\nabla\times\delta\mathbf{B})\times\mathbf{B} + (\nabla\times\mathbf{B})\times\delta\mathbf{B})\frac{1}{4\pi} - \delta\rho\nabla\Phi,\end{aligned} \tag{2}$$

is the linearized force operator composed of the perturbed physical quantities

$$\delta\rho = -\nabla\cdot(\rho\boldsymbol{\xi}), \quad \delta\mathbf{V} = (\mathbf{V}\cdot\nabla)\boldsymbol{\xi} - (\boldsymbol{\xi}\cdot\nabla)\mathbf{V},$$

$$\delta p = -\boldsymbol{\xi}\cdot\nabla p - \gamma p\nabla\cdot\boldsymbol{\xi}, \quad \delta\mathbf{B} = \nabla\times(\boldsymbol{\xi}\times\mathbf{B}).$$

We use the notation $\delta\mathbf{V}$ for that part of the total perturbation of the velocity (with the subtraction of $\dot{\boldsymbol{\xi}}$) which is associated only with the spatial inhomogeneity of the initial flow and its perturbation. The steady-state fluid density ρ, velocity $\mathbf{V}$, pressure p, magnetic field $\mathbf{B}$, and the potential $\Phi(\mathbf{r})$ of the external force field satisfy the equations

$$\begin{gathered}\rho(\mathbf{V}\cdot\nabla)\mathbf{V} + \nabla p = (\nabla\times\mathbf{B})\times\mathbf{B}\frac{1}{4\pi} - \rho\nabla\Phi, \\ \nabla\cdot(\rho\mathbf{V}) = 0, \\ \mathbf{V}\cdot\nabla p + \gamma p\nabla\cdot\mathbf{V} = 0, \\ \nabla\times(\mathbf{V}\times\mathbf{B}) = 0.\end{gathered} \tag{3}$$

Here, γ is the adiabatic index. Equations (1)–(3) describe a quite general hydrodynamic system. The transition from MHD to usual hydrodynamics is performed in Eq. (2) by setting $\mathbf{B} \longrightarrow 0$. In this case, Eqs. (3) are transformed to the equations of usual hydrostatics. The incompressible fluid limit requires the additional conditions $\nabla \cdot \mathbf{V} = 0$ and $\nabla \cdot \boldsymbol{\xi} = 0$.

It can be verified that the force operator in Eq. (1) is self-adjoint; i.e.,

$$\int \boldsymbol{\eta} \cdot \mathbf{F}(\boldsymbol{\xi}) d^3 r = \int \boldsymbol{\xi} \cdot \mathbf{F}(\boldsymbol{\eta}) d^3 r, \tag{4}$$

whereas the term with $\dot{\boldsymbol{\xi}}$ in Eq. (1) is obviously antisymmetric; i.e.,

$$\int \boldsymbol{\eta} \cdot \rho(\mathbf{V} \cdot \nabla)\dot{\boldsymbol{\xi}} d^3 r = -\int \dot{\boldsymbol{\xi}} \cdot \rho(\mathbf{V} \cdot \nabla)\boldsymbol{\eta} d^3 r. \tag{5}$$

Integration in Eqs. (4) and (5) is performed over the entire space and perturbations at infinity are absent.

One can verify that dynamics (1) is conservative by multiplying Eq. (1) by $\dot{\boldsymbol{\xi}}$ and integrating over the entire space. As a result, we obtain $\dot{E} = 0$ for

$$E(t) = \int \left(\rho \frac{\dot{\boldsymbol{\xi}}^2}{2} - \frac{\boldsymbol{\xi} \cdot \mathbf{F}(\boldsymbol{\xi})}{2} \right) d^3 r. \tag{6}$$

Treating $E(t)$ as the Lyapunov functional near the steady state (equilibrium) $\boldsymbol{\xi} = 0$, $\dot{\boldsymbol{\xi}} = 0$ and minimizing over $\dot{\boldsymbol{\xi}}$, which contributes only to nonnegative kinetic energy, we arrive at the formal stability condition in the form

$$E \geq W = -\frac{1}{2} \int \boldsymbol{\xi} \cdot \mathbf{F}(\boldsymbol{\xi}) d^3 r \geq 0. \tag{7}$$

For the static MHD equilibrium (with $\mathbf{V} = 0$), condition (7) obtained in [1] is not only sufficient, which is ensured by the Lyapunov theorem, but also necessary for stability. In other words, if there is $\boldsymbol{\xi}_-$ such that $W[\boldsymbol{\xi}_-] < 0$, then a solution of Eq. (1) can be constructed near the equilibrium position $\dot{\boldsymbol{\xi}} = 0$, $\boldsymbol{\xi} = 0$ that increases in time no slower than exponentially [1]. For the case $\mathbf{V} \neq 0$, condition (7) obtained in [2] is obviously also sufficient for stability by construction. However, this condition can be practically satisfied only for the flow of the fluid directed strictly along the magnetic field, i.e., $\mathbf{V} \parallel \mathbf{B}$ [2], or in cases reduced to this case by a special transformation [3]. Indeed, by representing W in the form

$$\begin{aligned} W = \int d^3 r \Bigg\{ & \frac{1}{4\pi} [\nabla \times [\boldsymbol{\xi} \times \mathbf{B}]]^2 - \frac{1}{\rho} [\nabla \times [\boldsymbol{\xi} \times \rho \mathbf{V}]]^2 \\ & + \frac{1}{4\pi} [\boldsymbol{\xi} \times \nabla \times [\boldsymbol{\xi} \times \mathbf{B}]] \cdot \nabla \times \mathbf{B} \\ & - [\boldsymbol{\xi} \times \nabla \times [\boldsymbol{\xi} \times \rho \mathbf{V}]] \cdot \nabla \times \mathbf{V} + \mathbf{V}^2 (\nabla \cdot (\rho \boldsymbol{\xi}))^2 \\ & + \left(\boldsymbol{\xi} \cdot \nabla \frac{\mathbf{V}^2}{2} - 2\mathbf{V}(\mathbf{V} \cdot \nabla)\boldsymbol{\xi} \right) \nabla \cdot (\rho \boldsymbol{\xi}) \\ & + \boldsymbol{\xi} \cdot \nabla p \nabla \cdot \boldsymbol{\xi} + \gamma p (\nabla \cdot \boldsymbol{\xi})^2 \Bigg\}, \end{aligned} \tag{8}$$

it is easy to see that the first two terms in Eq. (8) have the same structure but opposite signs. If the steady flow of the fluid occurs at an angle to the magnetic field direction, the sum of these terms can be easily made negative by choosing a test perturbation that is nearly uniform along the magnetic field lines $\mathbf{B}$ but noticeably varies along the streamlines. This quite obvious circumstance was considered in detail in [4]. Since these terms include the highest order derivatives of $\boldsymbol{\xi}$, $W(\boldsymbol{\xi})$ does not satisfy even the Lagrange condition necessary for positive definiteness. All these statements also evidently refer to flows of a usual fluid (in the absence of the magnetic field), where the stabilizing perturbation of magnetic energy is absent.

The stability condition improved as compared to Eq. (7) can be obtained by taking into account that $\dot{\boldsymbol{\xi}}$ and $\boldsymbol{\xi}$ in Eq. (6) are not completely independent. In particular, if initial dynamics (1) has other invariants that are not reduced to energy, E can be minimized only on a class of perturbations of $\dot{\boldsymbol{\xi}}$ and $\boldsymbol{\xi}$ that do not change these invariants. Similar ideas were already proposed by Lyapunov and, in application to hydrodynamics, were formalized by Arnold [5, 6], who showed that the conservation of the vorticity integral in an ideal fluid gives rise to the foliation of the phase space of the system into symplectic sheets and a similar property is inherent in other invariants. The latter statement is very important, because, first, vorticity is not a universal invariant in hydrodynamics and, second, its conservation, as was immediately noted in [6], is insufficient for deriving a satisfactory condition of the stability of three-dimensional flows.

Among other possible invariants of the hydrodynamic equations, it is natural to first consider the momentum and angular momentum or their components, which are conserved under certain geometric or topological symmetries of the system. It is just such symmetry that makes steady flows possible. The corresponding invariant for linearized Eq. (1) can be expressed in terms of so-called neutral displacements $\boldsymbol{\xi}_N$:

$$\mathbf{F}(\boldsymbol{\xi}_N) = 0, \quad \partial_t \boldsymbol{\xi}_N = 0. \tag{9}$$

Indeed, taking the scalar product of Eq. (1) and $\boldsymbol{\xi}_N$ and integrating over the entire space with the use of definition (9), we obtain $\dot{I} = 0$, where

$$I = \int (\rho \dot{\boldsymbol{\xi}} \cdot \boldsymbol{\xi}_N + 2\rho \boldsymbol{\xi}_N (\mathbf{V} \cdot \nabla) \boldsymbol{\xi}) d^3 r.$$

In a particular geometry, the general form of the neutral displacement can even be derived analytically. For example, for the topology of toroidal nested magnetic surfaces ψ = const: $\mathbf{B} \cdot \nabla\psi = 0$, which is typical for the laboratory physics of plasma, the neutral displacement has the form

$$\boldsymbol{\xi}_N = \lambda_u(\psi)\mathbf{u} + \lambda_v(\psi)\mathbf{v}, \tag{10}$$

where $\mathbf{u} = \mathbf{B}/\rho$, $\mathbf{v} = \mathbf{D}/\rho$, and $\mathbf{D}$ is the divergence-free, frozen-in-plasma vector that is tangential (similar to $\mathbf{B}$) to the same magnetic surfaces but differs from $\mathbf{B}$:

$$\mathbf{B} \times \mathbf{D} = \rho\boldsymbol{\nabla}\psi.$$

This invariant has a nonlinear analog, the known particular case of which is the conserved cross vorticity [at $\lambda_v = 0$ in Eq. (10)].

The inclusion of this invariant really enables one to improve the energy principle given by Eq. (7). The corresponding sufficient stability condition for the system of nested magnetic surfaces was obtained by Ilgisonis and Pastukhov [7] and Hameiri [4]. However, the problem mentioned above of the sign definiteness of the energy functional is not solved for an arbitrary steady flow even under this (improved) condition. For this reason, an additional invariant should be involved in analysis.

Recently, we announced [8, 9] the concept of using a new set of invariants inherent in linearized system (1) to analyze stability. Taking the nth derivative of Eq. (1) with respect to time, we express the $(n + 2)$th derivative of $\boldsymbol{\xi}$ with respect to time in terms of lower derivatives:

$$\boldsymbol{\xi}^{(n+2)} = -2(\mathbf{V} \cdot \boldsymbol{\nabla})\boldsymbol{\xi}^{(n+1)} + \frac{1}{\rho}\mathbf{F}(\boldsymbol{\xi}^{(n)}). \tag{11}$$

Multiplying Eq. (11) by $\boldsymbol{\xi}^{(n+1)}$ and integrating over the entire space with regard for Eq. (5), we conclude, as for the case of energy, that the quantity

$$E_{n+1} = \frac{1}{2}\int\{\rho(\boldsymbol{\xi}^{(n+1)})^2 - \boldsymbol{\xi}^{(n)} \cdot \mathbf{F}(\boldsymbol{\xi}^{(n)})\}d^3r \tag{12}$$

is an exact invariant of Eq. (1) ($E_1 = E$). Using recurrence relation (11), one can evidently express all higher time derivatives in Eq. (12) in terms of $\dot{\boldsymbol{\xi}}$ and $\boldsymbol{\xi}$. In particular,

$$E_2 = \frac{1}{2}\int\left\{\frac{1}{\rho}(\mathbf{F}(\boldsymbol{\xi}) - 2\rho\mathbf{V} \cdot \boldsymbol{\nabla}\dot{\boldsymbol{\xi}})^2 - \dot{\boldsymbol{\xi}} \cdot \mathbf{F}(\dot{\boldsymbol{\xi}})\right\}d^3r. \tag{13}$$

Integrals of form (12) are generally independent for a continuous medium. For our aims, it is important that, as is seen even in Eq. (13) for E_2, the first positively definite term also includes (in contrast to E) the higher spatial derivatives of perturbation and, therefore, can compete with a similar term in the second sign-definite term.

The presence of additional invariants given by Eq. (12) allows the minimization of energy (6), which is still treated as the Lyapunov functional but only on the class of perturbations of $\dot{\boldsymbol{\xi}}$ and $\boldsymbol{\xi}$ under which one or several invariants $E_{n>1}$ are equal to zero. To this end, one may compose a new functional of the form

$$U = E + \sum_{i=1}\lambda_{i+1}E_{i+1} - I, \tag{14}$$

where λ_i is the Lagrange multiplier. As is known, unconditional extremals of U cover the desired class of conditional extremals of E. For illustration, we consider the case $\lambda_{i>2} = 0$; i.e., we take into account only one additional invariant (13) of family (12). In this case,

$$U = \int\left\{\frac{\rho\dot{\boldsymbol{\xi}}^2}{2} - \frac{\boldsymbol{\xi} \cdot \mathbf{F}(\boldsymbol{\xi})}{2}\right.$$
$$+ \frac{\lambda_2}{2\rho}(\mathbf{F}(\boldsymbol{\xi}) - 2\rho(\mathbf{V} \cdot \boldsymbol{\nabla})\dot{\boldsymbol{\xi}})^2 - \frac{\lambda_2}{2}\dot{\boldsymbol{\xi}} \cdot \mathbf{F}(\dot{\boldsymbol{\xi}}) \tag{15}$$
$$\left. + (2\rho\boldsymbol{\xi} \cdot (\mathbf{V} \cdot \boldsymbol{\nabla}) - \rho\dot{\boldsymbol{\xi}})(\lambda_u\mathbf{u} + \lambda_v\mathbf{v})\right\}d^3r.$$

First, we note that the quantities E and E_2 are equivalent and the Lagrange multiplier in Eq. (15) might be assigned to E, as well as to E_2. It is easy to verify that the consideration of only E_2 as the Lyapunov functional also enables one to obtain the condition of the positive definiteness of potential energy (7), although it can provide a more adequate stability condition, as will be seen in the example below. Since the kinetic energy in E is nonnegative, we seek the minimum of quantity (15) over $\dot{\boldsymbol{\xi}}$ (in this case, the condition $\delta^2U/\delta\dot{\boldsymbol{\xi}}^2 > 0$ must be obviously satisfied, which should be verified after the choice of the set of λ). The Euler equation for the minimizing perturbation of $\dot{\boldsymbol{\xi}}$ yields

$$\dot{\boldsymbol{\xi}} = \underbrace{\lambda_u\mathbf{u} + \lambda_v\mathbf{v}}_{\boldsymbol{\xi}_N} + \lambda_2\frac{\mathbf{F}(\dot{\boldsymbol{\xi}})}{\rho}$$
$$+ 2\lambda_2\mathbf{V} \cdot \boldsymbol{\nabla}\left(2(\mathbf{V} \cdot \boldsymbol{\nabla})\dot{\boldsymbol{\xi}} - \frac{\mathbf{F}(\boldsymbol{\xi})}{\rho}\right). \tag{16}$$

Let us reveal the formal succession with known conditions. Formally setting $\lambda_{u,v,2} = 0$ in Eq. (15) and minimizing over $\dot{\boldsymbol{\xi}}$, we arrive at Frieman–Rotenberg condition (7). Retaining in (16) $\lambda_{u,v}$ at $\lambda_2 \longrightarrow 0$, we arrive at the Il'gisonis–Pastukhov–Hameiri condition [7, 4]

$$\dot{\boldsymbol{\xi}} \longrightarrow \boldsymbol{\xi}_N, \quad U \longrightarrow U_{IPH} = \int d^3r\left(\frac{\rho\boldsymbol{\xi}_N^2}{2} - \frac{\boldsymbol{\xi} \cdot \mathbf{F}(\boldsymbol{\xi})}{2}\right),$$

where $\boldsymbol{\xi}_N$ ensures the condition

$$\int(\rho\boldsymbol{\xi}_N^2 - 2\rho\boldsymbol{\xi} \cdot (\mathbf{V} \cdot \boldsymbol{\nabla})\boldsymbol{\xi}_N)d^3r = 0.$$

As was mentioned above, although the condition $U_{IPH} \geq 0$ is softer than Frieman–Rotenberg condition (7) ($U_{IPH} \geq U_{FR} = -\int \boldsymbol{\xi} \cdot \mathbf{F}(\boldsymbol{\xi})\, d^3r/2$), it is still unsatisfactory for an arbitrary flow with $\mathbf{V}$ unparallel to $\mathbf{B}$. However, the invariants $E_{n \geq 2}$ are disregarded in this limit. Let us try to improve this condition assuming that λ_2 is small but nonzero. In the first order in λ_2, Eq. (16) makes it possible to determine the minimizing $\boldsymbol{\xi}$ function in the explicit form

$$\dot{\boldsymbol{\xi}} \approx \boldsymbol{\xi}_N - 2\lambda_2(\mathbf{V} \cdot \nabla)\ddot{\boldsymbol{\xi}}_0, \qquad (17)$$

where

$$\ddot{\boldsymbol{\xi}}_0 = \mathbf{F}(\boldsymbol{\xi})/\rho - 2(\mathbf{V} \cdot \nabla)\boldsymbol{\xi}_N.$$

In this case, the desired stability condition is written for arbitrary $\boldsymbol{\xi}$ in the form

$$U \geq U_{\min}$$
$$= \int \left\{ \frac{\rho}{2}(\boldsymbol{\xi}_N - 2\lambda_2(\mathbf{V} \cdot \nabla)\ddot{\boldsymbol{\xi}}_0)^2 - \frac{1}{2}\boldsymbol{\xi} \cdot \mathbf{F}(\boldsymbol{\xi}) \right\} d^3r \geq 0. \qquad (18)$$

For definiteness, considering a system with nested magnetic surfaces, for which $\boldsymbol{\xi}_N$ is specified by Eq. (10), we determine the Lagrange multipliers in Eq. (18) by substituting Eq. (17) into the conditions

$$E_2,\ I(\dot{\boldsymbol{\xi}}, \boldsymbol{\xi}) \approx 0.$$

As a result, we obtain

$$\lambda_2 = \frac{1}{8}\frac{\int \rho \ddot{\boldsymbol{\xi}}_0^2 d^3r}{\int \rho((\mathbf{V} \cdot \nabla)\ddot{\boldsymbol{\xi}}_0)^2 d^3r},$$

$$\lambda_u = \frac{A_v D_u - A_0 D_v}{A_u A_v - A_0^2}, \quad \lambda_v = \frac{A_u D_v - A_0 D_u}{A_u A_v - A_0^2}.$$

Here,

$$A_{w = u, v} = \langle 4\lambda_2 \rho((\mathbf{V} \cdot \nabla)\mathbf{w})^2 - \rho \mathbf{w}^2 \rangle,$$

$$A_0 = \langle 4\lambda_2 \rho((\mathbf{V} \cdot \nabla)\mathbf{u}) \cdot ((\mathbf{V} \cdot \nabla)\mathbf{V}) - \rho \mathbf{u} \cdot \mathbf{V} \rangle,$$

$$D_{w = u, v} = \langle 2(\lambda_2 \mathbf{F}(\boldsymbol{\xi}) - \rho \boldsymbol{\xi}) \cdot (\mathbf{V} \cdot \nabla)\mathbf{w} \rangle,$$

where the angular brackets mean the averaging over the magnetic surface.

Another combination of the invariants E_n can obviously be used to analyze stability. For illustration, let us consider the axisymmetric equilibrium of a cold ($p = 0$), constant-density plasma rotating about the attractive center in the absence of the magnetic field. In the cylindrical coordinate system (r, φ, z) $\mathbf{V} = r\Omega\mathbf{e}_\varphi$, where Ω is the angular velocity of the equilibrium rotation, which is related to the potential gradient as $\Omega^2 = \partial\Phi/r\partial r$. The symmetry of the problem allows the solution to be sought in the form of a Fourier series in the symmetry direction:

$$\boldsymbol{\xi} = \sum_m \boldsymbol{\xi}_m,$$

where

$$\boldsymbol{\xi}_m = [\xi_r(t, r, z)\mathbf{e}_r + \xi_\varphi(t, r, z)\mathbf{e}_\varphi + \xi_z(t, r, z)\mathbf{e}_z]e^{im\varphi}.$$

Equation (1) is represented in the simple form

$$\ddot{\boldsymbol{\xi}} + 2\Omega\hat{A}\dot{\boldsymbol{\xi}} - \hat{B}\boldsymbol{\xi} = 0, \qquad (19)$$

where

$$\hat{A} = \begin{pmatrix} im & -1 & 0 \\ 1 & im & 0 \\ 0 & 0 & im \end{pmatrix},$$
$$\hat{B} = \begin{pmatrix} \Omega^2 m^2 - r(\Omega^2)'_r & 2im\Omega^2 & 0 \\ -2im\Omega^2 & \Omega^2 m^2 & 0 \\ 0 & 0 & \Omega^2 m^2 \end{pmatrix}. \qquad (20)$$

The stability of the solution of Eq. (19) is easily verified by the spectral method. For $\boldsymbol{\xi}_m \sim \exp(i\omega t)$, we arrive at the dispersion relation

$$(\omega + m\Omega)^4[(\omega + m\Omega)^2 - 4\Omega^2 - r(\Omega^2)'_r] = 0,$$

from which it follows that a necessary and sufficient condition for spectral stability has the form

$$\kappa^2 \equiv 4\Omega^2 + r(\Omega^2)'_r \geq 0. \qquad (21)$$

The quantity κ is sometimes called *epicyclic* frequency.

Let us apply our variational approach to this system. In this case, the multipliers λ may be functions of r and z, because E and E_2 are invariants even when the integrals in Eqs. (6) and (13) are calculated along the flow tube at fixed r and z values. The above procedure for minimizing the composite functional U can be completely realized for Eq. (19) and provides condition (21). However, tedious algebra is required even in this case. The problem can be significantly simplified by the substitution

$$\boldsymbol{\xi} \longrightarrow \boldsymbol{\xi}(t, r, z)e^{-im\Omega t},$$

which is equivalent to the transition to the reference frame rotating at a given radius about the z axis with the frequency Ω. The equation for the new function $\boldsymbol{\xi}$ retains form (19), but the corresponding matrices have the much simpler form

$$\hat{A} \longrightarrow \begin{pmatrix} 0 & -1 & 0 \\ 1 & 0 & 0 \\ 0 & 0 & 0 \end{pmatrix}, \quad \hat{B} \longrightarrow \begin{pmatrix} -r(\Omega^2)'_r & 0 & 0 \\ 0 & 0 & 0 \\ 0 & 0 & 0 \end{pmatrix}. \qquad (22)$$

The quantity E_2, calculated as

$$E_2 = \frac{1}{2}(2\Omega\hat{A}\dot{\boldsymbol{\xi}} - \hat{B}\boldsymbol{\xi})^2 - \frac{1}{2}\dot{\boldsymbol{\xi}}\hat{B}\dot{\boldsymbol{\xi}},$$

is reduced in the case of Eq. (22) to

$$E_2 = \frac{1}{2}\kappa^2\dot{\xi}_r^2 + \frac{1}{2}(2\Omega\dot{\xi}_\varphi - r(\Omega^2)'_r\xi_r)^2.$$

It is seen that, considering E_2 as the Lyapunov functions [$\lambda_2 \longrightarrow \infty$ in Eq. (14)] and taking into account the positivity of the last term, we arrive at desired condition (21). Thus, this example demonstrates the fruitfulness of the use of invariant (12) when constructing the Lyapunov functional.

This work was supported by the Human Capital Foundation (project no. 41).

REFERENCES

1. I. B. Bernstein *et al.*, Proc. R. Soc. London, Ser. A **244**, 17 (1958).
2. E. Frieman and M. Rotenberg, Rev. Mod. Phys. **32**, 898 (1960).
3. K. I. Ilin and V. A. Vladimirov, Phys. Plasmas **11**, 3586 (2004).
4. E. Hameiri, Phys. Plasmas **5**, 3270 (1998).
5. V. I. Arnold, Dokl. Akad. Nauk SSSR **162**, 975 (1965).
6. V. I. Arnold, Am. Math. Soc. Trans. **19**, 267 (1969).
7. V. I. Ilgisonis and V. P. Pastukhov, Fiz. Plazmy **22**, 228 (1996) [Plasma Phys. Rep. **22**, 208 (1996)].
8. V. I. Ilgisonis, Proc. HSCoPP-2004, http://www.cpt.univ-mrs.fr/hscopp04/Abstracts/ABS_Ilgisonis.txt.
9. V. I. Ilgisonis, physics/0506073.

Translated by R. Tyapaev

JETP Letters, Vol. 82, No. 9, 2005, pp. 575–579. Translated from Pis'ma v Zhurnal Éksperimental'noĭ i Teoreticheskoĭ Fiziki, Vol. 82, No. 9, 2005, pp. 652–656.
Original Russian Text Copyright © 2005 by Kopaev, Sofronov.

Manifestation of the Superconducting Pairing of Repulsive Particles with a Large Total Momentum in Andreev Reflection

Yu. V. Kopaev[a] and V. M. Sofronov[b]
[a] *Lebedev Physical Institute, Russian Academy of Sciences, Leninskiĭ pr. 53, Moscow, 119991 Russia*
e-mail: kopaev@sci.lebedev.ru
[b] *Moscow State Institute of Electronic Engineering (Technical University),*
Zelenograd, Moscow region, 124498 Russia

Received September 15, 2005

Features of Andreev reflection at the normal metal–superconductor interface in the presence of repulsive-interaction-induced pairing with a large total momentum **K** have been analyzed. When the direction of the motion of a hole arising upon the formation of a pair with $\mathbf{K} \neq 0$ by an incident electron corresponds to transmission, the intensity of Andreev reflection decreases compared to the case $\mathbf{K} = 0$. Another cause of the decrease in the intensity is that, owing to the repulsive interaction, the superconducting order parameter has a zero line, and the quasiparticle energy minimum, which determines the turning point, does not coincide with the Fermi contour on which the quasiparticle charge changes its sign (charge asymmetry). © *2005 Pleiades Publishing, Inc.*

PACS numbers: 74.20.–z, 74.25.–q

The determination of the symmetry of the order parameter of high-temperature superconducting (HTSC) cuprates is of great significance for understanding high-temperature superconductivity. Measurement of Andreev reflection spectra is one of the main methods that enable one to detect the superconducting gap and determine its symmetry type. In ordinary superconductors, owing to Andreev reflection, the conductivity of the normal metal–superconductor (NS) junction for voltages lower than the gap width is twice as high as the value for a superconductor in the normal state. It is found that the increase in the conductivity in HTSC cuprates may be less than twofold [1]. This experimental observation is as yet unexplained. In this work, we analyze Andreev reflection at the NS interface in the model of superconducting pairing with a large total momentum and the repulsive interaction (**K**-pairing) [2]. As will be shown below, the nonzero total momentum of a pair gives rise to a significant decrease in the differential conductivity for voltages at which Andreev reflection is manifested.

As was shown in [3, 4], singlet superconducting pairing with a large total momentum in the presence of the repulsive interaction is possible even at an arbitrarily small coupling constant under the mirror nesting condition. This condition is satisfied for a particular type of the electron (hole) dispersion relation, when the sections of the Fermi contour (analog of the Fermi surface in a quasi-two-dimensional system) coincide with an energy contour of the relative motion of a pair with a given total momentum **K**. The mirror nesting condition can be written as

$$\varepsilon(\mathbf{K}/2-\mathbf{k}) = \varepsilon(\mathbf{K}/2+\mathbf{k}), \qquad (1)$$

where $\varepsilon(\mathbf{K}/2 \pm \mathbf{k})$ is the dispersion relation for the particles forming the pair and **k** is the relative momentum of the pair.

Let us list several examples of the satisfaction of the mirror nesting condition [4]. Condition (1) is satisfied if the Fermi contour consists of four pockets centered at the points belonging to symmetric directions. Such hole pockets are observed in underdoped cuprates due to the presence of a dielectric gap in the electron spectrum [5]. Although hole cuprates are basic objects of experimental investigations, we analyze the problem of Andreev reflection in terms of incident electrons and reflected holes. Thus, we suppose that excitations outside and inside the Fermi contour are quasielectrons and quasiholes, respectively.

Certain kinematic constraints are imposed on momentum-space regions available for pairing. According to these constraints, both particles forming a pair must be either inside or outside the Fermi contour. It is evident that there are four equivalent kinematically allowed regions Ξ_K each determined by the total pair momentum **K** that has the same length for all regions.

The symmetry of the order parameter is determined by the interaction mixing the states of pairs belonging to equivalent regions Ξ_K. The order parameter can have either the same or opposite signs before and after the

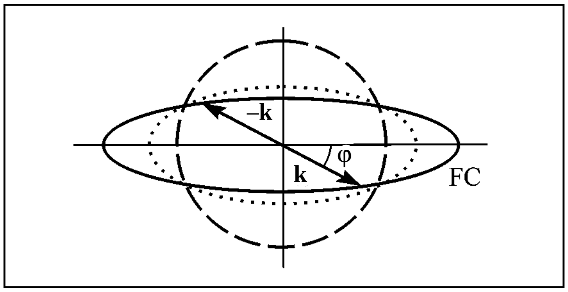

Fig. 1. One of the pockets of the Fermi contour FC. The dashed line is the line of the zeros of the order parameter and the dotted line is the line of the minima of the energy of quasiparticle excitations. The polar angle φ is introduced.

rotation by $\pi/2$ about the center of the 2D Brillouin zone (*s*- and *d*-type symmetries, respectively). When the equivalent regions Ξ_K do not overlap, each allowable region can be treated separately.

For the singlet superconducting pairing of repulsive particles with a large total momentum, the order parameter $\Delta_K(\mathbf{k})$ inside the region Ξ_K changes sign when transversing the zero line that intersects the Fermi contour [4]:

$$\Delta_K(k) = \Delta_{0K}(1 - k^2/k_0^2), \tag{2}$$

where Δ_{0K} determines the energy scale of the superconducting gap and k_0 is the radius of the zero line. Owing to the dependence of superconducting gap (2) on the relative momentum, the minimum of the energy

$$E_{Kk} = \sqrt{\xi_{Kk}^2 + \Delta_{Kk}^2} \tag{3}$$

of quasiparticle excitations does not coincide with the Fermi contour. Here, ξ_{Kk} is the kinetic energy of a pair measured from the chemical potential (Fig. 1).

Let us determine the total current through the interface between the normal metal N and superconductor S with the same dispersion relation for electrons in both regions. Let particles in the normal region move in the ballistic regime. In addition, we assume that particles incident at the NS interface from the region N are distributed according to the equilibrium Fermi–Dirac distribution function $f_0(E - eV)$ with the energy shift due to the applied voltage [6]. The energy of particles is measured from the chemical potential of the superconductor.

In the absence of a barrier at the interface, a particle incident from the normal region can either undergo Andreev reflection with probability A or penetrate deep into the superconducting region with probability B. Therefore,

$$A + B = 1.$$

Thus, the current through the NS interface from the normal side of the junction can be represented in the form

$$I_{\mathrm{NS}} = \sum_{\mathbf{K}} \left(I_K + \frac{1}{eR_{\mathrm{N}}} \int_{-\infty}^{\infty} T_K(E)[f_0(E - eV) - f_0(E)]dE \right). \tag{4}$$

Here, the summation is performed over vectors $\mathbf{K}$ with zero or positive projections onto the normal to the interface. The resistance is given by the expression

$$R_{\mathrm{N}} = (2N(0)e^2 v_{KkF}\Omega)^{-1},$$

where $N(0)$ is the density of states at the Fermi contour, Ω is the junction area, and $v_{KkF} = \nabla_k \xi_{Kk}|_{k = k_F}$ is the Fermi velocity. The effective transmission coefficient is expressed as [7]

$$T_K(E) = \int_0^{\pi/2} d\varphi \frac{\cos\varphi}{2\pi}[1 + A_K(E, \varphi)], \tag{5}$$

where the polar angle φ is measured from the normal to the interface (the CuO_2 plane is perpendicular to the interface). The component I_K of the total current corresponds to the fact that each particle in the region Ξ_K has mean momentum $\mathbf{K}/2$:

$$I_K \propto \mathbf{v}_K \cdot \mathbf{n}\Omega V, \tag{6}$$

where $\mathbf{v}_K$ is the velocity of the center of mass of the region Ξ_K and $\mathbf{n}$ is the normal to the interface.

Let us consider the case where the interface is oriented so that the normal to the surface corresponds to the direction of total vector $\mathbf{K}'$, which is one of total vectors $\mathbf{K}$ (Fig. 2). In contrast to the case of zero total momentum of the pair, when pairing occurs with nonzero total momentum, the direction of the motion of a hole undergoing Andreev reflection is not exactly opposite to the direction of the incidence of an electron at the interface. In this case, the angle of Andreev reflection is determined by the total momentum of the pair. When a particle is incident at the interface with momentum $\mathbf{k}'_+$, it forms a pair with a particle with momentum $\mathbf{k}'_-$ in the region $\Xi_{K'}$. As a result, the direction of the motion of an arising quasihole corresponds to transmission ($\mathbf{k}'_- \cdot \mathbf{n} > 0$). We call this geometric Andreev transmission. Thus, the probability of Andreev reflection for the region $\Xi_{K'}$ is equal to zero over the entire energy range:

$$A_{K'} = 0. \tag{7}$$

Current transferred by a $\mathbf{K}$ pair formed in geometric Andreev transmission is partially compensated by the current of a simultaneously arising quasihole. Therefore, in contrast to the case $\mathbf{K} = 0$, the right pocket (Fig. 2) does not contribute to the total probability of

Andreev reflection. An electron incident at the interface with momentum $\mathbf{k}_+$ (Fig. 2, upper pocket) forms a pair with an electron with momentum $\mathbf{k}_-$. In this case, the direction of the motion of the arising quasihole corresponds to reflection ($\mathbf{k}_- \cdot \mathbf{n} < 0$).

For the indicated orientation of the interface, the expression for the total current can be simplified. As follows from Eqs. (4)–(7),

$$I_{\mathrm{NS}} = I_{\mathrm{NN}}^{K'} + \frac{2}{eR_{\mathrm{N}}}\int_{-\infty}^{\infty} T_K(E)[f_0(E-eV) - f_0(E)]dE. \quad (8)$$

Here, $I_{\mathrm{NN}}^{K'}$ is the contribution of the right pocket to the total current through the interface.

In order to determine the probability of Andreev reflection for the upper and lower pockets, we consider the Bogoliubov equations

$$\begin{pmatrix} \hat{\varepsilon} - \mu & \Delta(\mathbf{r}) \\ \Delta^*(\mathbf{r}) & -(\hat{\varepsilon} - \mu) \end{pmatrix} \Psi_{\mathrm{S}}(\mathbf{r}) = E\Psi_{\mathrm{S}}(\mathbf{r}), \quad (9)$$

where $\hat{\varepsilon}$ is the kinetic energy operator and μ is the chemical potential. The solution of system (9) for particles outside and inside the Fermi contour is represented in the form

$$\Psi_{\mathrm{S}}^{+} = \begin{pmatrix} u_{Kk} e^{i(\mathbf{k} + \mathbf{K}/2)\cdot \mathbf{r}} \\ v_{Kk} e^{i(\mathbf{k} - \mathbf{K}/2)\cdot \mathbf{r}} \end{pmatrix},$$

$$\Psi_{\mathrm{S}}^{-} = \begin{pmatrix} v_{Kk} e^{i(\mathbf{k} + \mathbf{K}/2)\cdot \mathbf{r}} \\ u_{Kk} e^{i(\mathbf{k} - \mathbf{K}/2)\cdot \mathbf{r}} \end{pmatrix},$$

where

$$u_{Kk}^2 = \frac{1}{2}\left(1 + \frac{\xi_{Kk}}{E_{Kk}}\right), \quad v_{Kk}^2 = \frac{1}{2}\left(1 - \frac{\xi_{Kk}}{E_{Kk}}\right).$$

At the interface between the normal metal and superconductor, the following boundary conditions must be satisfied:

$$\Psi_{\mathrm{S}} = \Psi_{\mathrm{N}}, \quad \mathbf{n}\cdot\nabla\Psi_{\mathrm{S}} = \mathbf{n}\cdot\nabla\Psi_{\mathrm{N}}. \quad (10)$$

The function Ψ_{N} is obtained from the function Ψ_{S} by substituting $\Delta_{Kk} \equiv 0$. Thus, similar to [6],

$$\Psi_{\mathrm{inc}} = \begin{pmatrix} 1 \\ 0 \end{pmatrix} e^{i\mathbf{k}_+ \cdot \mathbf{r}}, \quad (11)$$

$$\Psi_{\mathrm{ref}} = a\begin{pmatrix} 0 \\ 1 \end{pmatrix} e^{-i\mathbf{k}_- \cdot \mathbf{r}} \quad (12)$$

for the incident and reflected particles, respectively. Here, $\mathbf{k}_+ = \mathbf{K}/2 + \mathbf{k}$ and $\mathbf{k}_- = \mathbf{K}/2 - \mathbf{k}$ are the momenta of the incident and reflected particles, respectively, and a^2 is equal to the Andreev reflection probability A.

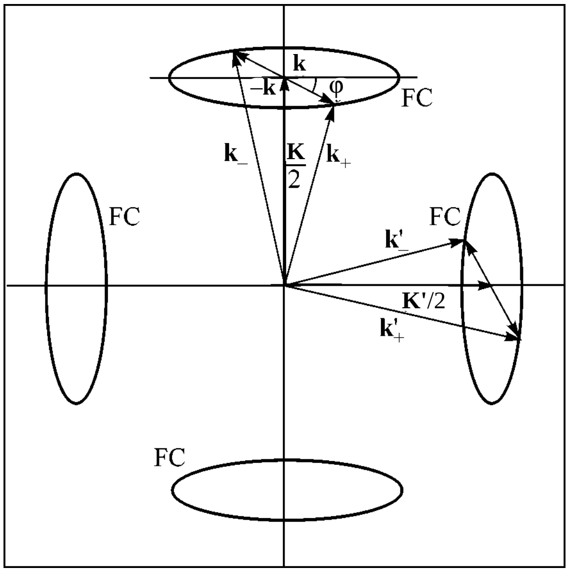

Fig. 2. Formation of a pair with a large total momentum. The direction of the total vector $\mathbf{K}'$ corresponds to the normal to the interface. A particle incident at the interface with momentum $\mathbf{k}_+$ undergoes Andreev reflection with momentum $\mathbf{k}_-$, whereas a particle with momentum $\mathbf{k}'_+$ is transmitted to the superconductor as a quasihole with momentum $\mathbf{k}'_-$ (geometric Andreev transmission).

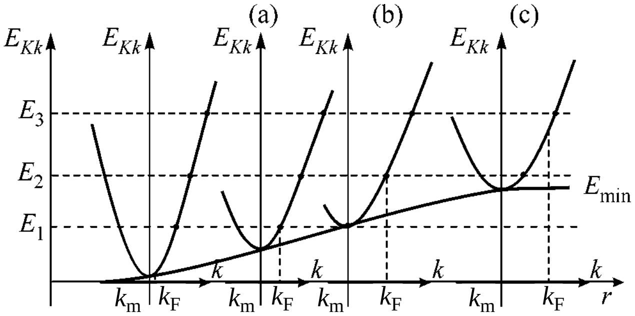

Fig. 3. Process of the transition of the incident electron from the normal region to the superconductor: E_1 is the Andreev reflection, E_2 is the Andreev transmission due to charge asymmetry, and E_3 is the usual transmission.

The superconducting gap amplitude Δ_{0K} is equal to zero deep in the normal region and is maximal deep in the superconductor. The transition from one value to the other occurs at a finite distance equal to the coherence length. Figure 3 shows the process of the transition of the electron from the normal region to the super-

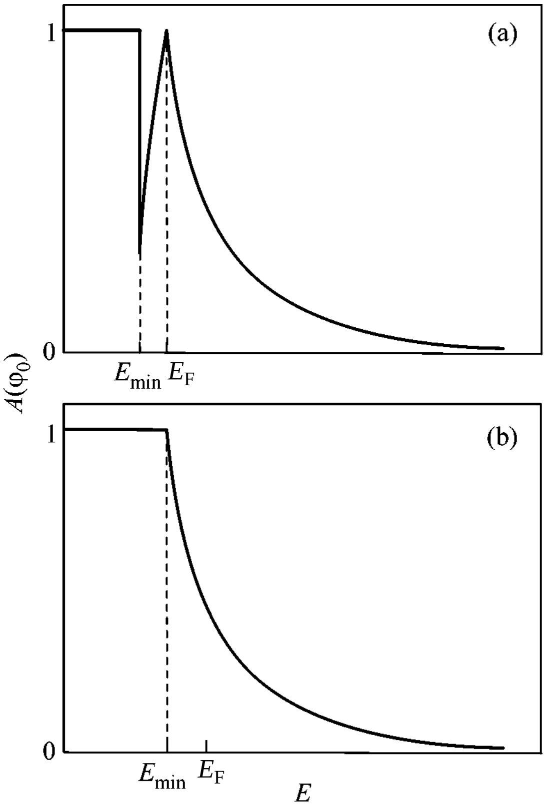

Fig. 4. Andreev-reflection probability A vs. the quasiparticle energy E at fixed polar angles: (a) φ_0 ($k_{\rm m} < k_{\rm F}$), in the energy range $E_{\rm min}(\varphi_0, x \longrightarrow \infty) < E < E_{\rm F}(\varphi_0, x \longrightarrow \infty)$, Andreev reflection is suppressed by Andreev transmission due to charge asymmetry and (b) φ_1 ($k_{\rm m} > k_{\rm F}$), the energy range corresponding to Andreev transmission due to charge asymmetry is absent.

conducting region at a certain polar angle $\varphi = \varphi_0$. For the chosen direction, the momentum $k_{\rm m}$ corresponding to the minimum of the energy of quasiparticle excitation (3) is lower than $k_{\rm F}$.

A particle incident at the interface with energy $E = E_1$ [$E_1 < E_{\rm min}(\varphi_0, x \longrightarrow \infty)$], moving deeply into the superconductor, first reaches a point where its momentum is equal to $k_{\rm F}$ (Fig. 3a). Here, the quasiparticle charge changes its sign. Then, the particle reaches the energy minimum point E_{Kk} (Fig. 3b). At this point, the relative velocity $\nabla_k E_{Kk}$ is inverted, Andreev reflection occurs, and a hole is reflected to the N region.

A particle with energy $E = E_2$ ($E_{\rm min}(\varphi_0, x \longrightarrow \infty) < E_2 < E_{\rm F}(\varphi_0, x \longrightarrow \infty)$), moving into the S region, intersects the Fermi contour, passing to the hole branch of the spectrum (Fig. 3b). However, it does not reach the point determining the turn of the group velocity. Thus, the arising quasihole moves deeply into the superconductor. The Andreev transmission process, i.e., the transmission of an incident electron to the superconductor as a quasihole, is possible in the case $\mathbf{K} = 0$ only in the presence of the interface barrier [6]. Since this process occurs due to the barrier at the NS interface, we call it barrier Andreev transmission, in contrast to the above-discussed Andreev transmission due to the noncoincidence of the quasiparticle energy minimum with the Fermi contour (Andreev transmission due to charge asymmetry).

At energy $E = E_3$ [$E_3 > E_{\rm F}(\varphi_0, x \longrightarrow \infty)$], an incident particle reaches neither the point $k_{\rm F}$ nor the point $k_{\rm m}$. Correspondingly, usual transmission of the quasiparticle into the superconductor occurs (Fig. 3c).

Thus, for the transmitted particle,

$$\Psi_{\rm trans} = b\Psi_{\rm S}^{-}$$

in the energy range $E_{\rm min}(\varphi, x \longrightarrow \infty) < E < E_{\rm F}(\varphi, x \longrightarrow \infty)$ and

$$\Psi_{\rm trans} = b\Psi_{\rm S}^{+}$$

for energies $E > E_{\rm F}(\varphi, x \longrightarrow \infty)$. The coefficient b squared is equal to the probability B of the transmission of particles to the superconducting region.

Using boundary conditions (10), we obtain

$$A(E,\varphi) = \begin{cases} 1, \quad E < E_{\rm min}(\varphi, x \longrightarrow \infty), \\ \dfrac{u^2}{v^2}, \\ E_{\rm min}(\varphi, x \longrightarrow \infty) < E < E_{\rm F}(\varphi, x \longrightarrow \infty), \\ \dfrac{v^2}{u^2}, \quad E > E_{\rm F}(\varphi, x \longrightarrow \infty). \end{cases} \tag{13}$$

Figure 4a shows the plot of the function $A(E, \varphi)$ for $\varphi = \varphi_0$ ($k_{\rm m} < k_{\rm F}$). For energies $E < E_{\rm min}(\varphi_0, x \longrightarrow \infty)$, the probability of Andreev reflection is equal to unity. In the energy range $E_{\rm min}(\varphi_0, x \longrightarrow \infty) < E < E_{\rm F}(\varphi_0, x \longrightarrow \infty)$, Andreev reflection decreases, because Andreev transmission due to charge asymmetry appears. On the Fermi contour, the probability A is equal to unity. For high energies $E > E_{\rm F}(\varphi_0, x \longrightarrow \infty)$, Andreev reflection is suppressed by the usual transmission of particles to the superconductor.

In the other case, $k_{\rm m} > k_{\rm F}$ ($\varphi = \varphi_1$), the Andreev transmission region due to charge asymmetry is absent (Fig. 4b), because the electron moving deeply into the superconductor reaches the point determining the inversion of the relative velocity earlier than the point where the quasiparticle charge changes sign.

The ratio $g \equiv G_{\rm NS}/G_{\rm NN}$ of the conductivities of the NS junction, when the superconductor is in the superconducting and normal states, decreases due to the indicated processes of geometric Andreev transmission and charge-asymmetry-induced Andreev transmission. At $V = 0$, a decrease in g compared to the case $\mathbf{K} = 0$ is caused only by geometric Andreev transmission. As follows from Eq. (8), at $T = 0$,

$$g(0) = 1 + 2G^K_{\mathrm{NN}}/G_{\mathrm{NN}},$$

where $2G^K_{\mathrm{NN}}$ is the contribution of the upper pocket and equivalent lower pocket to the total conductivity G_{NN} of the junction,

$$G^K_{\mathrm{NN}}/G^K_{\mathrm{NS}} = (T_K)^{-1}.$$

Here, G^K_{NS} is the contribution of the upper pocket to the total conductivity G_{NS}. By definition, $2G^K_{\mathrm{NN}}/G_{\mathrm{NN}} < 1$ and, correspondingly, $G_{\mathrm{NS}}/G_{\mathrm{NN}} < 2$. At $V > 0$, Andreev transmission due to charge asymmetry begins to contribute. The decrease in g with increasing applied stress is faster than that for the case $\mathbf{K} = 0$.

Thus, Andreev reflection in the presence of pairing with large total momentum $\mathbf{K}$ has a number of features. Namely, the intensity of Andreev reflection is lower than that in the case $\mathbf{K} = 0$ when the direction of the motion of a hole arising upon the formation of a pair with $\mathbf{K} \neq 0$ by an incident electron corresponds to transmission (geometric Andreev transmission). Another cause of the decrease in the intensity is Andreev transmission due to charge asymmetry. This type of transmission appears because, owing to the repulsive interaction, the superconducting order parameter has a zero line, and the quasiparticle energy minimum, which determines the turning point, does not coincide with the Fermi contour on which the quasiparticle charge changes its sign.

This work was supported in part by the Russian Foundation for Basic Research.

REFERENCES

1. Guy Deutscher, Rev. Mod. Phys. **77**, 109 (2005).
2. V. I. Belyavskiĭ, V. V. Kapaev, and Yu. V. Kopaev, Zh. Éksp. Teor. Fiz. **118**, 941 (2000) [JETP **91**, 817 (2000)].
3. V. I. Belyavskiĭ, Yu. V. Kopaev, Yu. N. Togushova, and S. V. Shevtsov, Zh. Éksp. Teor. Fiz. **126**, 672 (2004) [JETP **99**, 585 (2004)].
4. V. I. Belyavskiĭ, Yu. V. Kopaev, V. M. Sofronov, and S. V. Shevtsov, Zh. Éksp. Teor. Fiz. **124**, 1149 (2003) [JETP **97**, 1032 (2003)].
5. V. I. Belyavskiĭ, V. V. Kapaev, and Yu. V. Kopaev, Pis'ma Zh. Éksp. Teor. Fiz. **81**, 650 (2005) [JETP Lett. **81**, 527 (2005)].
6. G. E. Blonder, M. Tinkham, and T. M. Klapwijk, Phys. Rev. B **25**, 4515 (1982).
7. N. A. Mortensen, K. Flensberg, and A.-P. Jauho, Phys. Rev. B **59**, 10176 (1999).

Translated by R. Tyapaev

JETP Letters, Vol. 82, No. 9, 2005, pp. 580–585. Translated from Pis'ma v Zhurnal Éksperimental'noĭ i Teoreticheskoĭ Fiziki, Vol. 82, No. 9, 2005, pp. 657–663.
Original Russian Text Copyright © 2005 by Mitsen, Ivanenko.

Origin of Incommensurate Spin Modulation in $La_{2-x}Sr_xCuO_4$

K. V. Mitsen and O. M. Ivanenko
Lebedev Physical Institute, Russian Academy of Sciences, Moscow, 119991 Russia
e-mail: mitsen@sci.lebedev.ru

Received September 15, 2005

A model for explaining incommensurate spin modulation observed in $La_{2-x}Sr_xCuO_4$ is proposed without assuming stripe formation. In this model, all features of the observed spin textures in the entire doping range are associated only with the geometrical relations for the square lattice and with the competition between various forms of ordering of Sr ions. © *2005 Pleiades Publishing, Inc.*

PACS numbers: 74.20.Mn, 75.10.–b, 75.25.+z

The concept of stripes, which implies the existence of the incommensurate modulation of the spin antiferromagnetic (AFM) structure in the form of antiphase domains of AFM-ordered spins separated by narrow extended stripes of doped holes, has been used in a large number of recent publications devoted to analysis of *p*-doped cuprate high-temperature superconductors (HTSCs) [1–13]. In experiments on magnetic neutron scattering, such a modulation, which is characterized by wavevector **Q**, must be observed in the form of two incommensurate peaks shifted relative to the AFM wavevector $\mathbf{Q}_{\mathrm{AF}}(1/2; 1/2, 0)$ by $\varepsilon = 1/T$ in the direction of the modulation vector. Here, T is the magnetic structure period in units of the lattice constant. Accordingly, the period of charge modulation should be equal to $T/2$ and the corresponding incommensurate charge density modulation should be equal to 2ε.

The results of neutron diffraction studies of the magnetic texture of $La_{2-x}Sr_xCuO_4$ and $La_{1.6-x-y}Nd_{0.4}Sr_xCuO_4$ [1, 14–18] can be summarized in the form of the phase diagram (Fig. 1a). As is seen in Fig. 1a, incommensurate elastic-scattering peaks associated with static modulation (shaded in the figure) are observed for Sr concentrations $x < 0.07$ and $0.11 < x < 0.12$. In the concentration ranges $0.07 < x < 0.11$ and $x > 0.13$, incommensurate peaks observed in inelastic neutron scattering indicate the existence of the dynamic modulation of the spin texture. For $x < 0.07$, "diagonal" stripes exist with a single modulation vector directed along the orthorhombic *b* axis, while modulation for "parallel" stripes ($x > 0.055$) always exists in two directions parallel to the tetragonal axes. In the intermediate range ($0.055 < x < 0.07$), both types of modulation are observed. To compare the spin structures in the cases of diagonal and parallel stripes, both types of structures are considered in tetragonal coordinates. In this case, the spin modulation incommensurability parameter δ is equal to ε and $\delta = \varepsilon/\sqrt{2}$ for parallel and diagonal stripes, respectively, and a surprisingly simple relation ($\delta \approx x$) is observed between the incommensurability parameter and concentration in experiments for $x < 0.12$.

The appearance of the stripe structure due to competition between the electronic phase separation and long-range Coulomb repulsion was analyzed theoretically in [2–9]. An alternative mechanism of the formation of the

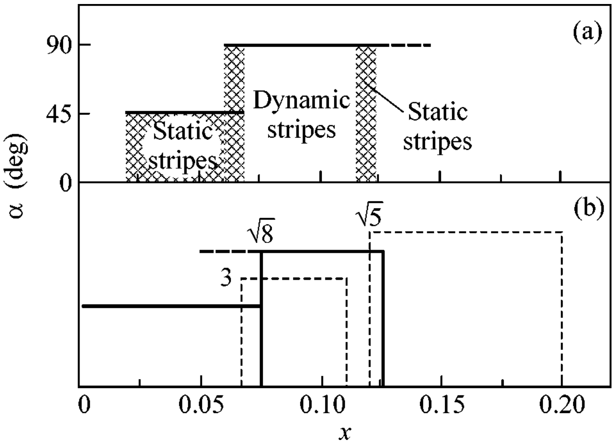

Fig. 1. (a) Experimental magnetic phase diagram of $La_{2-x}Sr_xCuO_4$ [1, 14–18]. Angles $\alpha = 45°$ and $90°$ correspond to diagonal and vertical stripes, respectively. Shaded regions correspond to the ranges of observation of static stripes. (b) Calculated stripe phase diagram of $La_{2-x}Sr_xCuO_4$. Dashed lines bound the regions of percolation via the chains of negative U centers with $l_{\mathrm{com}} = 3a$ and $a\sqrt{5}$ (dynamic stripes); thick solid lines bound the regions of existence of microdomains with $l_{\mathrm{com}} = \sqrt{8}$ ($0.075 < x < 0.125$) and diagonal rows of doped holes ($x < 0.075$). The thick dashed line corresponds to the region in which microdomains with $l_{\mathrm{com}} = \sqrt{8}$ can exist due to fluctuations of the Sr concentration in small regions. The figures at the corners of the rectangles are the values of l_{com} for a given type of microdomain.

0021-3640/05/8209-0580$26.00 © 2005 Pleiades Publishing, Inc.

dielectric stripe phase in a weakly doped HTSC material due to nesting of the Fermi surface was proposed in [10–13]. However, both theories face considerable difficulties when describing spin textures observed in $\mathrm{La}_{2-x}\mathrm{Sr}_x\mathrm{CuO}_4$ for various doping levels x. The main difficulties are as follows:

(i) the experimentally observed relation $\delta \approx x$ for $x \leq 0.12$ and $\delta \approx$ const for $x \geq 0.12$; since, according to Hall measurements, the value of x in $\mathrm{La}_{2-x}\mathrm{Sr}_x\mathrm{CuO}_4$ is not equal to the concentration of hole carriers (which, at the same time, is strongly temperature dependent), the relation $\delta \approx x$ indicates the connection of the spin texture parameters with the concentration of Sr ions rather than with the concentration of charge carriers;

(ii) transition from diagonal to parallel stripes for $x \approx 0.06$;

(iii) transition to dynamic stripes for $x > 0.07$ and repeated appearance of static correlations in a narrow concentration range for $x \approx 0.12$ (so-called pinning of stripes);

(iv) one-dimensional nature of diagonal stripes and two-dimensional nature of parallel stripes;

(v) tilt (~3°) of parallel stripes for $x \approx 0.12$;

(vi) $2c$ periodicity of stripe modulation in the direction of the c axis (c is the distance between CuO_2 planes in $\mathrm{La}_{2-x}\mathrm{Sr}_x\mathrm{CuO}_4$).

To overcome the difficulties in analysis of the results of neutron diffraction experiments, Gooding *et al.* [19, 20] proposed a physical model of spin glass that was based on the assumption of a random distribution of localized doped holes. According to [20], doped holes in the spin glass phase are localized in the CuO_2 plane. Such a hole localized in a certain region produces a long-range spin-distortion field around it. The arising distortions of the AFM background can be described as the generation of the topological excitation of a skyrmion [21, 22] with a topological charge of $Q = \pm 1$ corresponding to rotation (twisting) of the AFM order parameter in the vicinity of the localized hole. Thus, doping breaks the long-range AFM order and leads to the formation of disoriented AFM-ordered microdomains whose boundaries (domain walls) are determined by localized doped holes, while the directions of AFM ordering in adjacent microdomains are turned relative to each other through a certain angle (so-called spin twisting). Here, we are going to give an alternative explanation for the observed charge and spin modulation in $\mathrm{La}_{2-x}\mathrm{Sr}_x\mathrm{CuO}_4$ using some concepts of the model developed in [19, 20] in combination with our concepts on the mechanism of the formation of negative U centers (NUC) and ordering of Sr ions.

Our analysis will be based on our earlier assumption [23] that doped holes are rigidly localized in the nearest neighborhood of a doped ion at low temperatures. More precisely, holes are localized in the CuO_2 plane at four oxygen ions belonging to the oxygen octahedron adjacent to the dopant ion (Fig. 2a). This conclusion follows from analysis of the fine structure of the edge of the x-ray absorption spectrum (XAFS) [24] and from the measurements of the NMR spectra [25].

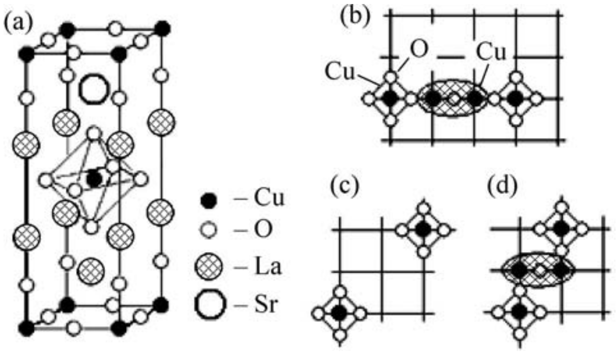

Fig. 2. Formation of negative U centers in $\mathrm{La}_{2-x}\mathrm{Sr}_x\mathrm{CuO}_4$. (a) Unit cell of $\mathrm{La}_{2-x}\mathrm{Sr}_x\mathrm{CuO}_4$. Negative U centers (shaded ellipse) are formed at a pair of neighboring Cu ions if a doped hole is localized at a distance a from each of these ions. This is equivalent to the condition that the distance between doped holes is (b) $3a$ or (d) $a\sqrt{5}$. In the intermediate case, when the distance between external Cu ions is (c) $a\sqrt{8}$, the above condition cannot be satisfied and no NUCs are formed.

In accordance with [23], doping of $\mathrm{La}_{2-x}\mathrm{Sr}_x\mathrm{CuO}_4$ results in the formation of NUCs at the pairs of adjacent Cu cations in the CuO_2 plane. These NUCs are formed at a pair of adjacent Cu ions if a doped hole is localized at a distance a from each of these ions. In other words, a NUC is formed at the inner pair of Cu ions belonging to a $\mathrm{Cu}_4\mathrm{O}_n$ cluster if a doped hole is localized in each of the oxygen squares surrounding outer Cu ions. This requirement is satisfied when the distance between outer Cu ions (or, which is the same, between the projections of dopants or doped holes) is equal to $3a$ or $a\sqrt{5}$, where a is the lattice constant in the CuO_2 plane (Figs. 2b and 2d). In the intermediate case, when the distance between outer Cu ions is $a\sqrt{8}$ (Fig. 2c), the above condition cannot be satisfied and no NUC is formed.

According to [23], two-particle hybridization of oxygen $p_{x,y}$ states with paired states of NUCs determines the anomalous behavior of HTSC materials. Electron pairing in such systems, which is responsible for superconductivity, occurs due to strong renormalization of the electron–electron interaction when scattering processes with intermediate virtual states of NUCs are taken into account [26–32]. Negative U centers act as pair acceptors leading to the generation of extra holes [23], which are also localized in the vicinity of the same NUCs. Conduction (superconductivity) is observed in such a system when localization regions of generated hole carriers form a percolation cluster either through quantum tunneling between such clusters or

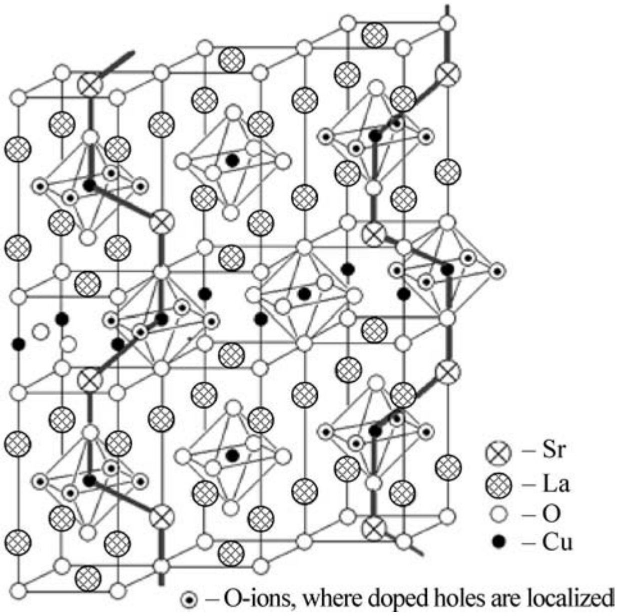

Fig. 3. Ordering of Sr ions in $La_{2-x}Sr_xCuO_4$. Negatively charged Sr ions together with doped holes "assigned" to them form dipoles attracting each other with opposite ends, forming "crankshaft" chains.

when such isolated clusters are embedded in a metal matrix.

In the doping scheme considered here, the system formed by an Sr ion and a hole localized in an oxygen square is an electric dipole interacting with other similar dipoles via the long-range Coulomb potential. In such systems, orientation interaction occurs between dipoles; as a result, the dipoles are aligned so that opposite poles face one another. The crystal structure of the compound implies that substitution of Sr for La in LSCO occurs so that the emerging dipoles form chains (similar to crankshafts) extended along the c axis (Fig. 3).

We assume that the chains are two-dimensional and are parallel to each other. The calculation of the energy of electrostatic interaction between dipole chains shows that the two nearest chains attract each other if the distance between doped holes is $l_{\rm com} \geq \sqrt{2}$,[1] whereas next to nearest chains repulse each other. This type of interaction leads to ordering of dipole chains; as a result, doped holes (or projections of Sr ions) in the CuO_2 plane occupy positions at the sites of the square lattice with a certain parameter $l_{\rm com}$, which is commensurate with the lattice constant a of the CuO_2 plane. Calculations show that the energy of interaction between dipole chains has a minimum corresponding to $l_{\rm com} = \sqrt{8}$. In addition, the energies of configurations with $l_{\rm com} = 2$, $\sqrt{5}$, $\sqrt{8}$, and 3 are close to each other within an accuracy of $\sim 10^{-2}\ e^2/\varepsilon a$ per dipole (ε is the dielectric constant); consequently, such configurations may coexist in the form of microscopic domains in which doped holes occupy positions in lattices with different $l_{\rm com}$ values.

Domains corresponding to a given $l_{\rm com}$ value can exist only in a certain range of concentration x. This range is bounded from above by the value $x_{\rm com} = 1/l_{\rm com}$, above which the existence of physically significant domains with the given $l_{\rm com}$ value does not correspond to the condition of constant average concentration. For $x < x_{\rm com}$, dipole chains are broken and vacancies appear in the square lattices of projections. Microdomains with a given $l_{\rm com}$ value are conserved up to a certain value of $x = x_l$, which corresponds to the 2D percolation threshold $x_l = 0.593/l_{\rm com}$ for a random distribution. Accordingly, domains with a given $l_{\rm com}$ value can exist for concentrations satisfying the condition

$$0.593/l_{\rm com}^2 < x \leq 1/l_{\rm com}^2. \tag{1}$$

The size of such ordered microscopic domains depends on x and increases as x approaches $x_{\rm com}$. The patterns of ordering of Sr along the c axis in a given microdomain is repeated in each second plane.

We assume that, for small x values (for a mean distance $l > 3a$ between projections of Sr ions), dipole chains in the planes parallel to the c and a axes are arranged so that the distance between doped holes along the a axis is $a\sqrt{8}$; i.e., it corresponds to the minimum of the interaction energy. Thus, the above analysis shows that a $La_{2-x}Sr_xCuO_4$ crystal for a given x value should be treated as a system of mutually penetrating domains, in which doped holes occupy (partly or completely) the positions in square lattices with various $l_{\rm com}$ values. The regions of existence of microdomains with $l_{\rm com} = \sqrt{5}$ and 3 and $l_{\rm com} = \sqrt{8}$ are shown in Fig. 1b by dashed and bold rectangles, respectively.

Let us now consider spin textures that can be formed upon such an ordering of localized doped holes. We will first try to determine the form of the spin texture (differing from the classical stripe pattern) for certain strictly ordered distributions of doped holes with $x = x_{\rm com}$, which leads to the experimentally observed spin modulation pattern. This can be done because there are no reasons to doubt the validity of the stripe model for an ordered distribution. Moreover, it follows from experiment [18] that the correlation length in the concentration range $0.06 < x < 0.12$ (the region of parallel stripes) increases from 25 Å for $x \approx 0.06$ to 200 Å for $x \approx 0.12$. It is natural to attribute the increase in the length of the correlation region to the ordering of individual AFM-ordered domains and to assume that the latter is, in turn, connected with the ordering of doped holes and, accordingly, dopant ions. We will consider below the transformation of the assumed structure upon a decrease in the value of $x < x_{\rm com}$ and a departure from

---

[1] This condition corresponds to the experimentally determined solubility limit $x_{\rm lim} \approx 0.25$ for the Sr impurity in La_2CuO_4.

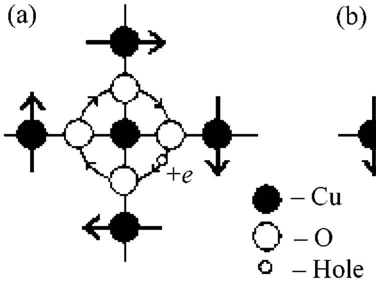

Fig. 4. Rotation of (bold arrows) the spins of copper ions in the vicinity of a doped hole (localized in the CuO_2 plane at four oxygen ions around a Cu ion), which correspond to topological charges Q = (a) 1 and (b) –1 of a skyrmion.

the strictly ordered hole distribution and will show that the main experimentally determined relations existing for a perfect lattice of holes for $x = x_{com}$ are conserved in a certain range of concentrations $x < x_{com}$.

Thus, we consider the case of complete ordering for $x_{com} = 1/8$. We assume that (i) each hole circulates over the oxygen square surrounding a copper ion and (ii) the nearest four copper atoms are polarized as a result of the interaction between the hole current and their spins and the emerging distortions of the AFM background can be described as the generation of a skyrmion with a topological charge of ±1 (Fig. 4).

Figure 5a shows a possible ordering of the spin projections of Cu ions onto the CuO_2 plane for the completely ordered arrangement of localized holes for $x = x_{com} = 1/8$ when they form a $\sqrt{8} \times \sqrt{8}$ square lattice. In this case, the CuO_2 plane splits into individual quadrangular AFM-ordered microdomains, whose angles are determined by localized doped holes. The projections of the directions of spins at Cu ions located at the lattice sites onto the CuO_2 plane are shown by arrows. The matched ordering emerging in this case is characterized by the AFM ordering of microdomains themselves, as well as by the ordered alternation of skyrmions with charges $Q = \pm 1$. It follows from Fig. 5a that such an ordering leads to an imitation of the magnetic stripe texture [1]. The period of magnetic modulation in this case is equal to the total size of two antiphase domains in the direction of the modulation vector and contains two sites over the length of a period in a stripe of width $l_{com}/\sqrt{2}$,

$$T = 2\sqrt{2} l_{com} = 8; \quad \delta = 1/8 = x, \tag{2}$$

in accordance with the experiment. This pattern is consistent with the results obtained in [33], where the existence of AFM-ordered microdomains with a size of 15–30 Å was detected in $La_{1.88}Sr_{0.12}CuO_4$ by the μsR relaxation method; the directions of magnetization in such domains are correlated over a length of 600 Å. It should be noted that, according to Fig. 5a, charged stripes in the form predicted by the theory do not exist in the present case. However, in the case considered here, we obtain commensurate modulation, which give no satellite peaks in the diffraction patterns. Satellite reflections might appear only in the case of incommensurate modulation. In addition, charge modulation is also observed in the experiment [1] in the form of the incommensurate splitting of lattice peaks (2 ± 2ε, 0, 0) and (0, 2 ± 2ε, 0).

To explain this result, let us pass from the completely ordered lattice of doped holes for $x = 1/8$ to their

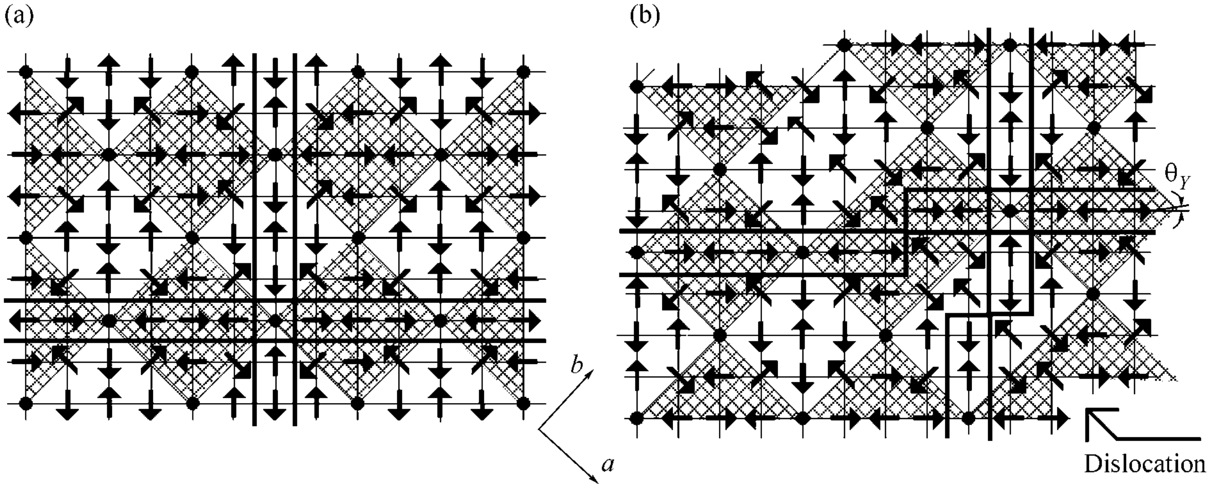

Fig. 5. Projections of the spins of Cu ions under ordering of doped holes in a $\sqrt{8} \times \sqrt{8}$ lattice for (a) $x = 1/8$, microdomains forming horizontal stripes are shaded; thick lines mark the directions of parallel stripes, and (b) $x < 1/8$, the plane is split into domains separated by diagonal dislocations, which are nuclei of diagonal stripes. The displacement of vertical stripes by one cell at each dislocation leads to the effective "tilt" of vertical stripes through the angle θ_Y.

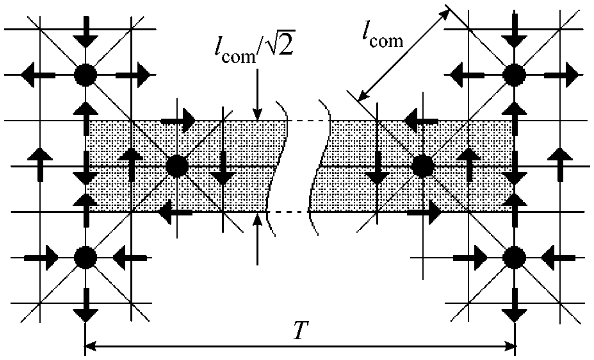

Fig. 6. Fragment of a magnetic stripe texture. Closed circles correspond to the projections of Sr ions onto the CuO_2 plane. Arrows show the directions of spin projections at Cu sites. Two filled sites (shaded rectangle of area $Tl_{com}/\sqrt{2}$) are located in a stripe of width $l_{com}/\sqrt{2}$ over the magnetic structure period T.

distribution for $x < 1/8$. We will first consider the experimental data obtained in the region of existence of static parallel stripes for $x \approx 0.12$ [18, 34]. This will allow us to carry out a detailed comparison of the experimental result with our model.

Modulation of the spin texture with an incommensurability parameter $\delta = 0.118$ was observed on a $La_{1.88}Sr_{0.12}CuO_4$ sample in [34]. This corresponds to the average period $T \approx 8.5$ of the texture (in units of a), i.e., to alternation of two periods $T_1 = 8$ and $T_2 = 9$. Figure 5b shows the proposed pattern of the ordered distribution of doped holes (and, hence, dopant projections) for the average concentration $x = 0.118$, which is obtained by “cutting” the completely ordered distribution for $x = 0.125$ along the orthorhombic a axis and by displacing one of its parts relative to the other by the vector $\mathbf{q} = (1, 1)$. Such a displacement conserves the coherence of ordering in domains located on both sides of the dislocation and “shifts” the system of parallel stripes by one cell upon passing through the cut.[2] Such a structure (Fig. 5b) produces typical reflections in the diffraction patters, which correspond to the incommensurate modulation of both spin (with incommensurability parameter δ) and charge (with incommensurability parameter 2δ). The condition of conservation of average concentration yields

$$T_d x_l = (T_d + 1)x_m. \quad (3)$$

Here, T_d is the mean period of dislocations in units of a and x_l is the local concentration of holes in a domain. To preserve the mean concentration $x_m = 0.118$ for a local concentration $x_l = 0.125$, the diagonal dislocations being introduced must have an average period of $T_d = T_1 + T_2 = 17$. Such quasiperiodic dislocations leading to the incommensurate modulation of both the crystal structure and the spin texture ensure the observation of incommensurate reflections in diffraction experiments.

A feature of the emerging ordering pattern is that parallel stripes are displaced by a lattice constant (see Fig. 5b). In other words, these stripes seem to be inclined at an angle of $\theta_Y = 1/17 \approx 3.3°$ to the tetragonal b axis. Such tilted parallel stripes with a slope of 3° were observed in $La_{1.88}Sr_{0.12}CuO_4$ [34].

Let us now consider the case of arbitrary values $x < 1/8$. The distribution pattern in this case can be obtained from the completely ordered distribution for $x = 1/8$ by successive introduction of such dislocations. The texture imitating parallel stripes can exist as long as microdomains with $l_{com} = \sqrt{8}$ exist, i.e., in the concentration range $0.075 < x < 0.125$, in the case of a uniform distribution of Sr ions (bold triangle in Fig. 1b). However, microdomains with $l_{com} = \sqrt{8}$ can be conserved to lower x values (thick dashed lines in Fig. 1b) due to fluctuations of the Sr concentration in small volume elements. The parallel stripe structure is observed in experiments down to $x = 0.06$ (see Fig. 1a).

Let us suppose that the lattice contains such correlated residual fragments of the parallel stripe texture, which are genetically related to microdomains with $l_{com} = \sqrt{8}$ (Fig. 6). In this case, characteristic reflections determined by the mean period of the residual texture are observed in the neutron diffraction pattern. In turn, the mean period T of this texture, which is defined as the distance between the centers of single-phase magnetic microdomains, includes two occupied sites as in the case of complete ordering; i.e., a rectangle of area $Tl_{com}/\sqrt{2} = 2T$ (shaded in the figure) must contain two sites. This condition gives

$$2Tx = 2, \quad \delta = 1/T = x. \quad (4)$$

Thus, the relation $\delta = x$ is accidental to a certain extent and is due to the fact that, in the case of parallel stripes, holes lie on straight lines separated by a distance of $2a$ from each other.

As seen in Fig. 5b, introduced dislocations are in fact the nuclei of diagonal stripes extended along the orthorhombic a axis. The dislocations are manifested in the form of a quasiperiodic structure for $x < 0.075$, when the traces of the $\sqrt{8} \times \sqrt{8}$ texture disappear and only the diagonal rows of impurity dipoles separated by a distance $l_{com} = \sqrt{8}$ remain, the distance between the rows being $l \geq 2\sqrt{8}$. Consequently, diagonal stripes are always directed along the orthorhombic a axis and the modulation vector is accordingly directed along the other orthorhombic b axis.

If all doped holes are ordered to diagonal charge stripes, the period T of the diagonal spin modulation (in

---

[2] In fact, we assume that chains of dipoles (and, hence, vacancies) tend to be aligned along the orthorhombic a axis; we believe that this is associated with the requirement of deformation stress minimization.

tetragonal axes) must be equal to $1/\sqrt{2}x$ (or $\delta = \sqrt{2}x$). Since some doped holes remain in the space between charge stripes, the period of the observed spin texture is larger than $1/\sqrt{2}x$ and, accordingly, δ is smaller than $\sqrt{2}x$. The experimentally obtained value of δ [16] varies from $\delta \approx 0.7x$ to $\delta \approx 1.4x$ in the concentration range $0.01 < x < 0.05$.

The last question considered here concerns static and dynamic stripes. Figure 1b shows the concentration regions in which parallel and diagonal stripe textures can exit. Dashed lines in the same figure bound the regions of the existence of percolation chains with $l_{\text{com}} = \sqrt{5}$ and 3. Such chains of doped holes in the CuO_2 plane adjoin a cluster of AFM microdomains. In accordance with the above arguments, NUCs playing the role of pair acceptors are formed on pairs of adjacent Cu ions in the regions corresponding to the existence of percolation clusters with $l_{\text{com}} = \sqrt{5}$ and 3. In these regions, conduction occurs along the corresponding NUC chains located on percolation clusters. The appearance of conduction disturbs static spin correlations in the surrounding regions due to the motion of charges breaking the magnetic order along their trajectory. In this case, spin correlations can be observed only in the inelastic neutron scattering as dynamic incommensurate magnetic fluctuations. It is remarkable (see Fig. 1b) that, in addition to the region $x < 0.07$, there is a narrow range of concentrations $0.11 < x < 0.125$ in which percolation in NUCs is absent. Static incommensurate correlations are again observed in this range. It should also be noted that microdomains with $l_{\text{com}} = \sqrt{8}$, which coexist with percolation NUC clusters with $l_{\text{com}} = \sqrt{5}$, can also be formed for the mean value of $x > 0.125$ due to fluctuations of the Sr concentration in small volume elements. This behavior makes it possible to observe a parallel texture with $\delta = 0.125$, but again in the form of dynamic spin modulation.

Thus, we have proved that the proposed model of $La_{2-x}Sr_xCuO_4$, which implies the formation of diatomic NUCs in the CuO_2 plane and is based on the assumptions concerning the ordering of Sr and localization of doped holes, can provide a detailed explanation of the experimentally observed spin textures in the entire doping range. In the framework of the model considered here, all features of the stripe phase diagram of $La_{2-x}Sr_xCuO_4$ are associated only with the geometrical relations existing for the square lattice and with the competition between different types of ordering of Sr ions.

REFERENCES

1. J. M. Tranquada, J. D. Axe, N. Ichikawa, *et al.*, Phys. Rev. B **54**, 7489 (1996).
2. J. Zaanen and O. Gunnarson, Phys. Rev. B **40**, 7391 (1989).
3. D. Poilblanc and T. M. Rice, Phys. Rev. B **39**, 9749 (1989).
4. S. A. Kivelson, V. J. Emery, and H.-Q. Lin, Phys. Rev. B **42**, 6523 (1990).
5. H. Schulz, Phys. Rev. Lett. **64**, 1445 (1990).
6. M. Inui and P. Littlewood, Phys. Rev. B **44**, 4415 (1991).
7. G. An and J. M. van Leeuwen, Phys. Rev. B **44**, 9410 (1991).
8. V. J. Emery and S. A. Kivelson, Physica C (Amsterdam) **209**, 597 (1993).
9. C. C. Castellani, C. Di Castro, and M. Grilli, Phys. Rev. Lett. **75**, 4650 (1995).
10. Q. Si, Y. Zha, K. Levin, and J. P. Lu, Phys. Rev. B **47**, 9055 (1993).
11. T. Tanamoto, H. Kohno, and H. Fukuyama, J. Phys. Soc. Jpn. **63**, 3739 (1994).
12. R. S. Markiewicz, Phys. Rev. B **56**, 9091 (1997).
13. V. I. Belyavsky and Y. V. Kopaev, Phys. Lett. A **287**, 152 (2001).
14. K. Yamada, C. H. Lee, K. Kurahashi, *et al.*, Phys. Rev. B **57**, 6165 (1998).
15. K. Yamada, C. H. Lee, Y. Endoh, *et al.*, Physica C (Amsterdam) **282–287**, 85 (1997).
16. M. Matsuda, M. Fujita, K. Yamada, *et al.*, Phys. Rev. B **65**, 134515 (2002).
17. M. Fujita, K. Yamada, H. Hiraka, *et al.*, Phys. Rev. B **65**, 064505 (2002).
18. M. Fujita, H. Goka, K. Yamada, *et al.*, Phys. Rev. B **66**, 184503 (2002).
19. R. J. Gooding, N. M. Salem, and A. Mailhot, Phys. Rev. B **49**, 6067 (1994).
20. R. J. Gooding, N. M. Salem, R. J. Birgeneau, *et al.*, Phys. Rev. B **55**, 6360 (1997).
21. A. A. Belavin and A. M. Polyakov, Pis'ma Zh. Éksp. Teor. Fiz. **22**, 503 (1975) [JETP Lett. **22**, 245 (1975)].
22. R. J. Gooding, Phys. Rev. Lett. **66**, 2266 (1991).
23. K. V. Mitsen and O. M. Ivanenko, Zh. Éksp. Teor. Fiz. **118**, 666 (2000) [JETP **91**, 579 (2000)].
24. V. Polinger, D. Haskel, and E. A. Stern, AIP Conf. Proc. **483**, 241 (1999).
25. P. C. Hammel, B. W. Statt, R. Lmartinye, *et al.*, Phys. Rev. B **57**, R712 (1998).
26. E. Simanek, Solid State Commun. **32**, 731 (1979).
27. C. S. Ting, D. N. Talwar, and K. L. Ngai, Phys. Rev. Lett. **45**, 1213 (1980).
28. B. A. Volkov and V. V. Tugushev, Pis'ma Zh. Éksp. Teor. Fiz. **46**, 193 (1987) [JETP Lett. **46**, 245 (1987)].
29. G. M. Éliashberg, Pis'ma Zh. Éksp. Teor. Fiz. **46** (Suppl.), 94 (1987) [JETP Lett. **46**, S81 (1987)].
30. I. O. Kulik, Fiz. Nizk. Temp. **13**, 879 (1987) [Sov. J. Low Temp. Phys. **13**, 505 (1987)].
31. P. I. Arseev, Zh. Éksp. Teor. Fiz. **101**, 1246 (1992) [Sov. Phys. JETP **74**, 667 (1992)].
32. J. Ranninger and A. Romano, Phys. Rev. B **66**, 094508 (2002).
33. A. T. Savici, Y. Fudamoto, I. M. Gat, *et al.*, Phys. Rev. B **66**, 014524 (2002).
34. H. Kimura, H. Matsushita, K. Hirota, *et al.*, Phys. Rev. B **61**, 14366 (2000).

Translated by N. Wadhwa

JETP Letters, Vol. 82, No. 9, 2005, pp. 586–589. Translated from Pis'ma v Zhurnal Éksperimental'noĭ i Teoreticheskoĭ Fiziki, Vol. 82, No. 9, 2005, pp. 664–667.
Original Russian Text Copyright © 2005 by Kapustina.

Threshold Structural Transition in Nematics in Homogeneous Ultrasonic Fields

O. A. Kapustina

Andreev Acoustics Institute, Russian Academy of Sciences, ul. Shvernika 4, Moscow, 117036 Russia
e-mail: oakapustina@yandex.ru

Received April 26, 2005; in final form, September 20, 2005

The effect of molecule reorientation in a homeotropically aligned layer of a nematic liquid crystal under the action of a transversely homogeneous ultrasonic wave is studied, and its description in terms of the new theoretical model based on the nonequilibrium thermodynamics and nonlinear hydrodynamics of liquid crystals is experimentally verified. It is shown that the effect is of a threshold character, the critical particle velocity is inversely proportional to the layer thickness, and the stationary distortion of macrostructure is uniform along the layer. *© 2005 Pleiades Publishing, Inc.*

PACS numbers: 61.30.–v

The structural transformations that occur in liquid crystals in deformation fields produced by ultrasonic waves have been much studied in the last 25 years [1]. One of the mechanisms of such transformations in homeotropically aligned nematic liquid crystals (NLCs), which had been the subject of wide speculation [2–4], consists in the reorientation of molecules under the effect of viscous moments in inhomogeneous acoustic flows. These flows are caused by the convective stresses in the viscous boundary layers, by the nonuniform compression of the NLC layer near its boundaries or near the boundaries of the ultrasonic beam, by the difference in the acoustic characteristics of the NLC and the plates enclosing the layer, and by the nonuniform intensity distribution across the ultrasonic wave. The physical models that postulate the flow mechanism of structural NLC distortions of nonthreshold character were developed and tested in the framework of linear hydrodynamics [5] in all known physical situations (an oblique incidence of an ultrasonic wave or a bounded ultrasonic beam on the NLC layer, the presence of a noticeable sound pressure gradient along the layer or the along edges of the NLC cell, etc. [1–4]).

The present paper reports the observation of a specific type of acoustically initiated orientational transition in a homeotropic NLC layer: the transition is of a threshold character and only manifests itself when a transversely homogeneous ultrasonic wave is normally incident on the mesophase layer. The measured critical amplitudes of particle velocities corresponding to the threshold of this effect are used to test the model that was developed on the basis of the theory proposed in [6, 7]. In the situation under consideration, the flow mechanism based on the Leslie–Ericksen classical linear hydrodynamic equations fails [4]. The attempt to describe the given orientational transition in terms of the conventional approach as a threshold effect that occurs in a system with periodically varying properties of the medium has also failed [7]: for the critical compression strain in an ultrasonic wave, the calculation predicted values that were one and a half or two orders of magnitude greater than the values conventionally used in experiments. Hence, the explanation of this phenomenon goes beyond the limits of classical hydrodynamics and requires another approach.

From this point of view, it is of interest to analyze the structural transitions in ultrasonic fields on the basis of the statistical methods and the nonclassical nonlinear hydrodynamics of NLCs. In terms of this approach, with the use of the molecular model [6], it was shown that a transversely homogeneous ultrasonic wave gives rise to stationary flows and moments in the NLC, which are quadratic in the strain of the medium and tend to rotate the NLC molecules so as to make them orthogonal to the direction of wave propagation. The combined action of these factors leads to a distortion of the homeotropic structure of the NLC layer in the transversely homogeneous ultrasonic wave when the intensity of ultrasound exceeds the critical value [7].

Figure 1a shows a simplified schematic diagram of the setup used for measuring the levels of ultrasound that were critical for the observation of the optical effect. Plates *1* and *2* form a flat cell filled with NLC (an eutectic mixture of 4-methoxybenzylidene-4'-butylaniline and 4-ethoxybenzylidene-4'-butylaniline). At the NLC layer edges parallel to the x axis, spacers *3* determining the layer thickness d are placed; the edges parallel to the y axis are open (Fig. 1b). The orientation of NLC molecules in the cell is homeotropic (this means that the unit vector **n** determining the direction of the predominant orientation of molecules, i.e., the director of the NLC, is parallel to the z axis). To test the homogeneity of the initial homeotropic macrostructure of NLC layer *4* in the cell and to monitor the changes in its ordering under the action of ultrasonic waves, the conoscopic method was used [1]. The optical system was designed so that a beam of linearly polarized light of intensity I_0 passed through a convex lens and converged at NLC layer *4*. Mirror coating *5* of plate *2* allowed the observation in reflected light, which made it possible to obtain high-quality conoscopic patterns even for thick samples (50–100 μm). Thin salol layer *6* provided for the coupling of the cell with the acoustic line *7*. The design of the cell allowed the variation of the NLC layer thickness in the course of measurement by moving plate *1* so that the gap between plates *1* and *2* could be varied within 10–120 μm. Such microdisplacements did not affect the boundary conditions in the cell or the energy of adhesion of NLC molecules to the cell walls. This made it possible to avoid the fluctuations in the threshold levels of ultrasound because of the aforementioned factors. The source of longitudinal ultrasonic waves was transducer *8* (Straubel-cut quartz with a quasi-uniform distribution of vibration amplitudes over the surface of the radiating plate) positioned at the lower end of the acoustic line, as shown in Fig. 1a. The acoustic contact between the transducer and the cell occurred through the thin salol layer. The level of ultrasound was controlled by the voltage applied to the transducer. The voltage was measured by a voltmeter and recalculated to the particle velocity at the boundary $z = 0$ according to the known method of calculation for a multilayer system (transducer–coupling layer–working medium) with allowance for its resonance properties. The frequency of vibrations was varied from 0.3 to 15 MHz, while the transducer operated at the fundamental frequency or its harmonics. The temperature of the NLC in the cell was maintained at a constant level (within 0.5°C) by a thermal stabilization system connected with the cell and could be varied from 22 to 45°C.

The experimental procedure was as follows: the cell was filled with NLC, the layer thickness was set by moving plate *1*, and the orientation state of the macrostructure of the NLC layer was tested. In the absence of ultrasound, the conoscopic pattern observed with crossed polarizers represented a system of concentric light and dark rings (isochromes), i.e., had a rotation symmetry about the normal to the layer. Then, voltage was applied to the transducer and increased up to the critical ultrasound level that was necessary for overcoming the elastic forces in the NLC and for the reorientation of the director, which resulted in the establishment of its new stationary distribution. This orientational transition observed under compression, $\varepsilon \geq \varepsilon_c$, visually manifested itself in a reduction of symmetry of the conoscopic pattern and in a distortion of the rings.

Two series of experiments were carried out to measure the critical levels of ultrasound: (a) at a constant frequency of vibrations, the layer thickness was varied from 10 to 100 μm (the temperature of the NLC in the cell was 26°C); (b) for the NLC layer of a fixed thickness, the frequency of vibration was varied from 0.3 to 15 MHz (the temperature of the NLC was 25°C).

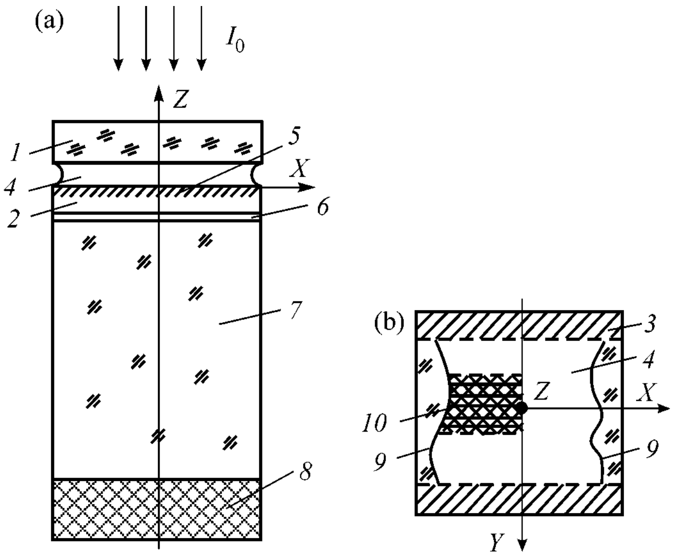

Fig. 1. The (a) side and (b) top views of the layout of the experimental setup: (*1*, *2*) plates, (*3*) spacers, (*4*) nematic-liquid-crystal layer, (*5*) mirror coating, (*6*) adhesion layer (salol), (*7*) rod serving as the acoustic line, (*8*) source of longitudinal ultrasonic waves, (*9*) the open edge of the nematic-liquid-crystal layer in the cell, and (*10*) the region observed in the nematic-liquid-crystal layer.

Figure 2a shows a typical dependence of the critical amplitude of the particle velocity V_{0c} on the layer thickness d at a constant ultrasonic frequency of 2.7 MHz. One can see that this dependence is approximated by the function $V_{0c} \sim 1/d$. Figure 2b displays the influence of the ultrasonic frequency on the critical particle velocity at a constant layer thickness of 40 μm. From these data, it follows that, at a constant layer thickness, the relation between the critical amplitude of the particle velocity and the ultrasonic frequency depends on the choice of the ultrasonic frequency range. Within 0.3–1.2 MHz, the critical amplitude decreases with increasing frequency according to the law $V_{0c} \sim 1/\omega$, whereas, in the frequency range from 2.7 to 15 MHz, the effect is frequency independent and the critical particle velocity has a constant value. Here, $\omega = 2\pi f$, where f is the frequency of vibrations.

Let us discuss the above experimental data on the behavior of the critical levels of ultrasound with varying thickness of the NLC layer and varying frequency of vibrations in terms of the theoretical model proposed in [7]. The geometry of the problem is as follows: the NLC layer lies in the (xy) plane, the z axis is perpendicular to the layer, the coordinate $z = 0$ corresponds to the lower acoustically transparent boundary of the layer, and the coordinate $z = d$ corresponds to the upper acoustically rigid boundary (Fig. 1). An ultrasonic

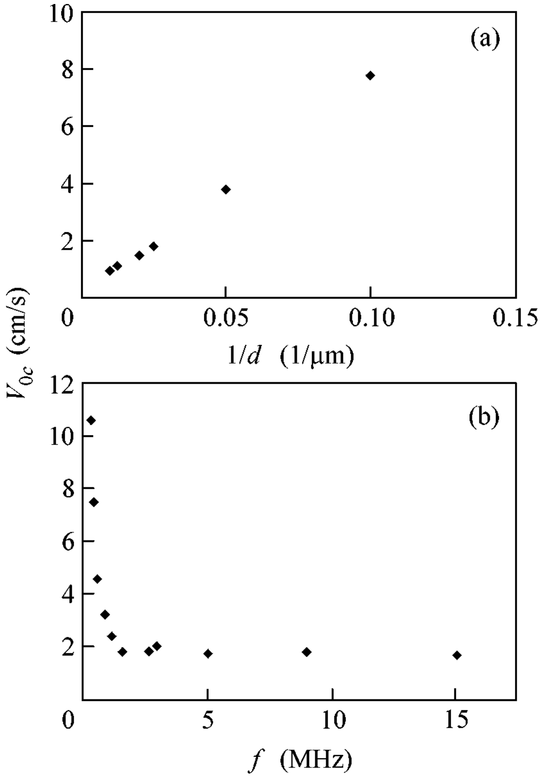

Fig. 2. Critical amplitude of the particle velocity vs. the (a) inverse thickness of the nematic-liquid-crystal layer at a frequency of 2.7 MHz at 26°C and (b) frequency for the nematic-liquid-crystal layer with a thickness of 40 μm at 25°C.

wave, homogeneous in its cross section, with a particle velocity amplitude V_0 is incident on the layer from below in the direction of the z axis. The problem is considered for the frequency range where the sound wavelength is greater than the layer thickness. In the layer, a periodic compression takes place with the amplitude $\varepsilon = 2V_0/c$, where c is the velocity of ultrasound propagation in the NLC. The theory is developed in the framework of the statistical hydrodynamics of liquid crystals on the basis of the microscopic NLC model [6]. The latter describes the rotation of an individual molecule caused by the external action and producing microstresses and micromoments in the medium. By averaging these microstresses and micromoments over the nonequilibrium angular distribution of molecule orientation and over the period of the ultrasonic wave, it is possible to separate the stationary nonlinear stresses $\sigma_{ij}^{(2)}$ and moments that arise in the NLC under the effect of ultrasonic waves and may lead to a reorientation of the NLC molecules. It is essential that the time averaging of microstresses is performed with allowance for the relaxation character of the relation between the sound pressure P and the strain ε_{kk} in the ultrasonic wave: $P = -[E\varepsilon_{kk} + \mu(\omega)U_{kk}]$. Here, E is the bulk elastic modulus, $\mu(\omega)$ is the bulk viscosity coefficient determining the sound absorption in the NLC, and U_{kk} is the strain rate of the medium. According to [7], the stationary distortion of the homeotropic NLC layer structure is assumed to satisfy the following conditions: (i) the flow of the liquid and the rotation of molecules occur in the (xz) plane and are homogeneous along the layer; (ii) the angle θ of the director deviation from the z axis is small ($\theta \ll 1$). It is important that the equation for the flow velocity $V_x^{(2)}$ in the (xz) plane takes into account not only the nonlinear stationary stress $\sigma_{xz}^{(2)}$ but also the shear stress $\sigma_{xz} = \eta_2 V_{x,zz}^{(2)}$ arising in the stationary flows caused by the effect of the nonlinear stresses. These nonlinear and shear stresses tend to overcome the effect of the Frank elastic moments [5], which stabilize the initial homeotropic orientation of molecules in the NLC layer, and tend to rotate them in the (xz) plane toward the position orthogonal to the direction of ultrasonic wave propagation. The critical amplitude of the compression strain in the wave at the threshold of the effect is determined from the condition of the existence of a nonzero solution given in the form $\theta = \theta_0\sin(\pi z/d)$ to the equation of the director rotation [5]. According to [7], under rigid orientational boundary conditions, this amplitude is given by the formula

$$\begin{aligned}\varepsilon_c &= (\pi/d)(K_{33}/\omega^\circ\gamma_1\xi)^{1/2} \\ &\times \{E[\partial T_c/\partial P - \alpha TV/C_p]/T\}^{-1/2} F(\omega\tau)^{-1/2}.\end{aligned} \qquad (1)$$

The analysis of this formula shows that the relation between the critical particle velocity and the layer thickness is described as $V_{0c} \sim 1/d$, which agrees well with the experimental data presented in Fig. 2a. The frequency dependence of the effect is given by the function $F(\omega\tau)$. At high frequencies, where $\omega\tau \gg 1$, this function is $F(\omega\tau) \longrightarrow 1$, and the critical particle velocity is frequency independent. In the low-frequency range, where $\omega\tau \ll 1$, the aforementioned function has the form $F(\omega\tau) \approx (\omega\tau)^2$, and the critical particle velocity is $V_{0c} \sim 1/\omega$. These theoretical predictions agree well with the experimental data presented in Fig. 2b. The frequency ω^* that separates the frequency regions with different types of $V_{0c}(\omega)$ dependences can be determined from the condition $\omega\tau = 1$. Taking $T_c - T = 1$°C and $\tau = 10^{-7}$ s [8], we obtain $\omega^* = 10^7$ s^{-1}, which yields $f^* = 1.59$ MHz. One can see that, as the ultrasonic frequency increases and passes from the region $f < f^*$ to the region $f > f^*$, a qualitative change occurs in the character of the frequency dependence of the critical particle velocity in compliance with the experimental observations. For the numerical comparison of the theoretical and experimental values of the critical particle velocity, we use the parameters of NLCs that were given in [1, 5, 8]. For MBBA, we have $K_{33} = 7 \times 10^{-7}$ dyn, $C_p = 2$ J/m^3 deg, $\partial T_c/\partial P = 3 \times 10^{-8}$ deg cm^2/dyn, $\gamma_1 = 0.78$ P, $E = 2 \times 10^{10}$ dyn/cm^2, $\alpha = 10^{-4}$ deg^{-1}, and $c = 1.5 \times 10^3$ m/s. According to [7], at $T_c - T = 10$°C, we have $\omega^\circ \approx 6 \times 10^7$ while the coefficients ξ_1 and ξ_2 are equal to 1.15 and 1.2, respectively. The closeness of these coefficients suggests that the stationary nonlinear flows and the moments play approximately identical roles in the mechanism of the director reorientation under the effect of a transversely homogeneous ultrasonic wave. Using the aforementioned values, from Eq. (1) we obtain the following critical parameters for the layer with a thickness of 100 μm at a frequency of 2.7 MHz: $e_{0c} = 2 \times 10^{-5}$ and $V_{0c} = 1.5$ cm/s, which agrees well with the experimental data in the frequency region $f > f^*$ where the effect is frequency-independent (Fig. 2).

Thus, the experimental results presented in this paper agree both qualitatively and quantitatively with the theoretical calculations performed in terms of the model proposed in [7]. This proves the validity of the model and, hence, justifies the use of the approach based on the nonequilibrium thermodynamics and statistical hydrodynamics in analyzing the threshold orientational transitions in NLCs in ultrasonic fields.

I am grateful to Prof. E. Guyon for useful discussions. This work was supported in part by the Russian Foundation for Basic Research, project no. 04-02-17454.

REFERENCES

1. *Handbook of Liquid Crystals*, Ed. by D. Demus *et al.* (Wiley, Weinheim, 1998).
2. *Physical Properties of Liquid Crystals* (Wiley, Weinheim, 1999).
3. A. P. Kapustin and O. A. Kapustina, *Acoustics of Liquid Crystals* (Nauka, Moscow, 1986) [in Russian].
4. O. A. Kapustina, Kristallografiya **49**, 759 (2004) [Crystallogr. Rep. **49**, 703 (2004)].
5. S. A. Pikin, *Structural Transformations in Liquid Crystals* (Nauka, Moscow, 1981; Gordon and Breach, New York, 1991).
6. E. N. Kozhevnikov, Akust. Zh. **42**, 800 (1996) [Acoust. Phys. **42**, 705 (1996)].
7. E. N. Kozhevnikov and N. G. Dolmatova, Vestn. Samar. Gos. Univ., No. 2, 142 (2003).
8. N. A. Tikhomirova, L. K. Vistin', and V. N. Nosov, Kristallografiya **17**, 1000 (1972) [Sov. Phys. Crystallogr. **17**, 878 (1972)].

Translated by E. Golyamina

JETP Letters, Vol. 82, No. 9, 2005, pp. 590–593. Translated from Pis'ma v Zhurnal Éksperimental'noĭ i Teoreticheskoĭ Fiziki, Vol. 82, No. 9, 2005, pp. 668–671.

Observation of Electric Polarization in $Gd_{1-x}Sr_xMnO_3$ ($x = 0.5, 0.6, 0.7$) Single Crystals

A. M. Kadomtseva[a], Yu. F. Popov[a], G. P. Vorob'ev[a], V. Yu. Ivanov[b], A. A. Mukhin[b], and A. M. Balbashov[c]

[a] *Moscow State University, Vorob'evy gory, Moscow, 119992 Russia*
e-mail: Kadomts@plms.phys.msu.ru
[b] *General Physics Institute, Russian Academy of Sciences, ul. Vavilova 38, Moscow, 119991 Russia*
[c] *Moscow Power Engineering Institute (Technical University), ul. Krasnokazarmennaya 14, Moscow, 105835 Russia*

Received September 21, 2005

In $Gd_{1-x}Sr_xMnO_3$ ($x = 0.5, 0.6, 0.7$) single crystals, a change in electric polarization ($\Delta P \sim 100\ \mu K/m^2$) is found to accompany the suppression of the charge-ordered spin-glass state and the transition to the ferromagnetic conducting phase ($H_{cr} \sim 100$ kOe at 4.5 K). The transition is also characterized by jumps in magnetization and magnetostriction. The sign of the induced polarization depends on the polarity of the electric field in which the sample was preliminarily cooled. This dependence testifies to the presence of spontaneous electric polarization in the system. The effect is maximal at $x = 0.5$ and decreases by more than an order of magnitude as x increases to 0.7. The phenomenon observed in the experiment may be associated with the new noncentrosymmetric structures with an electric dipole moment that were recently predicted for manganites ($x \sim 0.5$) [Nature Materials **3**, 853 (2004)]. These structures exhibit charge-orbital ordering such that e_g electrons are not localized by one of the manganese ions but distributed between neighboring ions, thus forming an ordered dimer structure. © *2005 Pleiades Publishing, Inc.*

PACS numbers: 75.80.+q

INTRODUCTION

Rare-earth (R) manganites, $RMnO_3$, with an orthorhombically distorted perovskite structure (space group *Pbnm*) are well known as the parent materials for compounds whose doping with Sr^{2+} and Ca^{2+} ions leads to the effect of colossal magnetoresistance and other interesting phenomena related to strong interactions of spin, orbital, charge, and lattice degrees of freedom (see, e.g., [1]). In recent years, new properties of $RMnO_3$ (R = Gd, Tb, Dy) manganites were revealed, namely, the properties associated with spontaneous electric polarization in the region of the existence of modulated spin structures [2–4], which are formed due to the frustration of exchange interactions with decreasing ionic radius of the R ion. As for the doped manganites, the presence of states with electric polarization in them remains open to question, although prerequisites for such a presence are known: for example, the dielectric anomaly observed in $Pr_{0.67}Ca_{0.33}MnO_3$ [5] or the new type of charge ordering with e_g electron localization in the middle of the Mn–O–Mn bond (Zener polaron) in $Pr_{0.6}Ca_{0.4}MnO_3$ [6]. The latter possibility was discussed and substantiated in theoretical publications [7–9]. Recently, it was theoretically shown [10] that, in doped manganites of the $R_{1-x}Ca_xMnO_3$ type at $x \sim 0.5$, not only can the Zener polarons and the CE-type classical antiferromagnetic structure with charge and orbital ordering of Mn^{3+}/Mn^{4+} ions be present, but also more complex structures are possible, with e_g electrons asymmetrically distributed between neighboring Mn ions and forming an ordered dimer structure possessing an electric dipole moment. In the latter case of charge ordering, the center of symmetry of the system is absent and a spontaneous electric polarization may appear.

In this paper, we report on the search for the electric polarization in $Gd_{1-x}Sr_xMnO_3$ ($x = 0.5, 0.6, 0.7$) single crystals and on the observation of this polarization in the given system. Previous studies of the magnetic, magnetoelastic, and conducting properties of polycrystalline $Gd_{0.5}Sr_{0.5}MnO_3$ samples revealed the presence of a charge ordering in this material at temperatures below $T \sim 90$ K, which coexists with the spin cluster glass state at $T \leq 42$ K [11, 12]. The absence of long-range magnetic order was confirmed by neutron diffraction studies [11]. For the same composition in the low-temperature region, the effect of colossal magnetoresistance due to the charge ordering suppression and the field-induced metal–insulator transition was observed in magnetic fields up to 150 kOe [11].

EXPERIMENTAL RESULTS AND DISCUSSION

The $Gd_{1-x}Sr_xMnO_3$ ($x = 0.5, 0.6, 0.7$) single crystals were grown by the floating zone method with optical heating. Comprehensive studies of magnetic, conducting, magnetoelectric, and magnetoelastic properties of these compositions were carried out in constant (up to 12 kOe) and pulsed (up to 250 kOe) magnetic fields in the temperature range 4.2–300 K.

Magnetic measurements confirmed the absence of spontaneous magnetization in all of the compositions under study. The temperature dependence of resistivity (Fig. 1) exhibited a thermal activation behavior without any peculiar anomalies in the presence of charge ordering at T_{CO} ~ 90 K in accordance with the data reported for polycrystals with $x = 0.5$ [11]. However, the resistivity value in our experiments was about an order of magnitude smaller than in the aforementioned polycrystals, presumably because of the contribution of intergrain boundaries in the latter.

Figure 2 shows the magnetization curves for a $Gd_{0.5}Sr_{0.5}MnO_3$ single crystal. One can see that, in the low-temperature region at H_{cr} ~ 100 kOe, the magnetization increases stepwise. This is related to the suppression of charge ordering and the first-order transition to ferromagnetic state, which, according to [11], is conducting. The phase transition exhibits a hysteresis, which is maximal at low temperatures and decreases rapidly with increasing *T*. The transition is also accompanied by anomalies of longitudinal magnetostriction (Fig. 3). These anomalies are observed at the same value of the threshold field at which the magnetization increases sharply (Fig. 2) and the resistivity decreases (according to the data of [11]) by several orders of magnitude. All these features testify to a strong spin–charge–lattice correlation in the system under study.

The fundamental result of our study is the observation of a drastic change in electric polarization $\Delta P(H)$ near the threshold field (Fig. 4). The sign of the polarization was found to depend on the polarity of the electric field $E = \pm 120$ kV/m in which the sample was preliminarily cooled. This fact testifies to the presence of a spontaneous electric polarization in the system. The sharp decrease in polarization that occurs after its step increase at H_{cr} is caused by the fact that, at the transition of the crystal from dielectric to conducting state, the induced charge leaks through the sample from the metallized plates applied to it and causes a drop in the induced polarization $\Delta P(H)$ in the region of $H \geq H_{cr}$.

In $Gd_{0.4}Sr_{0.6}MnO_3$, for which no data on magnetic and electric properties could be found in the literature, we also observed a strong increase in electric polarization $\Delta P(H)$ in a magnetic field of ~75 kOe and a subsequent decrease with growing magnetic field (Fig. 5a). In this case, the $\Delta P(H)$ curve is smoother and broader while the maximum value of $\Delta P(H)$ is smaller than that for the composition with $x = 0.5$. For the $Gd_{0.3}Sr_{0.7}MnO_3$ composition with a higher Sr content, we also observed a bell-shaped $\Delta P(H)$ curve (Fig. 5b), but the value of the field-induced electric polarization was noticeably smaller and reached its maximum in a field of ~25 kOe. For both the aforementioned compositions, we observed a change of sign of electric polarization with the change of sign of the electric field in which the crystals were cooled. Hence, spontaneous electric polarization should also occur in these crystals. However, the polarization decreases rapidly with increasing *x*.

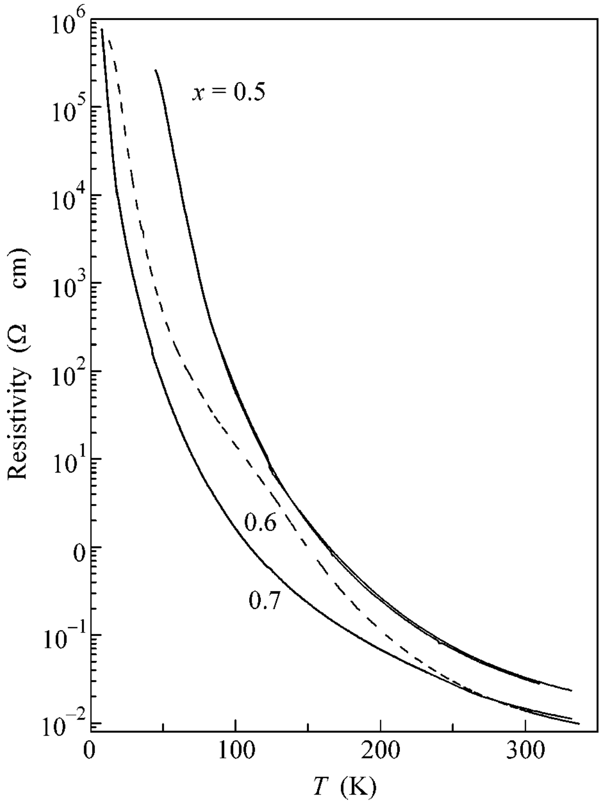

Fig. 1. Temperature dependence of resistivity for $Gd_{1-x}Sr_xMnO_3$ ($x = 0.5, 0.6, 0.7$) single crystals.

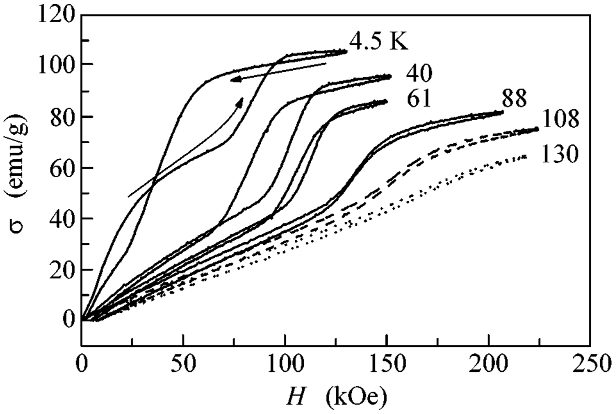

Fig. 2. Magnetization curves for $Gd_{0.5}Sr_{0.5}MnO_3$ at various temperatures.

The electric polarization observed in $Gd_{1-x}Sr_xMnO_3$ may be related to the presence of the new type of charge and orbital ordering predicted in [10]. Unlike the clas-

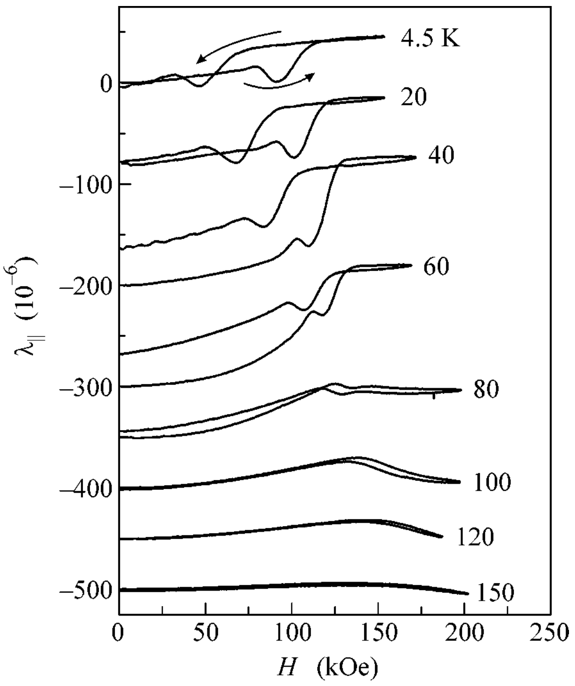

Fig. 3. Field dependences of magnetostriction measured along the growth axis of the $Gd_{0.5}Sr_{0.5}MnO_3$ single crystal. For clarity, the curves are shifted along the ordinate axis.

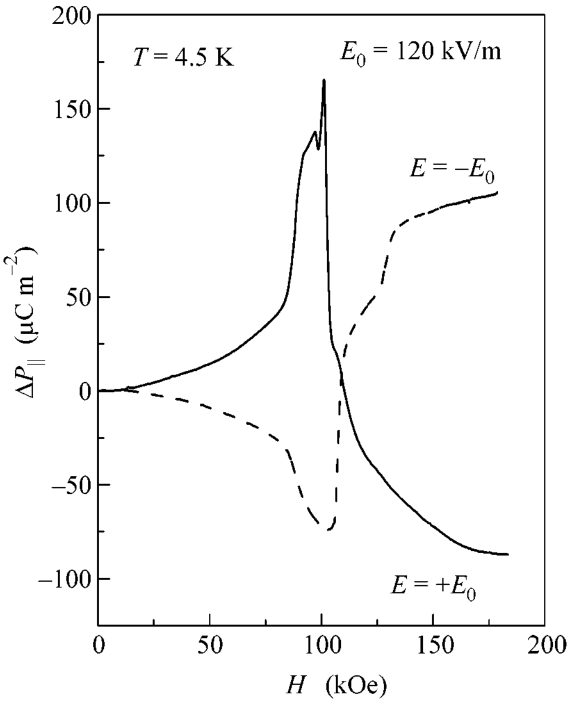

Fig. 4. Field dependences of polarization along the growth axis for the $Gd_{0.5}Sr_{0.5}MnO_3$ single crystal at $T = 4.5$ K. The measurements were performed after preliminary cooling in an electric field $E = \pm E_0$.

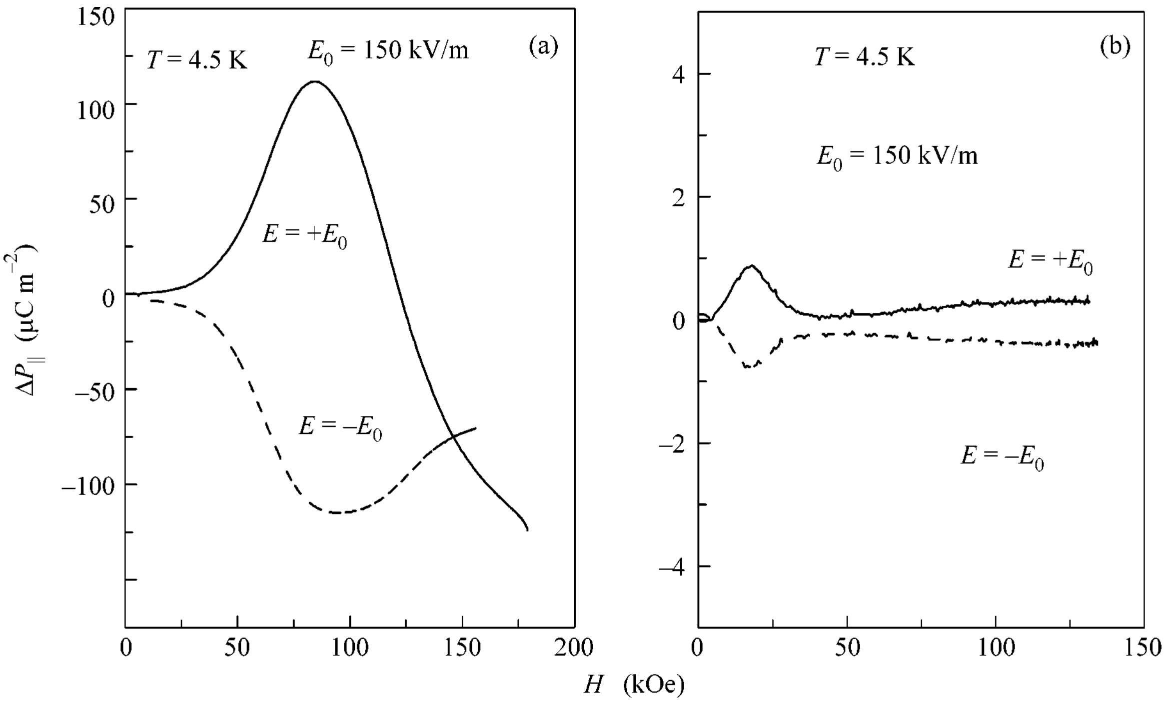

Fig. 5. Field dependences of polarization for the (a) $Gd_{0.4}Sr_{0.6}MnO_3$ and (b) $Gd_{0.3}Sr_{0.7}MnO_3$ single crystals at $T = 4.5$ K. The measurements were performed after preliminary cooling in an electric field $E = \pm E_0$.

sical CE-type structure with alternating Mn^{3+}/Mn^{4+} ions and e_g electrons localized by one of the manganese ions, the new type of ordering has e_g electrons asymmetrically distributed between neighboring ions. This structure consists of ordered manganese ion dimers and possesses a nonzero electric dipole moment. Although, in this model, the ground state of the spin system is the antiferromagnetic ordering, which does not correspond to the spin-glass cluster ground state of the $Gd_{1-x}Sr_xMnO_3$ ($x \sim 0.5$) system under study, we may expect that the basic features of the new type of charge-orbital ordering associated with nonzero polarization will be retained for $Gd_{1-x}Sr_xMnO_3$.

Thus, the studies described above revealed the presence of a spontaneous electric polarization in the $Gd_{1-x}Sr_xMnO_3$ system. The polarization manifests itself at the magnetic field-induced transition from the charge-ordered spin-glass state to the ferromagnetic conducting phase and may be caused by the presence of the new type of charge and orbital ordering predicted in [10].

We are grateful to D.I. Khomskiĭ for useful discussions. This work was supported by the Russian Foundation for Basic Research, project nos. 03-02-16445 and 04-02-81046-Bel2004.

REFERENCES

1. M. B. Salamon and M. Jaim, Rev. Mod. Phys. **73**, 583 (2001).
2. T. Kimura, T. Goto, H. Shintani, *et al.*, Nature **426**, 55 (2003).
3. T. Goto, T. Kimura, G. Lawes, *et al.*, Phys. Rev. Lett. **92**, 257201 (2004).
4. A. M. Kadomtseva, Yu. F. Popov, G. P. Vorob'ev, *et al.*, Pis'ma Zh. Éksp. Teor. Fiz. **81**, 22 (2005) [JETP Lett. **81**, 19 (2005)].
5. X. Hong, A. Posadas, A. Lin, and C. H. Ahn, Phys. Rev. B **68**, 134415 (2003).
6. A. Daoud-Aladine, J. Rodriguez-Carvajal, L. Pinsard-Gaudart, *et al.*, Phys. Rev. Lett. **89**, 97205 (2002).
7. V. Ferrari, M. Towler, and P. B. Littlewood, Phys. Rev. Lett. **91**, 227202 (2003).
8. G. Zheng and C. H. Patterson, Phys. Rev. B **67**, 220404 (2003).
9. V. S. Shakhmatov, N. M. Plakida, and N. S. Tonchev, Pis'ma Zh. Éksp. Teor. Fiz. **77**, 18 (2003) [JETP Lett. **77**, 15 (2003)].
10. D. V. Efremov, J. Van den Brink, and D. I. Khomskii, Nature Mater. **3**, 853 (2004); cond-mat/0306651 (2003).
11. B. Garsia-Landa, J. M. De Teresa, M. R. Ibarra, *et al.*, J. Appl. Phys. **83**, 7664 (1998).
12. T. Terai, T. Sasaki, T. Kakeshita, *et al.*, Phys. Rev. B **61**, 3488 (2000).

Translated by E. Golyamina

JETP Letters, Vol. 82, No. 9, 2005, pp. 594–598. Translated from Pis'ma v Zhurnal Éksperimental'noĭ i Teoreticheskoĭ Fiziki, Vol. 82, No. 9, 2005, pp. 672–677.
Original Russian Text Copyright © 2005 by Balagurov, Bobrikov, Pomyakushin, Sheptyakov, Babushkina, Gorbenko, Kartavtseva, Kaul'.

Magnetostructural Phase Separation and Giant Isotope Effect in $R_{0.5}Sr_{0.5}MnO_3$

A. M. Balagurov[a], I. A. Bobrikov[a], V. Yu. Pomyakushin[b], D. V. Sheptyakov[b], N. A. Babushkina[c], O. Yu. Gorbenko[d], M. S. Kartavtseva[d], and A. R. Kaul'[d]
[a] *Frank Laboratory of Neutron Physics, Joint Institute for Nuclear Research, Dubna, Moscow region, 141980 Russia*
e-mail: bala@nf.jinr.ru
[b] *Laboratory for Neutron Scattering, Paul Scherrer Institut, 5232 Villigen PSI, Switzerland*
[c] *Russian Research Centre Kurchatov Institute, Moscow, 123182 Russia*
[d] *Faculty of Chemistry, Moscow State University, Moscow, 119992 Russia*

Received September 26, 2005

Results of neutron diffraction studies of $R_{0.5}Sr_{0.5}MnO_3$ manganites (R = Sm, $Nd_{0.772}Tb_{0.228}$, and $Nd_{0.544}Tb_{0.456}$) performed to reveal the microscopic origins of the giant oxygen isotope effect recently discovered in $Sm_{0.5}Sr_{0.5}MnO_3$ are presented. It is shown that two crystalline phases differing in the type of Jahn–Teller distortions of oxygen octahedra and in the type of magnetic ordering coexist at low temperatures in all the studied compositions. A scenario for the observed phase transitions is suggested based on the diffraction data. It is found that the percolation transition from the metallic to insulating state in compositions with Sm upon substitution of ^{18}O for ^{16}O is associated with a sharp (from 65 to 13%) decrease in the volume of the ferromagnetic metallic phase. *© 2005 Pleiades Publishing, Inc.*

PACS numbers: 61.12.Ld, 75.30.–m

1. INTRODUCTION

The giant oxygen isotope effect in complex manganese oxides (manganites)—a change from the metallic to insulating state upon substitution of ^{18}O for ^{16}O—still remains one of the most intriguing phenomena in the physics of these compounds. The effect was first discovered in $(La_{0.5}Nd_{0.5})_{0.67}Ca_{0.33}MnO_3$ and $(La_{0.25}Pr_{0.75})_{0.7}Ca_{0.3}MnO_3$, that is, in compositions with the doping level $x \approx 0.3$, and more recently in $Sm_{1-x}Sr_xMnO_3$ at $x \approx 0.5$ as well (see [1] and references therein). Neutron diffraction studies of compositions with $x \approx 0.3$ clearly demonstrated [2] that an incoherent mixture of interpenetrating clusters with characteristic sizes of ~1000 Å of the ferromagnetic–metallic (FM–M) and antiferromagnetic (CE type)–insulating (AFM_{CE}–I) phases arises in these compounds upon decreasing the temperature. This creates conditions for the metal–insulator transition of a percolation nature. This type of the inhomogeneous state is new for solid-state physics, and it is necessary to look for mechanisms that ensure equilibrium of different phases and differ from the theory of ferrons [3], in which microscopic (~15–20 Å) sizes of inhomogeneities are controlled by the Coulomb energy, or from the model of elastic interactions of Jahn–Teller centers [4], which lead to coherently ordered inhomogeneous structures.

After the discovery of the giant isotope effect in the compositions $Sm_{1-x}Sr_xMnO_3$ (from here on, SSM) with $x = 0.45$ and 0.50 [1], studies of their phase diagram [5] and preliminary neutron diffraction experiments [6, 7] were performed to show that, at $x = 0.5$ in a sample enriched with the ^{16}O isotope, the FM and type-A AFM (AFM_A) phases coexist below 80 K. In addition, it was found in these works that the replacement of Sm by a mixture ($Nd_{1-y}Tb_y$) with the same ionic radius $\langle r_A\rangle = (1-y)r_{Nd} + yr_{Tb} = r_{Sm}$, where r_{Sm}, r_{Nd}, and r_{Tb} are ionic radii of samarium, neodymium, and terbium, respectively, does not change the type of the magnetic state. Therefore, $(Nd_{1-y}Tb_y)_{1-x}Sr_xMnO_3$ samples can be used for neutron structural analysis instead of SSM samples, for which the required accuracy cannot be achieved because of too strong absorption of neutrons by samarium.

This work presents the results of neutron experiments on the determination of the atomic and magnetic structure of $(Nd_{1-y}Tb_y)_{0.5}Sr_{0.5}MnO_3$ (from here on, NTSM) manganites with $y = 0.228$ (sample S1, $\langle r_A\rangle$ = 1.229 Å) and 0.456 (sample S2, $\langle r_A\rangle$ = 1.221 Å). The former is an analogue of the composition $(Nd_{0.5}Sm_{0.5})_{0.5}Sr_{0.5}MnO_3$, and the latter is an analogue of the composition $Sm_{0.5}Sr_{0.5}MnO_3$ with the same $\langle r_A\rangle$ and close macroscopic properties. It is shown that two symmetry-equivalent crystalline phases differing in macroscopic properties and in the type of magnetic ordering coexist in both compositions at low temperatures. Based on the results obtained, the diffraction data for SSM were revised, which allowed the structural origins of the giant isotope effect in these compounds to be formulated.

2. SAMPLES AND EXPERIMENT

Samples S1 and S2 (about 4 g) for neutron diffraction experiments were prepared by the so-called paper synthesis technique [1]. The ratio of Nd to Tb in NTSM was selected on the basis of data on ionic radii from Shannon's tables [8] for the ninefold coordination of the A cation accepted for manganites. The procedure of preparation of SSM compositions with ^{152}Sm, ^{16}O, and ^{18}O isotopes was described in [1, 5], and their mass was about 100 mg. Data obtained in the course of certification of samples, in particular, temperature dependences of the resistivity, magnetization, and magnetic susceptibility, were reported in [5, 9].

The crystal and magnetic structures of the samples were determined on HRFD (pulsed reactor IBR-2, Dubna, Russia), HRPT, and DMC (both with the SINQ source, PSI, Switzerland) neutron powder diffractometers. The first two are high-resolution diffractometers with $\Delta d/d \approx 0.001$, which allowed diffraction spectra from coexisting phases to be reliably distinguished and effects associated with peak broadening to be analyzed. The magnetic structure characteristics of the samples were determined on the DMC. The spectra were measured in a wide range of temperatures (10–300 K) mainly in the heating run. Moreover, the diffraction spectra from sample S1 were measured on the SLS source of synchrotron radiation (PSI, Switzerland) at several temperatures above and below the phase separation temperature.

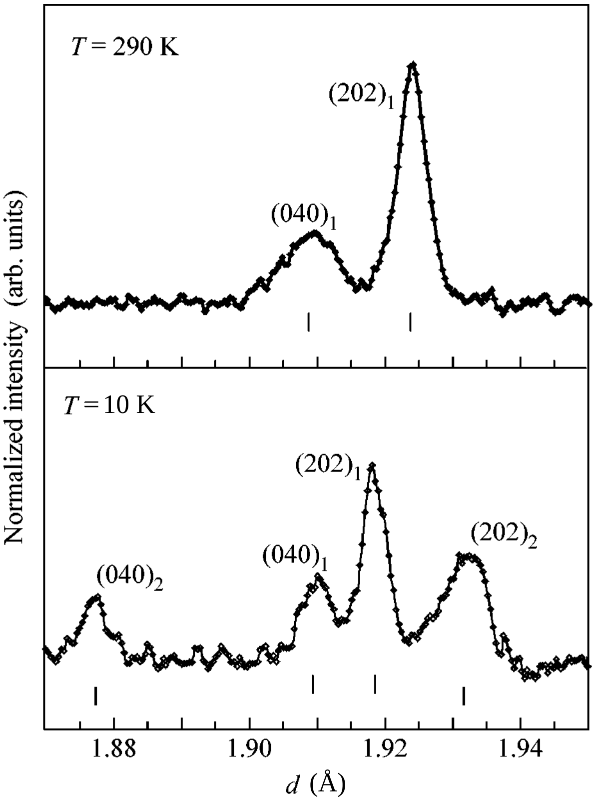

Fig. 1. Section of the diffraction spectrum of sample S1 at (above) room temperature and (below) T = 10 K. Miller indices and calculated peak positions are marked for $P1$ (only this phase exists at room temperature) and $P2$ phases.

3. STRUCTURAL SEPARATION IN NTSM

The atomic structures of NTSM and SSM at room temperature are well described in the rhombic space group *Pnma* with the relationship among the unit cell parameters standard for this group: $a \approx c \approx \sqrt{2}\,a_c \approx$ 5.4 Å, $b \approx 2a_c \approx$ 7.8 Å, where $a_c \approx$ 3.9 Å is the cell parameter of the cubic perovskite (phase $P1$ from here on). At low temperatures, peaks from one more rhombic phase (phase $P2$) appear in the diffraction spectra (Fig. 1). One of the features of this phase is a markedly smaller unit cell parameter b than that in the initial phase. The process of the appearance (upon cooling) or disappearance (upon heating) of phase $P2$ covers a considerable temperature range. For sample S1, it comprises almost 100 K. Upon heating above 150 K, the distinct diffraction peaks of phase $P2$ disappear, transforming to a wide intensity distribution with a flat top existing up to ≈250 K. The structural characteristics of phase $P1$ are rather reliably determined in the entire temperature range; for phase $P2$, it can be done only at $T \le 170$ K. The temperature dependences of unit cell parameters, interatomic Mn–O distances, and Mn–O–Mn valence angles for both phases in sample S1 were obtained upon treatment of spectra with HRFD and are shown in Fig. 2. In phase $P1$, the Mn–O distances in the MnO_6 octahedron only slightly differ from each other; even in the phase transition region, the parameter σ_{JT}, which characterizes the deviation of the MnO_6 octahedron from the regular shape (see, for example, [10]), does not exceed ≈0.01 Å at room temperature (for comparison, in $LaMnO_3$, $\sigma_{JT} \approx 0.1$ Å), and it decreases down to 0.007 Å at low temperature. In contrast, the octahedra in phase $P2$ are strongly distorted ($\sigma_{JT} \approx$ 0.03 Å), and the Mn–O1 bond directed along the axis b is the shortest one.

The volume occupied by the second phase weakly varies with temperature from 10 to 150 K and comprises about 40% of the sample volume. The diffraction peaks of phase $P2$ are appreciably broadened (by a factor of ≈1.7 wider than peaks $P1$) in the range from 10 to 150 K and sharply spread out above 150 K. The peak broadening can be due to an increased dispersion of the cell parameters of phase $P2$ caused by the occurrence of strains at phase boundaries ($\Delta a/a \approx 0.0035$) or by the finite sizes of coherently scattered domains ($L \approx 700$ Å at $T \le 150$ K and $L \approx 100$ Å at $190\text{ K} \le T \le 250$ K). Combining these two reasons is also possible, as well as

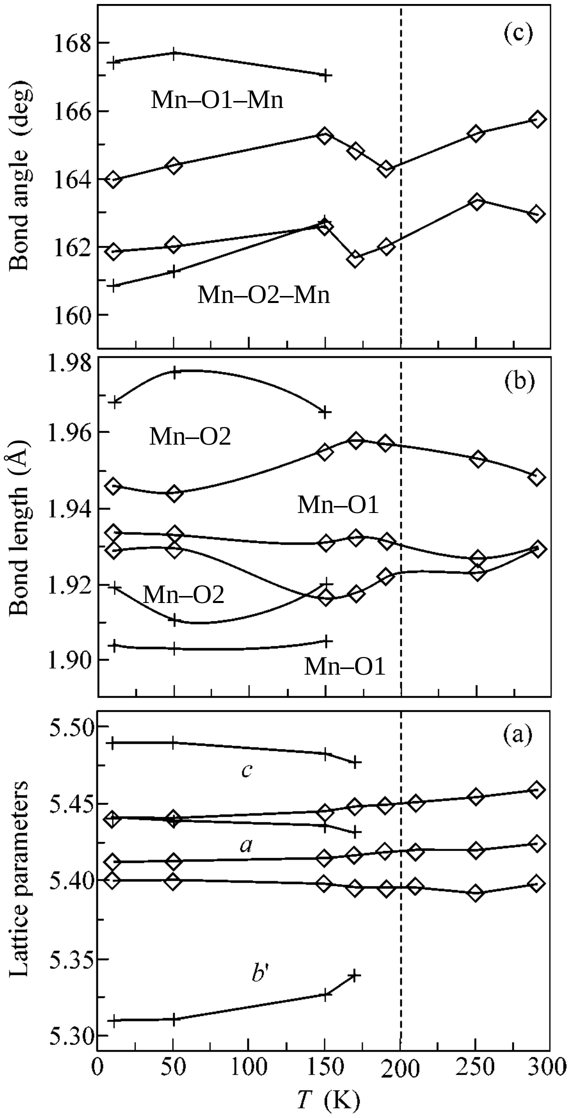

Fig. 2. Temperature dependences of (a) unit cell parameters ($b' = b/\sqrt{2}$), (b) Mn–O interatomic distances, and (c) Mn–O–Mn valence angles for (◇) *P*1 and (+) *P*2 phases in sample S1. The vertical dashed straight line designates the occurrence temperature of long-range FM and AFM_A orders. Signs of structural separation appear at 250 K, but the reliable determination of structural parameters of phase *P*2 can be performed only below 170 K. The experimental values shown in the figure were obtained on HRFD; the data from HRPT agree well with those values. Error bars of experimental points are less than the size of symbols for lattice parameters, about 0.002 Å for bond lengths, and about 0.1° for valence angles. Lines are drawn to facilitate perception.

strong fluctuations of the unit cell parameters of phase *P*2 over the sample volume.

The behavior of the sample with $y = 0.456$ is mainly the same. The facts that the second phase arises in this sample at a lower temperature (below 150 K) and that it occupies no more than 25% of the sample volume are essential distinctions.

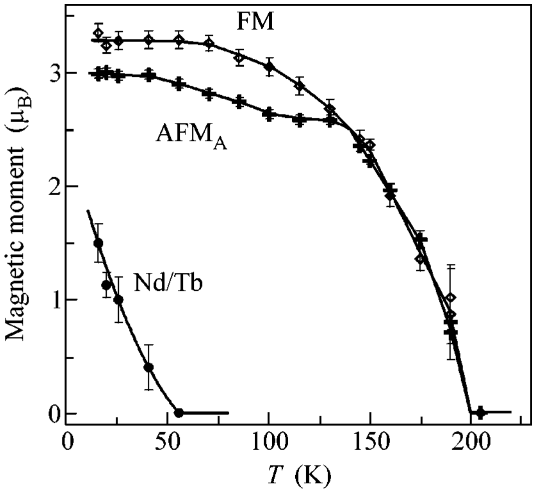

Fig. 3. Temperature dependences of the magnetic moments of Mn in the (+) FM and (◇) AFM_A phases, and (●) the magnetic moment (Nd/Tb) in the FM phase for sample S1 with $y = 0.228$. The values of moments are normalized to the phase concentration in the sample volume. Most experimental points were obtained on the DMC diffractometer. Points at 19, 150, and 190 K were additionally measured on HRPT.

4. MAGNETIC STRUCTURE OF NTSM

The data on magnetic susceptibility [5, 9] point to a transition to the FM state at temperatures $T_C \approx 200$ K and $T_C \approx 100$ K for samples S1 and S2, respectively. It follows from the neutron diffraction spectra measured in this work that, below these temperatures, FM ordering of magnetic moments of Mn appears in phase *P*1 and, in addition, the AFM_A structure arises in phase *P*2. Thus, below the indicated temperatures, structural separation is supplemented with magnetic separation, and the FM and AFM_A structures arise simultaneously. A characteristic decrease in FM intensities is observed below 50 K, which points to the ordering of magnetic moments (Nd/Tb) in the same direction as Mn moments. The temperature dependences of the magnetic contributions indicated above are shown in Fig. 3 for sample S1. It is evident that the FM and AFM_A structures arise synchronously and their temperature behavior is similar; that is, the volumes occupied by the corresponding phases in the sample remain approximately constant over the entire range, starting with T_C and to helium temperature. At $T = 10$ K, the magnetic moments in both phases are close to their limiting value 3.5 μ_B for the structure with the ratio $Mn^{3+}/Mn^{4+} = 1/1$, from which it follows that long-range magnetic order arises over virtually the entire sample volume. In both phases, magnetic moments are directed in parallel with the unit cell axis *c*.

5. PHASE SEPARATION IN $Sm_{0.5}Sr_{0.5}MnO_3$

Preliminary neutron data on the FM and AFM phases in $^{152}Sm_{0.5}Sr_{0.5}MnO_3$ with ^{16}O and ^{18}O oxygen isotopes [5] were obtained on a diffractometer with a medium resolution and from a small amount of the sample, which prevented the detection of two different crystalline phases in the sample. The treatment of the diffraction spectra from SSM in a two-phase version (by analogy with NTSM at $y = 0.456$, being an analogue of SSM) showed that two crystalline phases with approximately the same characteristics as in NTSM/S2 but with different relative concentrations coexist in both SSM samples with ^{16}O and ^{18}O isotopes. In the composition with ^{16}O having a metallic conductivity, phase $P1$ with almost regular oxygen octahedra occupies about 65% of the sample volume. The ordered moment in this phase assumes the limiting value ($M_{FM} = 3.5 \pm 0.2\ \mu_B$). The remaining part of the volume is occupied by the AFM_A phase with $M_{AFM} = 3.1 \pm 0.3\ \mu_B$. In the composition with ^{18}O, which is an insulator, the volume of phase $P1$ is only 13%, and long-range FM order is absent in this phase. As in NTSM/S2, in phase $P2$ in SSM below $T_c \approx 100$ K, the AFM_A structure arises with the ordered moment at low temperatures $M_{AFM} = 2.00 \pm 0.07\ \mu_B$.

6. DISCUSSION OF THE RESULTS

Structural and magnetic phase separation was already observed in manganites with compositions $R_{1-x}A_xMnO_3$, where R is a rare-earth element, A = Ca, Sr, etc. at $x \approx 0.5$ (see, for example, [11–13]). It was found that, as a rule, along with the FM phase with almost regular MnO_6 octahedra, the insulating AFM_{CE} phase arose with charge ordering (CO) of Mn^{3+} and Mn^{4+} ions and with diagonal ordering of $3x^2 - r^2$ and $3z^2 - r^2$ orbitals of Mn^{3+} ions in the (a, c) plane. The AFM_A structure observed in this work in NTSM and SSM occurs in manganites in undoped compositions of the $LaMn^{3+}O_3$ type, in which the $3x^2 - r^2$ and $3z^2 - r^2$ orbitals are ordered in the (a, c) plane in staggered rows. However, as shown in [14], the AFM_A structure can also arise in the compositions $R_{1-x}A_xMnO_3$ at $x = 0.5$, for example, for R = Pr and A = Sr, if charge ordering is combined with the filling of Mn^{3+} ($x^2 - y^2$) orbitals with an e_g electron. In both cases, the MnO_6 octahedron in the AFM_A structure is compressed along the b axis. It is this situation that is observed in phase $P2$ of our samples at low temperature.

As was noted in [1], the specific behavior of the inverse magnetic susceptibility $1/\chi'(T)$ of NTSM and SSM compositions at temperatures below 250 K suggest the occurrence of an inhomogeneous magnetic state in these systems even in the paramagnetic phase. It is suggested that this inhomogeneity is associated with strong AFM correlations accompanied by the occurrence of CO ($T_{CO} \approx 240$ K). However, it should be noted that, in spite of the theoretical prerequisites for the formation of CO [15], no clear microscopic evidence of its existence in the composition with $x \approx 0.5$ in the presence of the AFM_A-type structure has been found so far (see, for example, [16]). No additional peaks that can be related to the occurrence of the CO state are observed in the synchrotron radiation diffraction spectra measured in this work in sample S1. Thus, the question of the occurrence of CO in phase $P2$ of the NTSM and SSM compositions and the question of the specific type of orbital ordering requires further investigations. It should be noted that large fluctuations ($\sigma^2 = \langle r_A^2 \rangle - \langle r_A \rangle^2$) of the radius of the A cation (typical, in particular, for all $R_{0.5}Sr_{0.5}MnO_3$) can lead to the suppression of the transition to the CO state [17]. In contrast, it was reported that T_{CO} is virtually independent of these fluctuations at small σ^2 and/or large $\langle r_A \rangle$ [18].

The facts listed above fit the scenario proposed in [12], which suggests that phase separation of the sample into regions remaining paramagnetic and regions with strong AFM correlations and tendency for CO occurs with decreasing temperature even before the occurrence of long-range magnetic order. With a further decrease in temperature, the FM and AFM structures arise in these two types of regions, respectively. Only in this variant can the variations of magnetic peak intensities with decreasing temperature proceed synchronously without redistribution of phase volumes. The starting structure imperfection of the samples associated with local distortions of oxygen octahedra around Mn atoms occurring in different charge states and with fluctuations of the radius of the A cation can be a possible reason for phase separation. These fluctuations in $R_{1-x}Ca_xMnO_3$ are significantly larger than in $R_{1-x}Sr_xMnO_3$, because the difference between the radii of the ions R and Sr is larger than the difference between the radii of the ions R and Ca. These fluctuations primarily affect the local atomic displacements of oxygen atoms [19]. In the works based on numerical Monte Carlo simulations [20], it was shown that the scatter in the Mn–O–Mn valence angles leads to fluctuations of the hopping integral of the Mn e_g electron. With decreasing temperature, this can induce the occurrence of mesoscopic-size clusters of the metallic and insulating phases. From our diffraction data, it follows that, at the initial stage of cluster formation, structural changes become notable first; this occurs for both samples at approximately 50 K above T_c, and long-range order appear only when the sizes of the clusters become sufficiently large. The temperatures of the occurrence of structural separation in samples S1 and S2 (FM and AFM_A ordering) similarly decreased when y was increased from 0.228 to 0.456. This also suggests the same scenario of phase transitions in these compounds. The cause for the shift in T_c is evidently a change in $\langle r_A \rangle$. Actually, according to the phase diagram of compositions with $x = 0.5$ [21], a decrease of 0.01 Å in $\langle r_A \rangle$ at $\langle r_A \rangle \approx 1.23$ Å leads to a decrease of ≈100 K in T_{FM}.

New data on the coexistence of *P*1 and *P*2 phases in SSM samples with ^{16}O and ^{18}O isotopes allow the change from the metallic to insulating state upon substitution of ^{18}O for ^{16}O to be unambiguously interpreted as a percolation transition due to a sharp (from 65 to 13%) decrease in the volume of the metallic phase *P*1. In this regard, the isotopic M–I transitions in SSM and $(La_{0.25}Pr_{0.75})_{0.7}Ca_{0.3}MnO_3$ (LPCM) are similar: in both cases, these transitions can be related to the action of the polaron mechanism of the narrowing of the conduction band upon an increase in the oxygen mass [22]. A certain difference in the dependence of the occurrence temperatures T_C and T_N of long-range ferro- and antiferromagnetic orders on $\langle r_A \rangle$ in SSM and NTSM is possibly also associated with substantially different values of $\langle r_A \rangle$ fluctuations: $\sigma^2 \approx 0.0003$ Å^2 in LPCM, whereas $\sigma^2 \approx 0.0080$ Å^2 in NTSM, that is, almost 27 times larger.

7. CONCLUSIONS

In conclusion, let us formulate the main results. Neutron diffraction experiments performed on high-resolution diffractometers showed that, with decreasing temperature, $R_{0.5}Sr_{0.5}MnO_3$ compositions (R = Sm, $Nd_{0.772}Tb_{0.228}$, and $Nd_{0.544}Tb_{0.456}$) exhibit separation at the mesoscopic size scale into a phase with metallic conductivity, almost regular MnO_6 octahedra, and an FM structure and an insulating phase with strongly distorted MnO_6 octahedra and an AFM_A structure. The phase volumes remain approximately constant over the entire region of their coexistence. From the distribution of Mn–O distances by length, it follows that the AFM_A phase is orbital- and, possibly, charge-ordered, though we cannot find obvious indications of charge ordering. The success in the detailed structural analysis of the coexisting phases was favored by the unusually large difference in the parameters of their unit cells. The replacement of ^{16}O by ^{18}O in SSM samples leads to a decrease in the fraction of the sample volume occupied by the FM–M phase from ≈65% to ≈13% and, as a consequence, to a percolation transition from the metallic to insulating state, that is, to the giant isotope effect.

We are grateful to V.G. Simkin for great help in performing neutron experiments on HRFD. This work was supported by the Russian Foundation for Basic Research, project nos. 03-02-16954 and 04-02-16991. Neutron experiments were performed on the pulsed reactor IBR-2 (JINR, Dubna) and on the neutron source SINQ (Paul Scherrer Institut, Villigen, Switzerland).

REFERENCES

1. N. A. Babushkina, E. A. Chistotina, O. Yu. Gorbenko, *et al.*, Phys. Rev. B **67**, 100410 (2003).
2. A. M. Balagurov, V. Yu. Pomjakushin, D. V. Sheptyakov, *et al.*, Phys. Rev. B **64**, 024420 (2001).
3. É. L. Nagaev, Usp. Fiz. Nauk **165**, 529 (1995) [Phys. Usp. **38**, 497 (1995)].
4. D. I. Khomskii and K. I. Kugel, Phys. Rev. B **67**, 134401 (2003).
5. N. A. Babushkina, E. A. Chistotina, I. A. Bobrikov, *et al.*, J. Phys.: Condens. Matter **17**, 1975 (2005).
6. A. I. Kurbakov, V. A. Trunov, A. M. Balagurov, *et al.*, Fiz. Tverd. Tela (St. Petersburg) **46**, 1650 (2004) [Phys. Solid State **46**, 1704 (2004)].
7. N. A. Babushkina, E. A. Chistotina, O. Yu. Gorbenko, *et al.*, Fiz. Tverd. Tela (St. Petersburg) **46**, 1821 (2004) [Phys. Solid State **46**, 1884 (2004)].
8. R. D. Shannon, Acta Crystallogr. A **32**, 751 (1976).
9. N. A. Babushkina, E. A. Chistotina, A. M. Balagurov, *et al.*, submitted to J. Magn. Magn. Mater.
10. P. G. Radaelli, G. Iannone, M. Marezio, *et al.*, Phys. Rev. B **56**, 8265 (1997).
11. Q. Huang, J. W. Lynn, R. W. Erwin, *et al.*, Phys. Rev. B **61**, 8895 (2000).
12. A. Machida, Y. Moritomo, E. Nishibori, *et al.*, Phys. Rev. B **62**, 3883 (2000).
13. C. Ritter, R. Mahendiran, M. R. Ibarra, *et al.*, Phys. Rev. B **61**, R9229 (2000).
14. T. Mizokawa and A. Fujimori, Phys. Rev. B **56**, R493 (1997).
15. J. van den Brink and D. Khomskii, Phys. Rev. Lett. **82**, 1016 (1999).
16. A. Machida, Y. Moritomo, K. Ohoyama, *et al.*, Phys. Rev. B **62**, 80 (2000).
17. Y. Q. Wang, I. Maclaren, X. F. Duan, *et al.*, J. Appl. Phys. **90**, 488 (2001).
18. P. V. Vanitha, P. N. Santhosh, R. S. Singh, *et al.*, Phys. Rev. B **59**, 13 539 (1999).
19. L. M. Rodriguez-Martinez and J. P. Attfield, Phys. Rev. B **58**, 2426 (1998).
20. E. Dagotto, J. Burgy, and A. Moreo, Solid State Commun. **126**, 9 (2003).
21. P. M. Woodward, T. Vogt, D. E. Cox, *et al.*, Chem. Mater. **10**, 3652 (1998).
22. G. M. Zhao, K. Conder, H. Keller, and K. A. Muller, Nature **381**, 676 (1996).

Translated by A. Bagatur'yants

JETP Letters, Vol. 82, No. 9, 2005, pp. 599–602. From Pis'ma v Zhurnal Éksperimental'noĭ i Teoreticheskoĭ Fiziki, Vol. 82, No. 9, 2005, pp. 678–681.

Surface-Plasmon Vortices in Nanostructured Metallic Films¶

A. A. Ezhov*, S. A. Magnitskii, N. S. Maslova, D. A. Muzychenko,
A. A. Nikulin, and V. I. Panov

Department of Physics, Moscow State University, Moscow, 119992 Russia
**e-mail: spm@spmlab.phys.msu.su*

Received August 29, 2005; in final form, September 27, 2005

Light scattering by a small protrusion on a metal surface is analyzed within the framework of perturbation theory. Upon normal incidence of a linearly polarized monochromatic wave, slight deviations of the protrusion's shape from a circularly symmetric one lead to the formation of optical vortices in the near-field region due to resonant excitation of circular surface plasmons. This agrees with the results of scanning near-field optical microscopy experiments revealing distinct spiral patterns in the in-plane near-field intensity distribution for metallized nanostructured polymer substrates. © *2005 Pleiades Publishing, Inc.*

PACS numbers: 74.50.+r, 74.80.Fp

In the past decade, phase singularities of optical wave fields have attracted considerable interest in both fundamental and applied aspects. There are numerous techniques to produce an optical field with a screw dislocation (optical vortex) [1, 2]. Optical vortices produced by phase steps—refracting or reflecting surface structures shaped into one turn of a helicoid—can be understood in terms of the Berry phase and, in essential respects, are analogous to the Aharonov–Bohm effect. Phase singularities can play a significant role in the interaction of light with solid-state structures being developed for modern nanophotonic applications.

Introducing scanning near-field optical microscopy (SNOM) [3] as an experimental method has phase singularities to be investigated with a subwavelength resolution. Phase singularities of optical fields in waveguide structures [4] and in the focal region of a lens [5] have been observed by means of interferometric SNOM.

Recently, distinct spiral patterns in the in-plane near-field fringes [6] have been detected by SNOM measurements of the three-dimensional distribution of the field intensity near nanocylinders irradiated by linearly polarized monochromatic light incident normally to the axes of the nanocylinders. A constant wave laser beam with a wavelength of 532 nm was additionally polarized by a Nicole prism with an extinction ratio of 5×10^{-5} at the most. The nanocylinders were manufactured by double replication from a silicon matrix and placed onto a polymer substrate. Some of the nanocylinders were covered by a gold–palladium layer 20 to 30 nm thick; coverage nonuniformity due to the shadow effect was prevented by the coating procedure. According to Fig. 1, unexpected interference patterns with a spiral symmetry were observed only for metallized samples, whereas, for bare (nonmetallized) ones, the patterns were circular.

These experimental results can be understood on a qualitative level by considering a model that admits the use of a simplified perturbation-theory procedure as

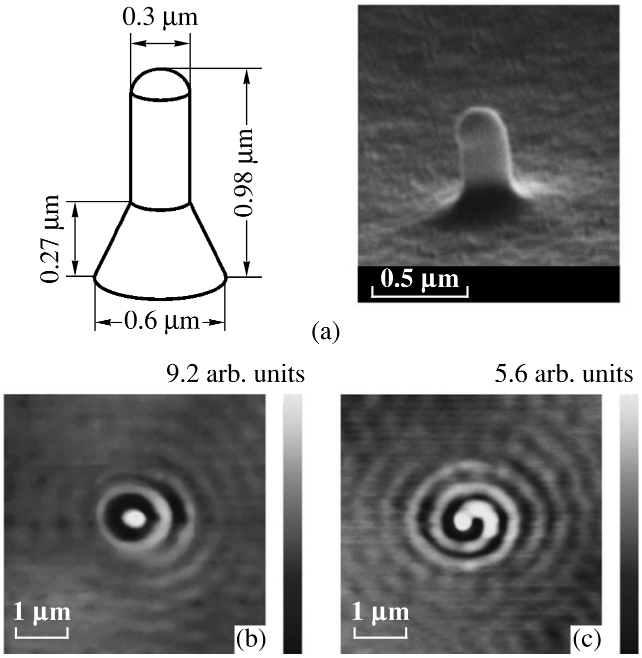

Fig. 1. (a) Geometric parameters and scanning electronic microscope image of a polymer nanocylinder; (b) SNOM image of the near-field intensity distribution near a bare polymer nanocylinder; and (c) that coated by a 25-nm-thick gold–palladium layer measured at a height of 20 nm above the cylinder tops upon normal incidence of linearly polarized light with a wavelength of 532 nm.

¶ The text was submitted by the authors in English.

compared to those developed in the context of a more general approach [7, 8]. A linearly polarized plane wave with frequency ω is incident from vacuum at a normal to the boundary of a semi-infinite metal occupying the half-space $z < Z(\rho, \varphi)$, where ρ, φ, z are the cylindrical coordinates and the function $Z(\rho, \varphi)$ describes a nearly flat surface having a single protrusion with height L and radius R:

$$Z(\rho, \varphi) = Lf(\rho/R)[1 + \gamma g(\varphi)], \tag{1}$$

where the function $f(x)$ satisfies the conditions

$$f(x < 1) > 0, \quad f(x \geq 1) \equiv 0 \tag{2}$$

and the term $\gamma g(\varphi)$ describes deviations of the protrusion's shape from a circularly symmetric one. Taking these circular-symmetry shape distortions into account is of primary importance for the model, since another factor breaking the symmetry between clockwise and counterclockwise directions—the presence of a circularly polarized component in the incident radiation—is excluded by the experimental procedure. The surface defect is assumed to be (i) slightly sloping, (ii) small in comparison to the wave penetration depth in the metal, and (iii) having small circular-symmetry distortions, i.e.,

$$L \ll R \ll \frac{c}{\omega\sqrt{|\varepsilon|}}, \quad \gamma \ll 1 \tag{3}$$

with ε being the dielectric constant of the metal. We suppose that $-\mathrm{Re}\,\varepsilon(\omega) \gg 1$ and simplify the boundary-value problem of finding the scattered electromagnetic field outside the metal by the use of the impedance boundary conditions at $z = Z(\rho, \varphi)$:

$$\mathbf{E}_t = \zeta[\mathbf{H}_t\ \mathbf{n}], \tag{4}$$

where $\mathbf{E}$ and $\mathbf{H}$ are the electric and magnetic fields at frequency ω, respectively, $\zeta = \sqrt{1/\varepsilon}$ is the surface impedance of the metal, $\mathbf{n}$ is the unit vector normal to the surface and directed inward into the metal, and the subscript t denotes the value of the tangential vector component taken at $z = Z(\rho, \varphi)$. In the case of a perfectly flat boundary $z = 0$, the approximate boundary conditions (4) yield the following relation between the wavenumber q and frequency Ω of a surface plasmon wave propagating along the plane $z = 0$ (the inverse function determines the dispersion law):

$$q = \frac{\Omega}{c}\sqrt{1 + \zeta(\Omega)^2}, \quad |\zeta| \ll 1. \tag{5}$$

This result reproduces the exact relation $q = \Omega/c\sqrt{1 - \zeta(\Omega)^2}$ to the second order in ζ inclusive.

It is convenient to represent the total field $\mathbf{F}$ at $z \geq Z(\rho, \varphi)$ as a sum of four terms (here, $\mathbf{F}$ stands for either $\mathbf{E}$ or $\mathbf{H}$):

$$\mathbf{F} = \mathbf{F}_0 e^{-ikz} + \bar{\mathbf{F}} e^{ikz} + \mathbf{F}^{(s)}(\rho, \varphi) e^{-\kappa_s z} + \tilde{\mathbf{F}}(\rho, \varphi, z), \tag{6}$$

where $\kappa_s = \sqrt{q_s^2 - k^2}$, $k = \omega/c$, q_s is the wavevector modulus of the surface-plasmon wave at frequency ω (i.e., q_s is the root of the equation $\Omega(q_s) = \omega$ with $\Omega(q)$ being the function inverse to that given by Eq. (5)). The vector $\mathbf{F}_0$ is the field amplitude in the incident wave, $\bar{\mathbf{E}} = (\zeta - 1)/(1 + \zeta)\mathbf{E}_0$, $\bar{\mathbf{H}} = -(\zeta - 1)/(1 + \zeta)\mathbf{H}_0$, $\mathbf{F}^{(s)}$ and $\tilde{\mathbf{F}}$ are the functions to be found. The first two terms in Eq. (6) correspond to a superposition of the incident wave and that reflected from the flat boundary $z = 0$. The third term in Eq. (6) stems from resonant excitation of surface plasmons. The far-field contribution to the field scattered by the protrusion is included in the remainder term $\tilde{\mathbf{F}}$.

We assume that, at the boundary, the field $\tilde{\mathbf{F}}$ is negligible against the background of the surface-plasmon term in the following sense:

$$|\tilde{\mathbf{F}}|_{z = Z(\rho, \varphi)} \ll |\mathbf{F}^{(s)}|, \quad \left|\frac{\partial \tilde{\mathbf{F}}}{\partial z}\right|_{z = Z(\rho, \varphi)} \ll \kappa_s |\mathbf{F}^{(s)}|. \tag{7}$$

It will be shown that the procedure of finding $\mathbf{F}^{(s)}$ based on condition (7) is self-consistent; i.e., it guarantees their fulfillment. The field $\mathbf{F}^{(s)}(\rho, \varphi)$ can be expanded in a Fourier series:

$$\mathbf{F}^{(s)}(\rho, \varphi) = \sum_n \mathbf{F}_n(\rho) e^{in\varphi}. \tag{8}$$

Four of the six vector components of $\mathbf{E}_n(\rho)$ and $\mathbf{H}_n(\rho)$ can be explicitly expressed from the Maxwell equations through the remaining two, $E_{z,n}(\rho) \equiv E_n(\rho)$ and $H_{z,n}(\rho) \equiv H_n(\rho)$.

At $\rho > R$, the functions $E_n(\rho)$ and $H_n(\rho)$ correspond to the normal field components in a traveling (diverging) circular surface-plasmon wave with the wavenumber q_s. Hence,

$$E_n(\rho > R) = C_n H_{|n|}^{(1)}(q_s \rho), \tag{9}$$

$$H_n(\rho > R) \equiv 0, \tag{10}$$

where $H_{|n|}^{(1)}(x)$ is the Hankel function of the first kind and C_n is a constant. Thus, the problem reduces to finding the functions $E_n(\rho)$ and $H_n(\rho)$ within the interval $0 \leq \rho \leq R$. At $\rho = R$, they should be combined with the functions given by Eq. (9) to provide continuity of all field components. The function $g(\varphi)$ in Eq. (1) can be expanded in a Fourier series: $g(\varphi) = \sum_{n \neq 0} g_n e^{in\varphi}$ with $g_{-n} = g_n^*$. We approximate the exponential factors in Eq. (6) at $z = Z(\rho, \varphi)$ by the two lowest order terms in their Taylor series expansions at $z = 0$, $e^{\pm ikZ(\rho, \varphi)} \approx 1 \pm ikZ(\rho, \varphi)$, and limit ourselves to the first order in the small parameter kL. In this way, the boundary conditions (4) are mapped onto the plane $z = 0$. To within the chosen accuracy, we find that $E_{n \neq \pm 1} = H_{n \neq \pm 1} \equiv 0$; meanwhile, $E_{n=\pm1}$ and $H_{n=\pm1}$ satisfy the following set of equations (where the prime denotes the first derivative of a function and $\xi \equiv \rho/R$):

$$\begin{aligned} &n[-H_n(\xi) + 2\gamma_n\alpha(\xi)H_{-n}(\xi)] \\ &+ \xi\alpha'(\xi)[E_n(\xi) + \gamma_n E_{-n}(\xi)] = is(\xi), \end{aligned} \tag{11}$$

$$\begin{aligned} &i\xi H'_n(\xi) + \xi\alpha'(\xi)[H_n(\xi) + \gamma_n H_{-n}(\xi)] \\ &\quad - 2n\gamma_n\alpha(\xi)E_{-n} = -ns(\xi), \\ &\qquad n = \pm1, \quad 0 \le \xi \le 1, \end{aligned} \tag{12}$$

with $\gamma_1 = \gamma_{-1}^* = \gamma g_2$, $\alpha(\xi) = kLf(\xi)$, and $s(\xi) = k^2RL(1 - \zeta)E_0\xi f(\xi)$. The main feature of this equation set is breaking of symmetry between the terms with $n = 1$ and those with $n = -1$. Analysis of the relative magnitude of the coefficients in Eqs. (11) and (12) shows that $|E_n(\rho < R)| \gg |H_n(\rho < R)|$. Taking this into account, we neglect $H_n(\rho < R)$ to provide continuity of the field components at $\rho = R$. At $\xi \longrightarrow 0$, it follows from Eqs. (11) and (12) that $E_n(\xi) \propto \xi$. At $\xi \approx 1$ and $f(\xi) = 1 - \xi$, Eqs. (11) and (12) yield the following approximate expressions for $E_{\pm1}$:

$$\begin{aligned} E_{\pm1}(\eta) &\approx A_{\pm1}e^{\gamma|g_2|\eta^2/2} + B_{\pm1}e^{-\gamma|g_2|\eta^2/2} \\ &+ kR(1-\zeta)(i\eta + 2\gamma_{\pm1}\eta^3), \end{aligned} \tag{13}$$

where $\eta \equiv 1 - \xi \ll 1$ and the constants $A_{\pm1}$ and $B_{\pm1}$ are to be found simultaneously with $C_{\pm1}$ entering into Eq. (9). We extrapolate the expressions given by Eq. (13) to the whole interval $0 \le \xi \le 1$ with the extra boundary condition $E_{\pm1}(\xi = 0) = 0$. The latter, together with the sewing conditions at $\xi = 1$, provides equations for determining the constants $A_{\pm1}$, $B_{\pm1}$, and $C_{\pm1}$. As a result, we obtain

$$A_{\pm1} = \frac{1}{2}\left(\frac{q_sRh'}{\gamma|g_2|} + h\right)C_{\pm1}, \tag{14}$$

$$B_{\pm1} = \frac{1}{2}\left(-\frac{q_sRh'}{\gamma|g_2|} + h\right)C_{\pm1}, \tag{15}$$

$$C_{\pm1} = \frac{kR(\zeta-1)\left(\frac{3}{2}\gamma_{\pm1} + i\right)E_0}{q_sRh'\sinh\frac{\gamma|g_2|}{2} + h\cosh\frac{\gamma|g_2|}{2}}, \tag{16}$$

where

$$h = H_1^{(1)}(q_sR), \quad h' = \frac{1}{2}(H_0^{(1)}(q_sR) - H_2^{(1)}(q_sR)).$$

Finally, we should check that the obtained solutions are consistent with the initial assumptions given by inequalities (7). Since the sum $E_z^{(s)}(\rho, \varphi)e^{-\kappa_s z} + \tilde{E}_z(\rho, \varphi, z)$ from Eq. (6) satisfies the three-dimensional Helmholtz equation with the wavevector modulus ω/c, the function $\tilde{E}_z(\rho, \varphi, z)$, to within the chosen accuracy, has the integral form

$$\tilde{E}_z(\mathbf{r}) = \int\limits_{\substack{\rho' < R \\ z' > Z(\rho, \varphi)}} G(|\mathbf{r} - \mathbf{r}'|)(\Delta_{\rho', \varphi'} + q_s^2)E_z^{(s)}(\mathbf{r}')d^3r', \tag{17}$$

where

$$G(r) = \frac{\exp(ikr)}{4\pi r}, \quad \Delta_{\rho,\varphi} = \frac{1}{\rho}\frac{\partial}{\partial\rho}\left(\rho\frac{\partial}{\partial\rho}\right) + \frac{1}{\rho^2}\frac{\partial^2}{\partial\varphi^2}$$

and $E_z^{(s)}(\mathbf{r}) = E_z^{(s)}(\rho, \varphi)e^{-\kappa_s z}$. From Eq. (17), the following estimates can be obtained:

$$\left|\frac{\tilde{E}_z|_{z = Z(\rho, \varphi)}}{E_z^{(s)}}\right| \sim (kR)^2 \ll 1, \tag{18}$$

$$\left|\frac{\left.\frac{\partial\tilde{E}_z}{\partial z}\right|_{z = Z(\rho, \varphi)}}{\kappa_s E_z^{(s)}}\right| \sim \sqrt{|\varepsilon|}(kR)^2 \ll 1, \tag{19}$$

which leads to inequalities (7).

Analyzing the spatial behavior of the nonvanishing time-averaged characteristics of the scattered field, we conclude that, for the found solution, a first-order vortex occurs in the in-plane distribution of the tangential component of the time-averaged Poynting vector $\mathbf{S} = \frac{c}{8\pi}\mathrm{Re}[\mathbf{E}\ \mathbf{H}^*]$ taken at the metal boundary $z = Z(\rho, \varphi)$. The projection of $\mathbf{S}$ onto the plane $z = 0$ describes the energy flow in the traveling surface-plasmon wave resonantly excited by the incident light due to the presence of the surface defect. This component exponentially decays as $|z|$ grows, and it is absent in the absence of the surface plasmon, e.g., for a dielectric substrate with $\mathrm{Re}\,\varepsilon > 0$. For our model, we obtain

$$|S_x^{(s)}| \gg |S_y^{(s)}|, \tag{20}$$

$$\begin{aligned} S_x^{(s)} &= \frac{ce^{-\kappa_s z}}{4\pi}\mathrm{Re}(E_z^{(s)}(\rho, \varphi)E_0^*) \\ &\propto e^{-\kappa_s z}\mathrm{Re}\{H_1^{(1)}(q_sR)(\sin\varphi + \gamma\,\mathrm{Im}\,g_2e^{i\varphi})\}, \end{aligned} \tag{21}$$

where the x axis is chosen to be parallel to the electric field $\mathbf{E}_0$ in the incident plane wave. Figure 2 shows the first-order vortex occurring in the in-plane spatial dependence of $S_x^{(s)}(\rho, \varphi, z = Z(\rho, \varphi))$ at $\gamma \ne 0$, i.e., when the defect shape deviates from circular symmetry.

To summarize, the scattering of linearly polarized monochromatic light by an individual subwavelength protrusion in a thin metal film has been studied within

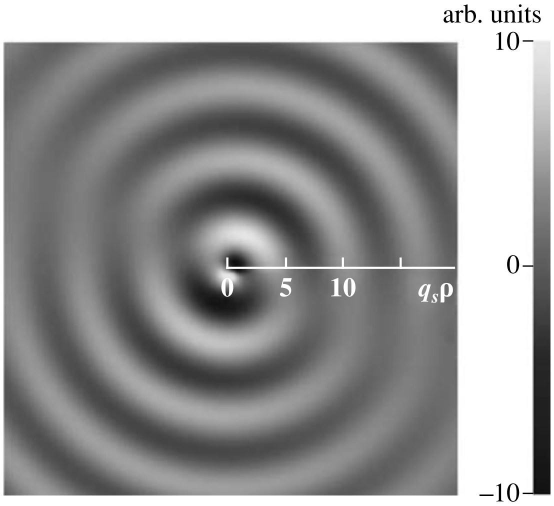

Fig. 2. Density plot of the tangential Poynting vector component $S_x^{(s)}$ at the metal surface as a function of the dimensionless radius $q_s\rho$ and polar angle $\varphi(\gamma = 0.5, g_2 = i)$.

the framework of perturbation theory. It is shown that, even at normal incidence, small deviations from circular symmetry of the protrusion shape can result in optical vortex formation in the near-field region if resonant circular surface-plasmon waves are excited. This coincides with the fact that the in-plane near-field intensity distribution measured by scanning near-field optical microscopy has distinct spiral patterns for metallized nanostructured polymer substrates contrary to the circular patterns observed for unmetallized substrates where surface-plasmon waves are lacking.

This work was supported in part by the Russian Foundation for Basic Research (project nos. 03-02-16807, 04-02-16847, and 04-02-17059). Support from the Samsung Corporation is also gratefully acknowledged.

REFERENCES

1. M. V. Berry and J. F. Nye, Proc. R. Soc. London **35**, 8723 (1987).
2. E. Engel, N. Huse, T. A. Klar, and S. W. Hell, Appl. Phys. B **77**, 11 (2003).
3. D. W. Pohl, W. Denk, and M. Lanz, Appl. Phys. Lett. **44**, 651 (1984).
4. M. L. M. Balistreri, J. P. Korterik, L. Kuipers, and N. F. van Hulst, Phys. Rev. Lett. **85**, 294 (2000).
5. J. N. Walford, K. A. Nugent, A. Roberts, and R. E. Scholten, Opt. Lett. **27**, 345 (2002).
6. M. V. Bashevoy, A. A. Ezhov, S. A. Magnitskii, *et al.*, Int. J. Nanosci. **3**, 105 (2004).
7. P. I. Arseev, Pis'ma Zh. Éksp. Teor. Fiz. **45**, 132 (1987) [JETP Lett. **45**, 163 (1987)].
8. P. I. Arseev, Zh. Éksp. Teor. Fiz. **92**, 464 (1987) [Sov. Phys. JETP **65**, 262 (1987)].

JETP Letters, Vol. 82, No. 9, 2005, pp. 603–608. From Pis'ma v Zhurnal Éksperimental'noĭ i Teoreticheskoĭ Fiziki, Vol. 82, No. 9, 2005, pp. 682–687.
Original English Text Copyright © 2005 by Gavriliuk, Struzhkin, Lyubutin, Trojan.

Irreversible Electronic Transition with Possible Metallization in $Y_3Fe_5O_{12}$ at High Pressure[¶]

A. G. Gavriliuk[a, b, c], V. V. Struzhkin[a], I. S. Lyubutin[c], and I. A. Trojan[b]
[a] *Geophysical Laboratory, Carnegie Institution of Washington, 5251 Broad Branch Road NW,*
Washington, DC 20015, USA
[b] *Institute for High Pressure Physics, Russian Academy of Sciences, Troitsk, Moscow region, 142190 Russia*
[c] *Institute of Crystallography, Russian Academy of Sciences, Moscow, 119333 Russia*
e-mail: lyubutin@ns.crys.ras.ru

Received September 27, 2005

The effect of high pressure up to 70 GPa on the optical absorption spectra in yttrium iron garnet $Y_3Fe_5O_{12}$ single crystals was studied in diamond anvil cells. In the pressure range 40–50 GPa, an electronic transition with a drastic narrowing in the optical gap from ~2.3 eV to nearly zero was observed, implying possible metallization. The final narrowing of the optical gap to zero is extrapolated at about 55 GPa. It is shown that the phase transition in yttrium iron garnet observed at 40–55 GPa is possibly a transition of the insulator–metal type. At decompression, the backtransition to the insulating state is not completely reversible. The final spectrum at ambient pressure is substantially different from the initial one and corresponds to an optical gap of about 1.8 eV, while, in the initial state, the gap value is ~2.6 eV. © *2005 Pleiades Publishing, Inc.*

PACS numbers: 64.60.–i, 71.30.+h, 78.20.–e, 81.40.Tv

INTRODUCTION

Yttrium iron garnet $Y_3Fe_5O_{12}$ (YIG) belongs to a well-known class of rare-earth iron garnets which are ferrimagnets with a dominant antiferromagnetic interaction [1–3]. It has a cubic structure with space group O_h^{10}–$Ia3d$, and the unit cell parameter is $a_0 = 12.3738$ Å [4]. Iron ions Fe^{3+} occupy two different sites, with octahedral and tetrahedral oxygen environments in the ratio 2 : 3 per formula unit, and thus build two magnetic iron sublattices with opposite directions of magnetization. Two Fe^{3+} ions from the octahedral sublattice partially compensate magnetization of three Fe^{3+} ions from tetrahedral sublattice giving $5\mu_B$ of final magnetization per formula unit [1]. At ambient pressure, the Neel temperature of YIG is about 555 K.

YIG is a charge-transfer insulator with optical gap of about ~2.6 eV [5]. There are several *d*–*d* optical transitions in the region of transparency [5, 6]. The nature of the absorption edge is charge-transfer transitions between electronic shells of Fe^{3+} ions and ligands O^{2-} [5]. It was also shown in [6] that the valence of iron ions can be altered by heat treatment in oxidizing or reducing atmospheres or by doping with divalent or tetravalent ions, which leads to an increase in optical absorption and electrical conductivity.

In the present study, external high pressures created in diamond anvil cells were applied to the $Y_3Fe_5O_{12}$ single crystal to modify its electronic properties. Measurements of optical absorption were used to investigate the parameters of the electronic system.

EXPERIMENTAL

A high-quality $Y_3Fe_5O_{12}$ single-crystal film with thickness ~7.5 μm was grown on the $Gd_3Ga_5O_{12}$ garnet substrate with the (111) direction perpendicular to the substrate and was then cleaved from the substrate. In an optical microscope, the crystal plate of YIG was transparent and had a deep red-brown color. A YIG plate with the dimensions $\sim 60 \times 40\ \mu m^2$ was placed in a high-pressure cell with diamond anvils. The diameter of the working surface of diamonds in the cell was about 390 μm, and the diameter of the hole in the rhenium gasket where the sample was placed was about 120 μm. Silicon-organic liquid PES-5 was used as a pressure medium. The pressure was determined by the standard ruby fluorescence technique. Several ruby chips with dimensions 1–5 μm were placed in the cell at different distances from the center of the hole in order to evaluate the pressure distribution.

The optical absorption in the near- and middle-IR region was measured with the help of a Magna-IR750 Fourier spectrometer made by the Nicolet Company, with the spectral resolution 32 cm^{-1}. A liquid-nitrogen-cooled mercury cadmium telluride (MCT) detector was used. Measurements in the visible and near-UV regions were made with an optical system equipped with a

---

[¶] The text was submitted by the authors in English.

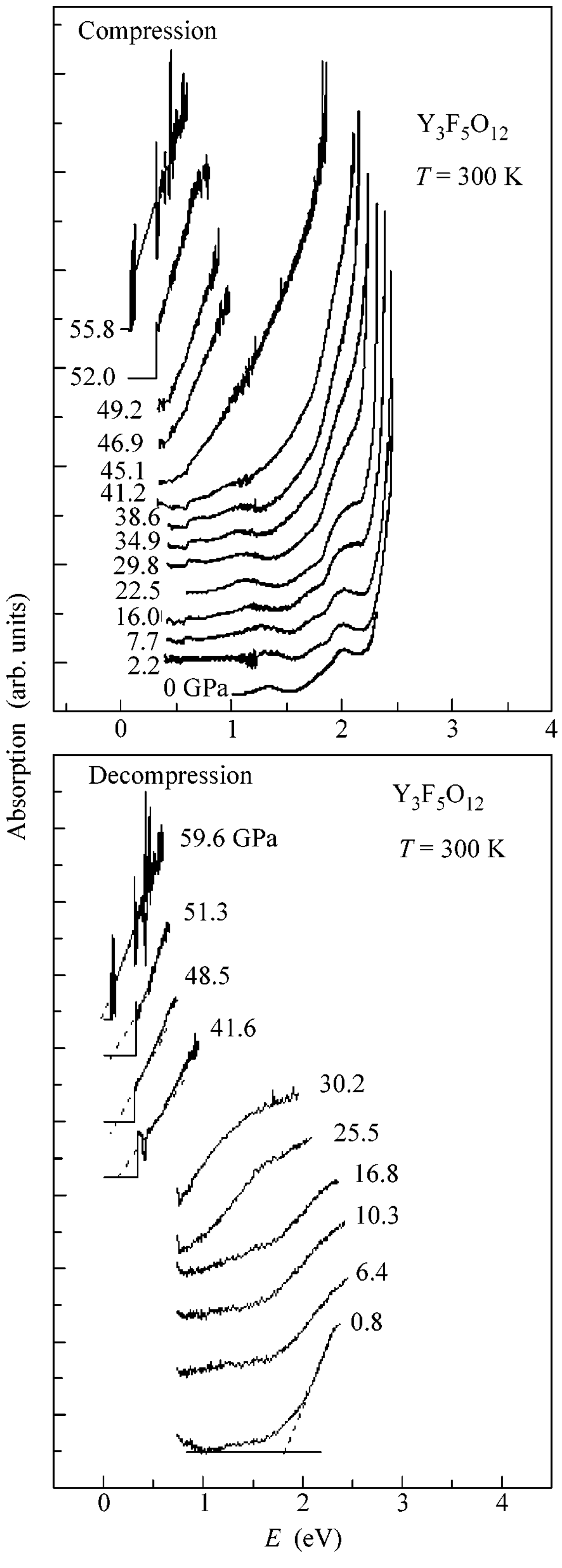

Fig. 1. Evolution of optical absorption spectra in the $Y_3Fe_5O_{12}$ single crystal with pressure increase and at decompression. The spectra are recorded at room temperature.

SpectraPro-500i grating monochromator using a spectral resolution of about 40 cm^{-1}. An Andor charge-coupled device (CCD) detector with the Peltier cooling system was used. The experimental setup used mirror optics to focus the light beam on the sample and also to focus the transmitted radiation onto the entrance slit of an optical monochromator. The diameter of the light spot on the sample surface was about 40 μm. To eliminate possible stray signals, confocal pinholes were used; we measured the reference signal $\mathbf{I}_0$ outside the sample through the pressure medium and then the signal $\mathbf{I}$ transmitted through the sample. The absorption spectrum was calculated by the standard method from the formula $\mathbf{I} = \mathbf{I}_0\exp(-\alpha d)$, where d is the sample thickness and α is the optical absorption coefficient.

RESULTS AND DISCUSSION

The room-temperature evolution of optical absorption spectra in $Y_3Fe_5O_{12}$ single crystal with increasing pressure and under decompression is shown in Fig. 1. The spectra exhibit rather wide absorption bands, corresponding to the *d–d* optical transitions of the Fe^{3+} ion in the ligand crystal field. At ambient pressure before compression, the shape of the spectrum coincides with those obtained previously in [5, 6].

The sample remains transparent down to ~940 cm^{-1} (~0.11 eV). Below this energy, a strong lattice absorption was observed due to vibrations of the ions in the unit cell of the crystal [6]. The high-energy absorption edge is due to electronic transitions. At ambient pressure, below the absorption edge which occurs at ~2.6 eV, several broad absorption peaks are observed with maxima at ~2.0 and ~1.40 eV [6]. Two broad bands at ~1.4 and ~2 eV are formed by several *d–d* transitions of Fe^{3+} ion in octahedral and tetrahedral ligand crystal fields [5, 6]. The band at ~1.4 eV corresponds to the ${}^6A_{1g} \longrightarrow {}^4T_{1g}$ transition of Fe^{3+} ion in octahedral sites. The second band at ~2 eV corresponds to the ${}^6A_1 \longrightarrow {}^4T_1$ transition of Fe^{3+} ion in tetrahedral sites. We denote the absorption band at ~1.4 eV as the **A** band and that at ~2 eV as the **B** band.

We found that, during compression, the energies of *d–d* transitions and the absorption edge linearly decrease (Fig. 2), and their pressure slopes are –7.81 ± 0.43, –1.66 ± 0.22, and –8.2 ± 1.3 meV/GPa for the **A** and **B** bands and for the absorption edge, respectively. The parameters of pressure dependences for the edge and absorption bands in YIG are presented in the table. For comparison, the analogous parameters of the $NdFeO_3$ orthoferrite, where iron ions are located only in the octahedral sites, are also given in the table from our recent study [7]. The comparison shows that the dE/dP values for octahedral sites in YIG and orthoferrite are close (in the limit of 30%), while, for tetrahedral sites of YIG, the dE/dP value is much lower.

In the pressure range from 40 to 50 GPa, the absorption edge of YIG exhibits a rapid decrease from ~2.3 to ~0.05 eV, which testifies to an electronic transition with possible metallization. The final drop of the optical gap to zero is extrapolated to be at about 55 GPa, indicating a possible complete transition to a metal state. We evaluated the zero value of the optical gap from linear extrapolation of the absorption spectrum to zero intensity. At pressures higher than 55 GPa, this extrapolation gave negative values of the optical gap, and, therefore, we can conclude that, above 55 GPa, the complete metallization of YIG is possible.

The Fe^{3+} ion in the octahedral and tetrahedral sites does not exhibit any remarkable absorption in the visible range. Therefore, the strong absorption in oxides is attributed to the charge transfer $d^n \longrightarrow d^{n+1}L$, where $n = 5$ and L is a hole in the oxygen p band [8, 9]. From the theoretical point of view, $Y_3Fe_5O_{12}$ is a strongly correlated electronic system in which, according to the Mott–Hubbard model, the gap Δ formed in the excitation spectrum due to the $O^{2-} \longrightarrow Fe^{3+}$ charge transfer is smaller than the Coulomb interaction energy U [10]. For example, for octahedral clusters in the orthoferrite $LaFeO_3$, the parameters of the model determined from the X-ray and UV photoemission data are $\Delta = (2.4 \pm 0.7)$ eV and $U = (7.4 \pm 0.7)$ eV [11].

It was demonstrated in [6] that the main contribution to the intensity of the **A** band comes from the transition $^6A_{1g} \longrightarrow {}^4T_{1g}$ of Fe^{3+} ion in octahedral sites, while the main contribution to the intensity of the **B** band is due to the $^6A_1 \longrightarrow {}^4T_1$ transition of Fe^{3+} ion in tetrahedral sites. In Fig. 3, the Tanabe–Sugano diagrams showing the dependence of energy terms on the crystal field are shown for Fe^{3+} ions in octahedral and tetrahedral sites. Figure 4 shows assignments of the absorption bands positions in YIG in comparison with those in the rare-earth orthoferrites (REO) and with calculations from [6]. Our comparison of the pressure behaviors of d–d transitions energy in REO and YIG (see table and Figs. 3, 4) supports the conclusions made in [6] that the **A** band is due to the transition in octahedral sites while the **B** band is due to the transition in tetrahedral sites.

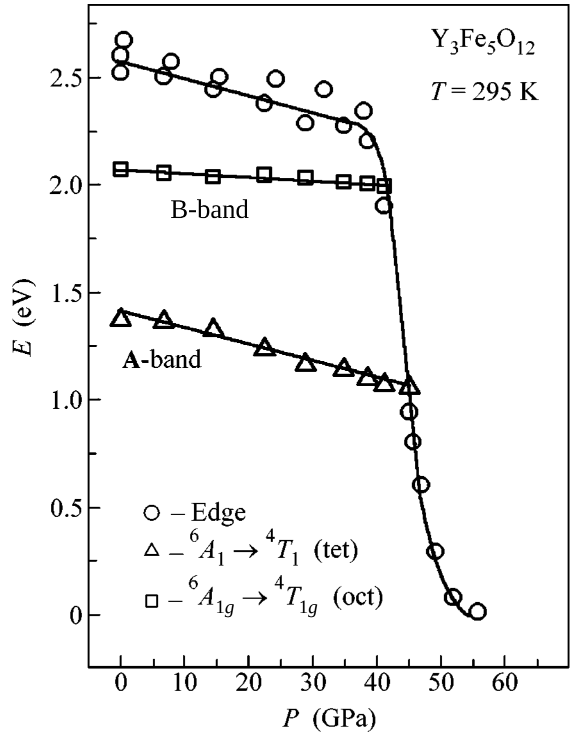

Fig. 2. Pressure (P) dependence of the optical absorption edge and energies of d–d transitions $^6A_1 \longrightarrow {}^4T_2$ and $^6A_1 \longrightarrow {}^4E, {}^4A$ for the pressure increase regime. Solid lines for d–d transitions are linear fits.

The room-temperature parameters of the optical absorption bands in the $NdFeO_3$ and $Y_3Fe_5O_{12}$ single crystals at ambient pressure and their pressure slopes

Transition	Energy at ambient pressure, eV	Pressure coefficient dE/dP, meV/GPa
$NdFeO_3$ [7]		
Edge (charge transfer)	2.42 ± 0.03	−6.94 ± 1.62
$^6A_{1g} \longrightarrow {}^4E_{1g}, {}^4A_{1g}$ (oct)	2.29 ± 0.02	−16.5 ± 0.7
$^6A_{1g} \longrightarrow {}^4T_{2g}$ (oct)	1.73 ± 0.02	−9.5 ± 0.7
$^6A_{1g} \longrightarrow {}^4T_{1g}$ (oct)	1.23 ± 0.01	−10.69 ± 0.4
$Y_3Fe_5O_{12}$		
Edge (charge transfer)	2.60 ± 0.03 (this study)	−8.23 ± 1.30 (this study)
$^6A_1 \longrightarrow {}^4T_1$ (tet)	2.033 [6]	
	2.066 ± 0.006 (this study)	−1.66 ± 0.22 (this study)
$^6A_{1g} \longrightarrow {}^4T_{1g}$ (oct)	1.40 [6]	
	1.40 ± 0.01 (this study)	−7.81 ± 0.43 (this study)

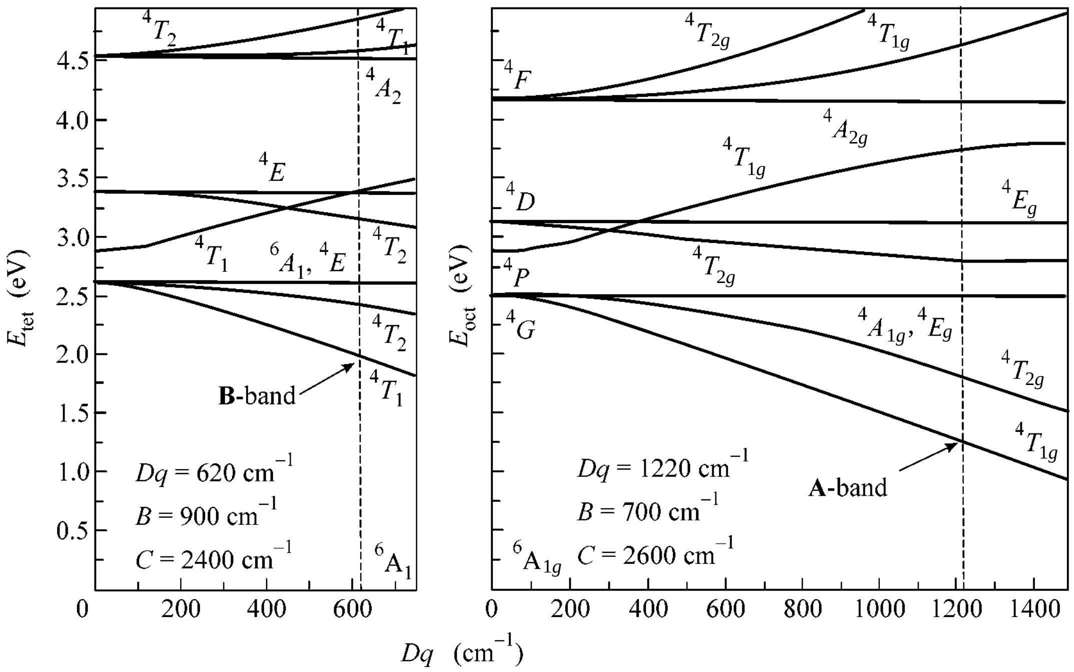

Fig. 3. The Tanabe–Sugano diagram (from [6]) for tetrahedral (left) and octahedral (right) environments of Fe^{3+} ion. *B* and *C* are the Racah parameters.

Using our experimental values for pressure slopes of the **A** and **B** band energies and the Tanabe–Sugano diagram from [6], we can evaluate the pressure slopes of crystal-field parameter for octahedral and tetrahedral sites using a simple equation:

$$\frac{d(D_q)}{dP} = \frac{1}{\partial E/\partial(Dq)}\frac{\partial E}{\partial P}. \qquad (1)$$

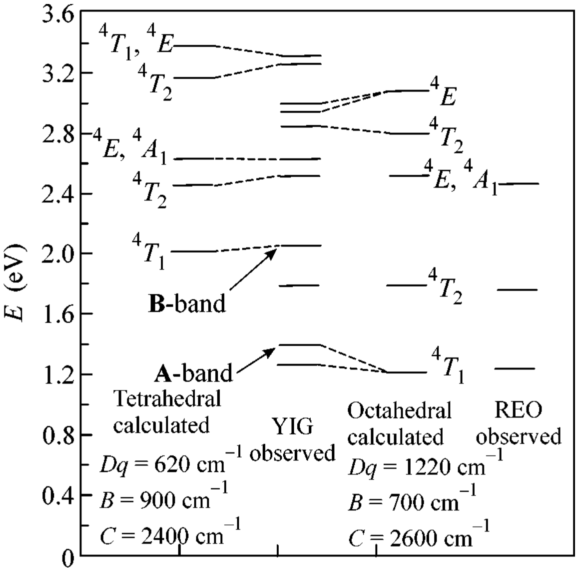

Fig. 4. Assignments of the absorption bands positions in $Y_3Fe_5O_{12}$ in comparison with rare-earth orthoferrites $RFeO_3$ (REO) and with calculations from [6]. *B* and *C* are the Racah parameters.

Here, 10*Dq* is the energy splitting of the term $(d^1)^2D$ in a crystal field and *E* is the energies of consequent terms in the Tanabe–Sugano diagram.

The value of $\partial E/\partial(Dq)$ can be calculated from the Tanabe–Sugano diagram taking the Racah parameters *B* and *C* to be independent of pressure. We found that these derivatives are equal to –9.2 for octahedral sites and –10.4 for tetrahedral sites of YIG. Using these values and our experimental data for $\partial E/\partial P$ (table), we have finally

$$\frac{\partial(Dq)_{\text{oct}}}{\partial P} \simeq +0.85 \text{ meV GPa}^{-1}, \qquad (2)$$
$$\frac{\partial(Dq)_{\text{tet}}}{\partial P} \simeq +0.16 \text{ meV GPa}^{-1}.$$

A very interesting effect was observed at the pressure decrease. We found that the observed electronic transition in YIG is irreversible. Figure 5 shows the pressure dependence of the optical absorption edge both for a pressure increase and decompression. It is obvious that there is a huge hysteresis and irreversibility in the behavior of the optical gap. After decompression from the high-pressure state to ambient pressure,

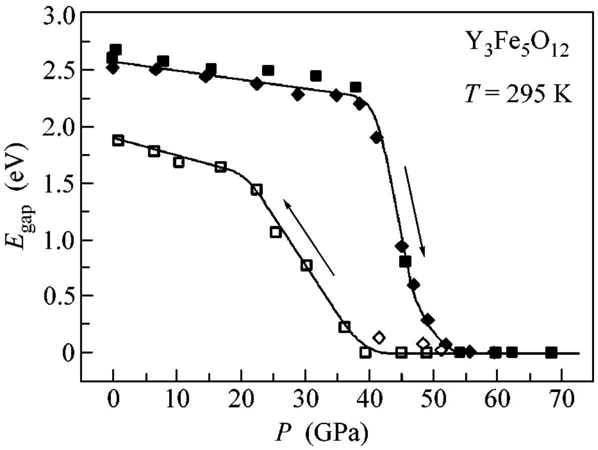

Fig. 5. Pressure dependence of the optical absorption edge in $Y_3Fe_5O_{12}$ for the pressure increase (black squares and diamonds) and pressure decrease (open diamonds and squares) regimes. The two sets of symbols correspond to two sets of independent measurements. The solid line is a guide for the eye.

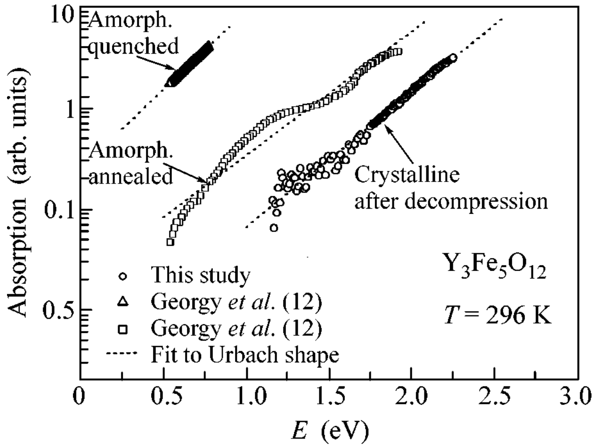

Fig. 6. Optical absorption spectrum of $Y_3Fe_5O_{12}$ after decompression to ambient pressure in comparison with that from the amorphous YIG synthesized and investigated by Georgy *et al.* [12]. The absorption intensity (Y coordinate) of the spectra is given on the logarithmic scale.

the optical gap is equal to ~1.8 eV, while its initial value is ~2.6 eV. Moreover, the shape of the spectrum is drastically changed from the initial one. After decompression, no absorption bands of the *d*–*d* transitions were observed. The spectral shape becomes very broad and has a tail with exponential decay. A very similar behavior was observed for the amorphous YIG synthesized in [12].

Figure 6 shows the optical spectrum of our YIG after decompression to ambient pressure in comparison with the spectra from the amorphous YIG synthesized and investigated by Georgy *et al.* [12]. The absorption intensity (Y coordinate) of the spectra is represented on the logarithmic scale. It is obvious that, after decompression, the shape of the absorption edge is close to the exponential function $I \propto \exp(E/E_0)$ with parameter $\Gamma = 1/E_0 \sim 3.3$ eV^{-1}. According to the empirical relation for exponential Urbach-type absorption edges [13], this shape could correspond to an amorphous state. For different samples of amorphous YIG [12], the parameter $\Gamma = 1/E_0$ is close to the same value (~3 eV^{-1}). Thus, we can suggest that, at the high-pressure transition in our YIG, the crystal transforms irreversibly into an amorphouslike state.

The most important effect is the drastic decrease in the optical gap in the pressure range of 40–50 GPa. The decrease is not abrupt, which implies the existence of some transient regime in this range of pressure when electronic correlations are suppressed and 3*d* electrons of Fe^{3+} ions are delocalized. This effect occurs due to the transition of the YIG crystal to a new, most probably metallic state. Thus, in the critical region of pressures, the YIG crystal transforms from the antiferromagnetic insulating state to most probably a paramagnetic metallic state. This transition is irreversible and accompanied by possible crystal amorphization. Simultaneously, with metallization, the transition of the iron ions from the high-spin to the low-spin state is possible, analogously to the phenomenon that was recently observed in several complex iron oxides in a pressure range of 30–50 GPa [7, 14–16]. But this hypothesis needs additional experimental investigation.

Additional information about the crystal structure before and after transition, as well as about ion spin states and magnetic properties, can be obtained from high-pressure X-ray diffraction, Mössbauer absorption, nuclear forward scattering (NFS), and high-resolution X-ray emission spectroscopy (XES) techniques. These types of experiments are planned for the near future.

This work is supported by the US Department of Energy (grant no. DE-FG02-02ER45955), the Russian Foundation for Basic Research (project nos. 04-02-16945a and 05-02-16142a), and by the Physical Division of the Russian Academy of Sciences (project “Strongly Correlated Electronic Systems”).

REFERENCES

1. C. Kittel, *Introduction to Solid State Physics*, 4th ed. (Wiley, New York, 1971; Nauka, Moscow, 1978).
2. L. Neel, R. Pauthenet, and B. Dreyfus, Prog. Low Temp. Phys. **4**, 344 (1964).
3. S. Geller, J. P. Remeika, R. C. Sherwood, *et al.*, Phys. Rev. A **137**, 1034 (1965).
4. D. Rodic, M. Mitric, R. Tellgren, *et al.*, J. Magn. Magn. Mater. **191**, 137 (1999).
5. A. M. Clogston, J. Appl. Phys. **31**, S198 (1960).
6. D. L. Wood and J. P. Remeika, J. Appl. Phys. **38**, 1038 (1967).

7. A. G. Gavrilyuk, I. A. Troyan, R. Boehler, *et al.*, Pis'ma Zh. Éksp. Teor. Fiz. **77**, 747 (2003) [JETP Lett. **77**, 619 (2003)].
8. D. L. Wood, J. P. Remeika, and E. D. Kolb, J. Appl. Phys. **41**, 5315 (1970).
9. F. G. Kahn, P. S. Pershan, and J. P. Remeika, Phys. Rev. **186**, 891 (1969).
10. J. Zaanen, G. A. Sawatsky, and J. W. Allen, Phys. Rev. Lett. **55**, 418 (1985).
11. A. E. Bocquet, A. Fujimori, T. Mizokawa, *et al.*, Phys. Rev. B **45**, 1561 (1992).
12. E. M. Gyorgy, K. Nassau, M. Eibschutz, *et al.*, J. Appl. Phys. **50**, 2883 (1979).
13. N. F. Mott and E. A. Davis, *Electronic Processes in Non-Crystalline Materials*, 2nd ed. (Clarendon, Oxford, 1979; Mir, Moscow, 1982).
14. A. G. Gavriliuk, I. A. Trojan, I. S. Lyubutin, *et al.*, Zh. Éksp. Teor. Fiz. **127**, 780 (2005) [JETP **100**, 688 (2005)].
15. A. G. Gavriliuk, S. A. Kharlamova, I. S. Lyubutin, *et al.*, Pis'ma Zh. Éksp. Teor. Fiz. **80**, 482 (2004) [JETP Lett. **80**, 426 (2004)].
16. A. G. Gavriliuk, V. V. Struzhkin, I. S. Lyubutin, *et al.*, Pis'ma Zh. Éksp. Teor. Fiz. **82**, 243 (2005) [JETP Lett. **82**, 224 (2005)].

JETP Letters, Vol. 82, No. 9, 2005, pp. 609–612. Translated from Pis'ma v Zhurnal Éksperimental'noĭ i Teoreticheskoĭ Fiziki, Vol. 82, No. 9, 2005, pp. 688–692.
Original Russian Text Copyright © 2005 by Kazeĭ, Snegirev, Broto, Rakoto.

Jahn–Teller Magnet $TbVO_4$ in a Strong Magnetic Field up to 50 T

Z. A. Kazeĭ[a], V. V. Snegirev[a], J.-M. Broto[b], and H. Rakoto[b]
[a] *Moscow State University, Vorob'evy gory, Moscow, 119992 Russia*
e-mail: kazei@plms.phys.msu.su
[b] *Laboratoire National des Champs Magnetiques Pulses, 31432 Toulouse, France*

Received October 11, 2005

Magnetic properties of the Jahn–Teller crystal $TbVO_4$ are studied in pulse magnetic fields up to 50 T. The destruction of quadrupole ordering accompanied by an increase in crystal symmetry from orthorhombic to tetragonal has been revealed at $H_c = 32$ T. An adequate description based on the interaction parameters determined previously is proposed for magnetic anomalies and critical parameters of the induced phase transition. It is noted that the Jahn–Teller crystal $TbVO_4$ may be of interest for investigations using synchrotron radiation in a pulsed magnetic field. *© 2005 Pleiades Publishing, Inc.*

PACS numbers: 71.70.–d, 75.30.–m, 75.40.Cx

It is known that a magnetic field strongly affects the phase states and magnetic properties of Jahn–Teller compounds. Both suppression and enhancement of the Jahn–Teller (quadrupole) order parameter can be expected, depending on the magnetic field orientation. The suppression of quadrupole ordering for a magnetic field orientation differing from the direction of the Jahn–Teller distortion occurs as a rule in rather strong magnetic fields and, therefore, is little investigated. Experimental studies for the zircon structure were performed on $TmVO_4$, which has the lowest critical temperature $T_c = 2.15$ K and critical field $\mu_0 H_c \approx 0.6$ T [1]. Considerable progress in the technique of pulsed magnetic field generation has allowed similar experiments to be performed with other Jahn–Teller magnets, and widening the range of properties and effects available for investigations under these conditions, for example, combining the technique of pulsed magnetic fields and synchrotron radiation, makes them more informative. Detailed studies of the suppression of quadrupole and magnetic orderings in a pulsed magnetic field for another zircon $DyVO_4$ [2] showed that a refined compressible model must be used to describe the behavior of this compound. This work is devoted to an experimental and theoretical investigation of the effect of a strong magnetic field up to 50 T on the quadrupole ordering in the classical Jahn–Teller magnet $TbVO_4$, for which the effective field model in principle works well.

According to the studies of thermodynamic [3] and spectroscopic [4] characteristics, terbium vanadate undergoes a structural phase transition at $T_Q = 33$ K, which gives rise to a distortion of the tetragonal D_{4h}^{19} zircon crystal structure along the [110] axis to the orthorhombic D_{2h}^{24} structure. The transition is a cooperative Jahn–Teller effect accompanied by the ordering of quadrupole moments of Tb^{3+} ions due to their specific electronic structure. At $T_N = 0.6$ K, $TbVO_4$ becomes an antiferromagnet with the magnetic moments of Tb^{3+} ions oriented along the [110] axis [5]. The Jahn–Teller transition in this compound has been studied in detail by various methods, but studies in strong magnetic fields are unavailable.

Measurements of the differential magnetic susceptibility $dM/dH(H)$ of the $TbVO_4$ crystal in the temperature range 1.4–35 K for the $H \parallel [001]$ magnetic field orientation were performed by the induction method using the facilities of the Laboratoire National des Champs Magnetiques Pulses (National Laboratory of Pulsed Magnetic Fields) (Toulouse, France). The field was generated by a discharge of a capacity bank into a copper coil. The maximum field of 50 T was reached in 20 ms, and the downsweep time was ~100 ms. The pulse durations in our experiments were such that the magnetization regimes can be considered as being close to adiabatic for upsweep and intermediate for downsweep. This requires that the magnetocaloric effect (MCE) be taken into account in the analysis of experimental data. The misorientation of the field with respect to the [001] axis under the experimental conditions was equal for all temperatures and did not exceed 1°–1.5°. Measurements of $TbVO_4$ crystal magnetization curves in steady magnetic fields up to 8 T along the symmetric [100], [110], and [001] directions in the temperature range 1.5–300 K were used to determine the initial magnetic susceptibility necessary for crystal-field (CF) analysis.

Experimental temperature dependences of the magnetic susceptibility along the tetragonal [001] axis and the [110] direction of Jahn–Teller distortion (Fig. 1) reveal distinct anomalies at $T_Q = 33$ K due to a change in the electronic structure of the Tb^{3+} ion upon the qua-

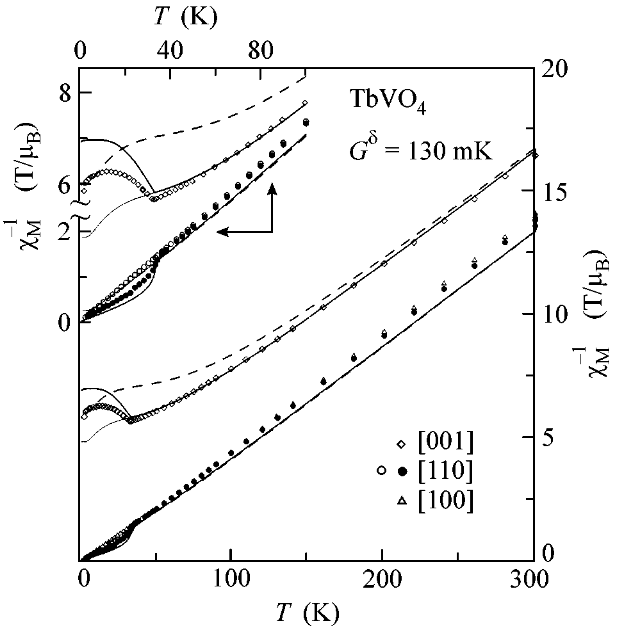

Fig. 1. Temperature dependences of the inverse magnetic susceptibility of a $\mathrm{TbVO_4}$ crystal along the [100], [110], and [001] axes. Lines show dependences calculated (thin lines at $T < T_Q$ and dashed lines) without and (solid lines) with the inclusion of the quadrupole constant $G^\delta = 130$ mK for two sets of the crystal-field parameters (solid lines for set 2 from [10] and dashed lines for the set of crystal-field parameters for $\mathrm{HoVO_4}$).

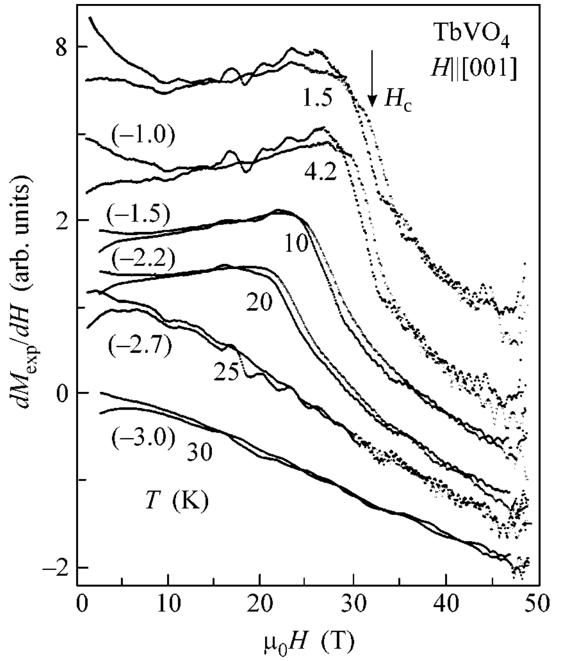

Fig. 2. Experimental curves of the differential magnetic susceptibility $dM/dH(H)$ of a $\mathrm{TbVO_4}$ crystal for various temperatures for the (closed points) upsweep and (open points) downsweep of the field. The curves are shifted along the vertical axis by the indicated value.

drupole transition. For the field along the [001] and [100] axes, the domain state of the sample in the quadrupole-ordered phase has no effect on the value and character of the anomalies because the two types of the domains with the [110] and [1–10] deformation axes make the same contribution. In contrast, the anomaly along the [110] axis becomes more pronounced with increasing field and sample monodomainization (the inset in Fig. 1). Thus, the magnetic susceptibility is sensitive to a change in the electronic structure of the $\mathrm{Tb^{3+}}$ ion upon the initiation or suppression of quadrupole ordering, and this transition can be investigated by magnetic anomalies, in particular, by measuring the $dM/dH(H)$ curves in pulsed magnetic fields.

Experimental $dM/dH(H)$ curves for the $\mathrm{TbVO_4}$ crystal at $H \parallel [001]$ are shown in Fig. 2 for various temperatures $T < T_Q$. The jump in $dM/dH(H)$ curves, which is somewhat smeared evidently because of a small misorientation of the field with respect to the [001] axis, is typical of second-order phase transitions; the value of the critical field at the starting temperature $T_{st} = 4.2$ K is $H_c = 32$ T. The critical field and the anomaly value weakly vary at T_{st} below ~ 10 K and start to rapidly decrease and smear above this temperature. The value of H_c for the increasing field is smaller than for the decreasing field, which, in our opinion, can be associated with the heating of the sample due to MCE for a shorter increasing field pulse.

To calculate the effect of a strong magnetic field on the phase states and magnetic properties of $\mathrm{TbVO_4}$, a Hamiltonian H was used that contained the CF Hamiltonian H_{CF}, the Zeeman term H_Z, and the Hamiltonian of bilinear H_B and quadrupole H_{QT} interactions written in the formalism of equivalent operators O_n^m

$$\begin{aligned} H_{CF} &= \alpha_J B_2^0 O_2^0 \\ &+ \beta_J(B_4^0 O_4^0 + B_4^4 O_4^4) + \gamma_J(B_6^0 O_6^0 + B_6^4 O_6^4), \end{aligned} \tag{1}$$

$$H_Z = -g_J \mu_B \mathbf{H} \cdot \mathbf{J}, \tag{2}$$

$$\begin{gathered} H_B = -g_J \mu_B \mathbf{H}_B \cdot \mathbf{J}, \quad \mathbf{H}_B = n g_J \mu_B \langle \mathbf{J} \rangle \\ (n = \theta/C), \end{gathered} \tag{3}$$

$$\begin{gathered} H_{QT} = -G^\alpha \langle O_2^0 \rangle O_2^0 - G^\delta \langle P_{xy} \rangle P_{xy}, \\ \left(P_{xy} = \frac{1}{2}(J_x J_y + J_y J_x)\right). \end{gathered} \tag{4}$$

In these equations, B_n^m are crystal-field parameters; α_J, β_J, and γ_J are Stevens coefficients; g_J and μ_B are the Lande factor and the Bohr magneton; and $\mathbf{J}$ is the angular momentum operator of the rare-earth ion. The value of the quadrupole constant of the δ symmetry $G^\delta = 130$ mK was determined from the temperature of the spontaneous quadrupole transition T_Q, and the totally symmetric constant $G^\alpha = 4.5$ mK was determined from magnetostriction data for the related $TbPO_4$ compound. The bilinear interaction parameter $\theta_z \approx -2$ K in $TbVO_4$ was estimated from the magnetic ordering temperature of the neighboring $DyVO_4$ compound. The calculations are more conveniently performed in the coordinate system rotated through an angle of 45° about the z axis, which corresponds to the transformation of parameters B_4^4, $B_6^4 \longrightarrow -B_4^4, -B_6^4$ and $\langle P_{xy}\rangle \longrightarrow \frac{1}{2}\langle O_2^2\rangle$. In this case, the quadrupole term $G^\delta\langle P_{xy}\rangle P_{xy}$ can be presented in the form of the ortorhombic component $\alpha_J B_2^2 O_2^2$ in the CF Hamiltonian in which the parameter $B_2^2 = -1/4G^\delta\langle O_2^2\rangle/\alpha_J$ depends on temperature and magnetic field because of the dependence of the quadrupole moment $\langle O_2^2\rangle$.

The problem of CF in $TbVO_4$ remains open to the present date, because there is no sufficient spectroscopic data for the Tb^{3+} ion in the tetragonal phase. According to the optical absorption spectra [5, 6] and studies of Raman scattering [7, 8] and electron resonance [9], the lower part of the ground multiplet of the Tb^{3+} ion split in the CF has a singlet–doublet–singlet scheme and the next doublet arranged at ~90 cm^{-1}. Three sets of CF parameters were obtained in [10] to describe this spectrum and the magnetization curves in the region of helium temperatures from [11]. We analyzed all the sets of CF parameters available for $TbVO_4$ and the neighboring $HoVO_4$ compound [12] for the purpose of their applicability to the description of our experiment. The CF parameters determined for $HoVO_4$ based on experimental data on magnetic susceptibility, g-tensor components, and spectroscopic information are considered to be reliably established. It turned out that set 2 from [10] ($B_2^0 = -92$, $B_4^0 = 45$, $B_6^0 = -46$, $B_4^4 = 652$, $B_6^4 = -71$ cm^{-1}) is best to describe the magnetic susceptibility of $TbVO_4$ in the tetragonal phase. This set is used in the subsequent calculations (see Fig. 1). With this set, the singlet–doublet and doublet–second singlet gaps in the tetragonal phase are ~12 cm^{-1} and 14 cm^{-1}, which is close to experimental data. Sets 1 and 3 from [10] somewhat worse describe the data, and the set for $HoVO_4$ and the set from [11] rather poorly describe the data. Note that the susceptibility along the easy [100] axis virtually coincides for all the sets listed above and is little sensitive to the electronic structure and CF parameters. Calculations with set 2 and the above interaction parameters provide a reasonable description of anomalies due to the quadrupole transition in the $\chi_M^{-1}(T)$ curves (see Fig. 1).

According to the calculations, the magnetic field $H \parallel [001]$ at $T < T_Q$ destroys the quadrupole ordering and converts the crystal from the orthorhombic to tetragonal phase, which corresponds to a sharp jump in the $dM/dH(H)$ curve in the field $\mu_0 H_c \approx 30$ T. Calculations performed without fitting parameters demonstrate a reasonable agreement of experimental and calculated curves shown in Fig. 3 (scales in the figure are selected in such a way that the experimental and theoretical susceptibility curves coincide in weak fields). When the experimental and calculated curves are compared, it is necessary to take into account the change in the sample temperature caused by the MCE. According to the calculations, the magnitude and sign of the MCE strongly depend on the field orientation: for the field strictly aligned with the [001] axis at $T_{st} = 4.2$ K, the crystal cools down upon magnetization up to the critical field, whereas a small misorientation by ~2° from the axis leads to monotonic heating of the sample by ~ 6 K. The jump width in the $dM/dH(H)$ curves suggests that the misorientation of the crystal in our experiment was ~1°, which must lead at $T_{st} = 4.2$ K to heating of the sample due to the MCE in the region of H_c by ~3–5 K. This is also confirmed by the fact that the anomaly in the $dM/dH(H)$ curves is no longer observed at T_{st} above 25 K. The heating of the sample upon magnetization

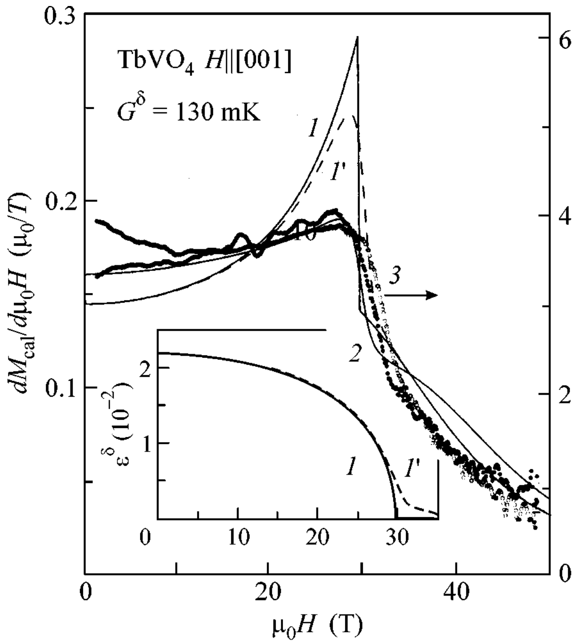

Fig. 3. Experimental ($T_{st} = 4.2$ K; closed points correspond to the upsweep of the field, open points correspond to the downsweep of the field) and calculated isothermal curves (lines $T_0 = 7$ K) of the differential magnetic susceptibility $dM/dH(H)$ of a $TbVO_4$ crystal for $H \parallel [001]$. Theoretical dependences were calculated using the parameter of quadrupole interactions $G^\delta = 130$ mK for two sets of the crystal-field parameters and various angles of field misorientation from the [001] axis (set 2 from [10]): $\Delta\theta$ = (*1*) 0 and (*1*') 1°; curve *2* is obtained for the set of parameters 2a. The inset shows the field dependence of the ortorhombic distortion $\varepsilon^\delta = (a' - b')/a'$ for two angles of field misorientation from the [001] axis: $\Delta\theta$ = (*1*) 0 and (*1*') 1°.

explains the mutual arrangement of the downsweep and upsweep $dM/dH(H)$ susceptibility curves and allows the observed hysteresis to be assigned mainly to the MCE.

Qualitative agreement between the experimental (at T_{st} = 4.2 K) and calculated (isothermal at T_0 = 7 K with regard to heating by ~3 K) $dM/dH(H)$ curves in the region of the critical field in Fig. 3 serves as a verification of the CF used. For a field strictly aligned with the [001] axis, the destruction of quadrupole ordering proceeds as a second-order phase transition, while misorientation generating a field component along the [110] axis leads to smearing of the phase transition (compare curves *1* and *1'*). Though the anomaly in the calculated curves is sharper, a better agreement with the experiment can be reached by slightly varying the CF parameters within the limits of ±20%. However, in our opinion, it makes sense to refine the CF and electronic structure of the Tb^{3+} ion simultaneously with regard for the contribution of weaker interactions, such as bilinear and totally symmetric quadrupole interactions. Taking into account negative bilinear interactions with the constant $\theta_z = -2$ K leads to a decrease in the critical field by ~0.5 T and a small (within 10%) decrease in the anomaly. The effect of the quadrupole constant G^α = 4.5 mK is opposite in sign and considerably stronger, so that the critical field decreases by ~4 T.

It is interesting to note that, for parameter set 2 in the absence of quadrupole ordering in the tetragonal phase, energy level crossing accompanied by a differential susceptibility peak would take place for the Tb^{3+} ions at H_{c1} = 27 T. In the tetragonal phase, this peak is superimposed on the anomaly due to the phase transition, which increases its magnitude at the critical field H_c. The critical field H_{c1} can be increased to ~32 T by small variations of the CF parameters ($\Delta B_4^0 = 9$ cm^{-1}, $\Delta B_6^0 = 9$ cm^{-1}, set 2a), and, in this way, the anomaly at H_c can be decreased and made closer to the experimental one (curve *2* in Fig. 3).

Thus, studies of the Jahn–Teller $TbVO_4$ magnet in a strong field up to 50 T revealed that the $H \parallel [001]$ field destroys quadrupole ordering and increases the crystal symmetry from ortorhombic to tetragonal. This transition is accompanied by significant anomalies of the magnetic properties, namely, a kink in the magnetization curve and a jump in the field dependence of the differential magnetic susceptibility. These anomalies were observed experimentally in this work. Our studies showed that the suppression of quadrupole ordering in $TbVO_4$, as well as the spontaneous quadrupole transition, is well described within the molecular field model. This distinguishes Tb vanadate from another Jahn–Teller magnet, $DyVO_4$, in the case of which a refined compressible model has to be used to describe induced and spontaneous transitions. This model takes into account an increase in pair interactions with increasing order parameter.

The order parameter of this induced transition is the quadrupole moment $Q_{xy} = \langle P_{xy} \rangle$. This moment is associated with a large magnetoelastic distortion $\varepsilon^\delta = B^\delta Q_{xy}/C_0^\delta$, which vanishes at the critical field H_c (inset in Fig. 3). The ortorhombic distortion in terbium vanadate reaches record values: $\varepsilon^\delta = (a' - b')/a' = 2.3 \times 10^{-2}$ for quadrupole transitions. This makes it possible to directly observe the structural phase transition induced by a strong magnetic field. At present, interest in various methods of investigations with the use of synchrotron radiation is increasing. Considerable progress has been reached in expanding the capabilities of these methods, in particular, in combining them with the technique of pulsed magnetic fields. Information obtained in this work on the induced phase transition in $TbVO_4$ allows it to be considered as a suitable model object of investigations using synchrotron radiation.

This work was supported in part by the Russian Foundation for Basic Research, project no. 03-02-16809.

REFERENCES

1. R. L. Melcher, E. Pytte, and B. A. Scott, Phys. Rev. Lett. **31**, 307 (1973).
2. A. A. Demidov, Z. A. Kazei, N. P. Kolmakova, *et al.*, Phys. Rev. B **70**, 134432 (2004).
3. M. R. Wells and R. D. Worswick, Phys. Lett. A **42A**, 269 (1972).
4. R. T. Harley, K. B. Lyons, and P. A. Fleury, J. Phys. C: Solid State Phys. **13**, L447 (1980).
5. G. A. Gehring, H. G. Kahle, W. Nagele, *et al.*, Phys. Status Solidi B **74**, 297 (1976).
6. K. A. Gehring, A. P. Malozemoff, W. Staude, and R. N. Tyte, Solid State Commun. **9**, 511 (1971).
7. R. J. Elliott, R. T. Harley, W. Hayes, and S. R. P. Smith, Proc. R. Soc. London, Ser. A **328**, 217 (1972).
8. R. T. Harley, W. Hayes, and S. R. P. Smith, Solid State Commun. **9**, 515 (1971).
9. B. Bleaney, J. Z. Pfeffer, and M. R. Wells, J. Phys.: Condens. Matter **9**, 7469 (1997).
10. A. A. Demidov and N. P. Kolmakova, Physica B (Amsterdam) **363**, 245 (2005).
11. A. A. Andronenko and A. N. Bazhan, Fiz. Tverd. Tela (Leningrad) **31** (2), 35 (1989) [Sov. Phys. Solid State **31**, 195 (1989)].
12. P. Morin, J. Rouchy, and Z. Kazei, Phys. Rev. B **51**, 15103 (1995).

Translated by A. Bagatur'yants

JETP Letters, Vol. 82, No. 9, 2005, pp. 613–615. Translated from Pis'ma v Zhurnal Éksperimental'noĭ i Teoreticheskoĭ Fiziki, Vol. 82, No. 9, 2005, pp. 693–696.
Original Russian Text Copyright © 2005 by Gabuda, Gaidash, Drebushchak, Kozlova.

Physical Properties and Structure of Bound Water in Collagen-Type Fibrillar Proteins as Studied by Scanning Calorimetry

S. P. Gabuda[a], A. A. Gaidash[a, b], V. A. Drebushchak[a, c], and S. G. Kozlova[a]

[a] *Nikolaev Institute of Inorganic Chemistry, Siberian Division, Russian Academy of Sciences,*
pr. Akademika Lavrent'eva 3, Novosibirsk, 630090 Russia
e-mail: gabuda@che.nsk.su
[b] *Institute of Clinical and Experimental Medicine, Siberian Division, Russian Academy of Medical Sciences,*
Novosibirsk, 630117 Russia
[c] *Institute of Mineralogy and Petrography, Siberian Division, Russian Academy of Sciences,*
Universitetskiĭ pr. 3, Novosibirsk, 630090 Russia

Received September 5, 2005; in final form, October 4, 2005

The first-order phase transition observed in half (~50%) of bound water in rat-tail tendon collagen has been studied by a calorimetric technique. The latent heat of transition, the transition temperature, and the specific heat of a high-temperature phase of this subsystem is found to be close to the characteristics of free water. The properties of the other half (~50%) of bound water in collagen are similar to the properties of zeolite water. *© 2005 Pleiades Publishing, Inc.*

PACS numbers: 87.15.By, 87.19.Pp

The fibrillar protein collagen accounts for about a third of total polypeptides in animal and human bodies [1]. The collagen contents of tendon, skin, and bone tissue are as high as 94, 75, and about 50%, respectively. One of the fundamental properties of collagen is that it contains a large amount of water, which accounts for about 66% of mass in a native (unaffected) state. It was found that water plays an important role in the self-assembling mechanism of collagen molecules and fibril formation in the cytoplasm of collagenocytes, as well as in the mechanisms of biochemical activity and function of collagen in the extracellular space of a living organism [1]. However, the fundamental nature of the hydrate structure of collagen remains unknown.

Collagen is characterized by high degrees of molecular ordering and crystallinity. According to x-ray diffraction data obtained using a synchrotron radiation beam [2, 3], the idealized structure of collagen belongs to space group **P**1 (triclinic) with the lattice parameters $a = 39.97$, $b = 26.95$, and $c = 677.9$ Å; $\alpha = 89.24°$; $\beta = 94.59°$; and $\gamma = 105.58°$. Rodlike macromolecules as triple helixes of three nonidentical chains of ~1040 amino acid residues each are the main structural units of collagen. The molecular weight of such a macromolecule (so-called tropocollagen) is ~300 000, and its length and diameter are ~2800 and ~14 Å, respectively. In the crystal structure of collagen, the macromolecules are stacked parallel to the *c* axis of the structure; the *ab* projection of a unit cell contains five sections of the macromolecules (Fig. 1, on the left), and H_2O molecules are arranged in a close space between the side groups of macromolecules.

Another structural type of H_2O localization in collagen belongs to a freer space between the C- and N-terminal groups of macromolecules. It is of importance that, in the longitudinal direction (*c*), macromolecules following each other do not contact through their C- and N-terminal groups, and the gaps are approximately equal to 350–370 Å. The distribution of such "vacancies" in the structure of collagen is strictly ordered both in *AB* planes, where $A = 5a$ and $B = 5b$ (Fig. 1, on the right), and along the direction of the *c* axis. This manifests itself as a characteristic transverse banding of collagen with the period $c_0 = 640$–700 Å; this banding is visible in electron micrographs (Fig. 2 [4–6]). The supramolecular structure that manifests itself as such a transverse banding of fibers is a characteristic property of all of the known (no less than 19 types [1]) proteins from the collagen group, which are different in primary-structure peculiarities. The presence of nanotanks ~30–35 Å in section and 350–370 Å in length in the collagen structure is a consequence of the ordered arrangement of vacancies; these nanotanks are free of collagen macromolecules, but they contain nanocapillary water.

To determine the fundamental nature of the hydrate structure of collagen, we studied samples of rat-tail tendons (RTTs). The distribution of water in the samples was studied by ^{2}H NMR spectroscopy. The 100- to 150-mg samples were taken immediately before a

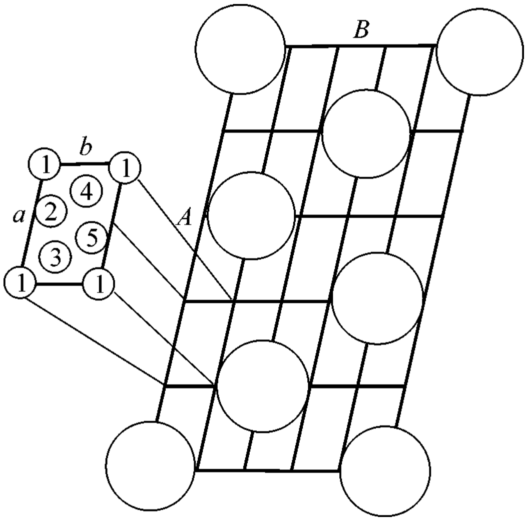

Fig. 1. Arrangement of tropocollagen macromolecules in a longitudinal projection (along the *c* axis). On the left: *ab* is the projection of a unit cell in dense regions of the collagen structure; numerals from 1 to 5 indicate the positions of the sections of structurally nonequivalent macromolecules. On the right: *AB* is the projection of a unit cell in loose regions of the collagen structure; large circles show the arrangement of cisterns, each of them is formed by the combination of longitudinal gaps between macromolecules from four neighboring subcells.

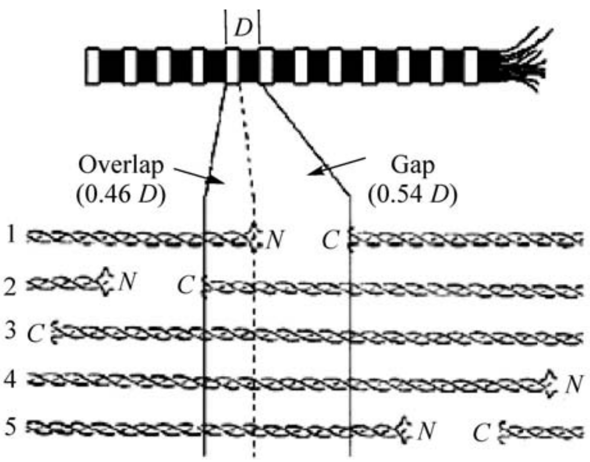

Fig. 2. Schematic diagram of the longitudinal stacking of tropocollagen macromolecules and the formation of transverse banding. The transverse banding period *D* of fibers is actually equal to c_0. Numerals from 1 to 5 denote the same as those in Fig. 1.

study and placed in 99% heavy water (for 20 min) to enrich them in the isotope ^{2}H. The ^{2}H NMR spectra (Fig. 3) are the superposition of two types of bands: a doublet characteristic of disordered quasi-liquid-crystal systems [7] and a central line characteristic of the liquid phase of water; the ratio between the two types is ~1 : 1. The subsystem of water molecules in space between the side groups of macromolecules can be assigned to the former type, whereas the central line can be attributed to the water subsystem of cisterns from gap regions. This conclusion is supported by a stepwise disappearance of the central line as the temperature was decreased below –10°C; this can be due to the formation of a nanoice-in-nanotanks phase. This fact indirectly supports a model according to which loose regions of the collagen structure consist of a tectohydrate or a structure that includes a continuous three-dimensional framework of water molecules with a tetrahedral coordination, which is characteristic of ice and clathrate hydrates. This model of the arrangement of water molecules in the wide-pore structure of collagen in gap regions can be directly supported by an analysis of the latent heat of a phase transition in rat-tail tendons. This phase transition was detected using not only ^{2}H NMR-spectroscopic [8] but also scanning calorimetric data.

The study of tendon samples was performed with the use of a Netzsch DSC 204 automatic calorimeter (Germany). The measurements were performed over a range from room temperature (+20°C) to –30°C; the rate of temperature change was 3 K/min. Figure 4 shows a typical cooling–heating curve. The experimental curves exhibited supercooling with the freezing temperature $T_f = -9.2 \pm 0.5$°C and the latent heat of crystallization $Q_f = -73.3 \pm 1.9$ J/g; for heating curves, the maximum melting temperature was $T_m = +2.3 \pm 0.2$°C and the latent heat of melting was $Q_m = 89.15 \pm 2.0$ J/g. These experimental data can be compared with the reference value for the latent heat of melting of pure ice: $Q_m(\text{ice}) = 333.5$ J/g [9]. In this comparison, it should be taken into account that the collagen content of tendons is as high as 94% and the total water content of native collagen is about ~60%, including ~30% in nanocapillaries. Thus, if the structure of the subsystem of water molecules in the vacancy regions of the collagen structure at negative temperatures corresponds to the structure of a tectohydrate (clathratelike or icelike type), the expected latent heat of a phase transition in this subsystem is $Q_m(\text{RTT}) = {\sim}(0.3 \times 0.94)$, $Q_m(\text{ice}) = {\sim}94$ J/g, which is consistent with the values measured in three samples.

The cooling curves exhibited reduced values of Q_f; this is a consequence of a considerable supercooling of the samples as the temperature was decreased. This effect allowed us to estimate the specific heat c_p of a high-temperature phase in the subsystem of water molecules that underwent the phase transition. In terms of the model under discussion, the average change in the heat of the phase transition $\Delta Q_{tr} = 16.55 \pm 3.9$ J/g is related to the average supercooling temperature $\Delta T = (11.5 \pm 0.7)°$ by the expression $\Delta Q_{tr}(\text{RTT}) = {\sim}(0.3 \times 0.94)\Delta c_p \Delta T$, where Δc_p is the difference between the heat capacities of water and ice. If the properties of the water subsystem that underwent phase transition in collagen correspond to the properties of free water and ice,

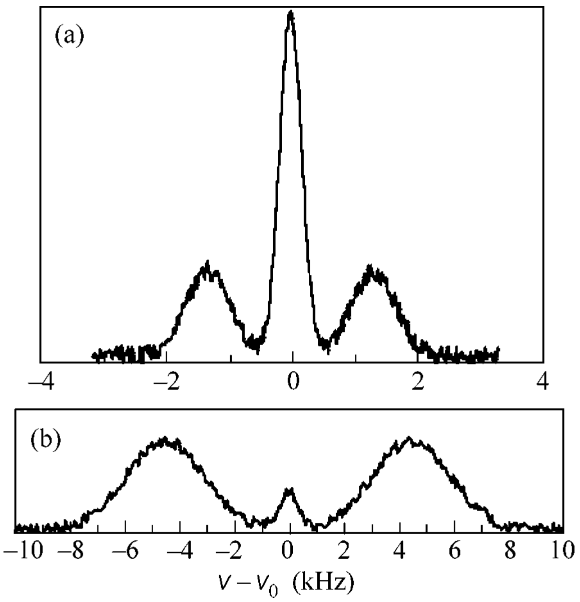

Fig. 3. ^{2}H NMR spectra of a single rat-tail tendon fiber oriented perpendicularly to the magnetic field of the spectrometer at (a) room temperature and (b) –10°C. Recording conditions: Bruker CXP-300 spectrometer, Larmor frequency ν_0 = 46 MHz, and measurement of the spectra after a pulse. The distance between doublet components is $\Delta\nu = 3/4C_{qcc}$, where C_{qcc} is the effective quadrupole coupling constant of ^{2}H nuclei.

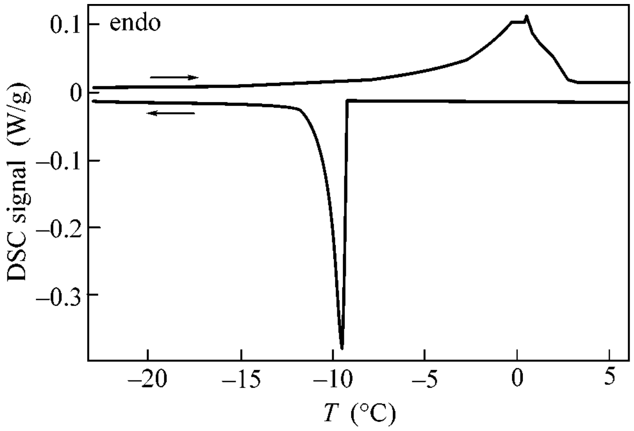

Fig. 4. Typical differential scanning calorimetry (DSC) curve of rat-tail tendon from Wistar rats. The number of laboratory animals in the group was 3, the age was 6 months, the tendon sample weight was 40 mg, and the rate of temperature change was 3 K/min. The top and bottom curves correspond to heating and cooling, respectively.

Δc_p = 2.062 J g^{-1} K^{-1} (near 0°C [9]). Therefore, the calculated value is ΔQ_{tr}(RTT) = ~6.69 J/mol; this calculated value of ΔQ_{tr}, which is lower than the experimental value, suggests that the interaction of water molecules and functional groups in cisterns makes a contribution to Δc_p. For example, telopeptides, which were reliably detected in the neighborhood of gaps [2], can serve as these functional groups. An analogous conclusion also follows from an increase in the melting temperature of ice in collagen, as compared with that of free ice (Fig. 4). Thus, qualitatively, the latent heat of phase transition is consistent with the model according to which the properties of nanocapillary water in the collagen structure are close to the properties of free (or bulk) water. The increased melting temperature of bound-water ice in collagen and the increased difference between heat capacities Δc_p suggest a correlation between the structures of water and functional groups, probably of the clathrate type.

In conclusion, note that, according to ^{2}H NMR data, the degree of disorder and the diffusion mobility of water molecules in dense regions of the collagen structure also decreased with temperature. However, the observed smooth changes in the doublet splitting over a wide temperature range from –20 to –30°C are more typical of nanopore systems like zeolites and clay minerals. As a rule, phase transitions in systems of this kind are order–disorder transitions (close to second-order phase transitions). According to the experimental data obtained by differential scanning calorimetry, no heat effects related to ordering in the subsystem of dense regions occurred in rat-tail tendon collagen. It is believed that the ordering of water molecules in dense regions was accompanied by a second-order phase transition.

This work was supported by the Russian Foundation for Basic Research (project no. 05-03-32263) and, in part, by the US Civilian Research and Development Foundation (grant no. O-008-XI).

REFERENCES

1. *Collagen*, Ed. by M. E. Nimni (CRC Press, Boca Raton, FL, 1988), Vols. 1–4.
2. J. P. Orgel, A. Miller, T. C. Irving, *et al.*, Structure **9**, 1061 (2001).
3. J. P. Orgel, A. Miller, T. C. Irving, and T. J. Wess, Fibre Diffr. Rev. **10**, 40 (2002).
4. T. J. Wess, A. P. Hammersley, L. Wess, and A. Miller, J. Mol. Biol. **248**, 485 (1995).
5. D. J. S. Holmes, T. J. Wess, D. J. Prockop, and P. Fratzl, Biophys. J. **68**, 1661 (1995).
6. R. B. D. Frazer and B. L. Trus, Biosci. Rep. **6**, 221 (1986).
7. D. Freude, *Encyclopedia of Analytical Chemistry*, Ed. by R. A. Meiers (Wiley, Chichester, 2000), p. 12 188.
8. S. P. Gabuda, A. A. Gaĭdash, and E. A. Vyazovaya, Biofizika **50** (2), 231 (2005).
9. *Thermodynamic Properties of Individual Substances*, Ed. by V. P. Glushko *et al.* (Nauka, Moscow, 1978), Vol. 1, Book 2 [in Russian].

Translated by V. Makhlyarchuk